

UNIVERSITY OF CALIFORNIA, SAN DIEGO

**Design of a Low-cost Underwater Acoustic Modem for Short-Range
Sensor Networks**

A thesis submitted in partial satisfaction of the
requirements for the degree
Doctor of Philosophy

in

Computer Science and Engineering

by

Bridget Benson

Committee in charge:

Professor Ryan Kastner, Chair
Professor Rajesh Gupta
Professor John Hildebrand
Professor Tajana Rosing
Professor Curt Schurgers

2010

Copyright
Bridget Benson, 2010
All rights reserved.

The thesis of Bridget Benson is approved, and it is acceptable in quality and form for publication on microfilm and electronically:

Chair

University of California, San Diego

2010

DEDICATION

To everyone who told me not to give up.

EPIGRAPH

Enjoy the Process

—Dr. Dan Clark

TABLE OF CONTENTS

Signature Page		iii
Dedication		iv
Epigraph		v
Table of Contents		vi
List of Figures		ix
List of Tables		xii
Acknowledgements		xiii
Vita and Publications		xv
Abstract of the Dissertation		xvii
Chapter 1	Introduction	1
Chapter 2	Motivating Applications	4
	2.1 Coral Reefs	4
	2.2 Autonomous Drifter Swarms	7
	2.3 Shallow Water Moorings	8
	2.4 Power Utilities	10
	2.5 Summary	11
Chapter 3	Comparison of RF, Optical and Acoustic Communication Un- derwater	12
	3.1 Radio Frequency Waves	12
	3.1.1 Conductivity	13
	3.1.2 Wavelength	14
	3.1.3 Air/Water Interface	15
	3.1.4 Existing RF Systems	16
	3.2 Optical Waves	18
	3.2.1 Physics of Optical Waves Underwater	18
	3.2.2 Existing Optical Systems	21
	3.3 Acoustic Waves	22
	3.3.1 Absorption Loss	22
	3.3.2 Spreading Loss	24
	3.3.3 Noise	24
	3.3.4 Passive Sonar Equation	27

	3.3.5	Multipath	29
	3.4	Summary	30
Chapter 4		Existing Underwater Acoustic Modems	32
	4.1	Commercial Modems	32
	4.2	Research Modems	37
	4.3	Summary	39
Chapter 5		Transducer Design	42
	5.1	Piezo Ceramics	42
	5.1.1	Type	43
	5.1.2	Geometry	44
	5.2	Transducer Construction	46
	5.2.1	Wiring	47
	5.2.2	Potting	47
	5.2.3	Reducing Unwanted Acoustic Radiation	49
	5.2.4	Material Costs	50
	5.3	Calibration Procedures	50
	5.3.1	Comparison Method	50
	5.3.2	Reciprocity Method	51
	5.4	Experimental Measurements	53
	5.5	Summary	57
Chapter 6		Analog Transceiver Design	58
	6.1	Power Amplifier Design	58
	6.2	Power Management Circuit	67
	6.3	Impedance Matching Circuit	68
	6.4	Pre-Amplifier Design	77
	6.5	Summary	80
Chapter 7		Digital Design	81
	7.1	Modulation Schemes	81
	7.2	Hardware Platforms	85
	7.3	Digital Transceiver	87
	7.3.1	Modulator	89
	7.3.2	Digital Down Converter	90
	7.3.3	Symbol Synchronizer	91
	7.3.4	Demodulator	104
	7.3.5	Clock Generation	105
	7.3.6	HW/SW Co-Design Controller	106
	7.4	Resource Requirements	108
	7.5	Summary	110

Chapter 8	System Tests	111
	8.1 Analog Testing	111
	8.2 Digital Testing	114
	8.2.1 Hard Wired Tests	114
	8.2.2 Bucket Tests	118
	8.3 Integrated Tests	120
	8.3.1 Multipath Measurements	120
	8.3.2 Tank Tests	121
	8.3.3 Canyon View Pool Tests	123
	8.3.4 Westlake Tests	124
	8.3.5 Integrated System Test Summary	128
	8.4 Summary	128
Chapter 9	Deployment Considerations	130
	9.1 Linear Programming Model	130
	9.2 Battery Considerations	136
	9.3 Housing Considerations	137
	9.4 Marine Life Considerations	138
	9.4.1 Physical Effects	138
	9.4.2 Acoustic Effects	139
	9.5 Summary	140
Chapter 10	Future Improvements	141
Appendix A	Bill Of Materials	143
Bibliography	145

LIST OF FIGURES

Figure 2.1: 2009 Sensor Deployment around Moorea	6
Figure 2.2: Proposed Autonomous Drifter Swarm	7
Figure 2.3: Southern California Coastal Ocean Observing System	10
Figure 3.1: Electromagnetic Spectrum	13
Figure 3.2: RF Attenuation vs. Frequency in Fresh and Sea Water	14
Figure 3.3: RF Wavelength vs. Frequency in Sea Water, Fresh Water, and Air	15
Figure 3.4: Air to Water Refraction Loss as a Function of Frequency	16
Figure 3.5: Wireless Fibre Systems SeaText Modem	17
Figure 3.6: Absorption Coefficient of Pure Seawater	19
Figure 3.7: The Spectral Transmittance over the upper 10m of water for Jerlov water types	20
Figure 3.8: Acoustic Absorption as a function of temperature, pressure, and pH	23
Figure 3.9: Acoustic Spherical and Cylindrical Spreading Loss	25
Figure 3.10: Sound Levels of Ocean Background Noises	26
Figure 3.11: Source Level vs. Transmission Distance for a 40 kHz carrier an ambient noise of 50 dB re 1 uPa at various levels of SNR	28
Figure 3.12: Ray Trace for a 40kHz source with a 15 degree beam angle placed at 10 meters depth in a body of water 11 meters deep with a constant sound speed of 1500 m/s	29
Figure 5.1: (a) Raw PZT , (b) Prepotted Transducer , (c) and Potted Trans- ducer	47
Figure 5.2: Transducer Transmitter Voltage Response	54
Figure 5.3: Transducer Receiver Voltage Response	55
Figure 5.4: Transducer Figure of Merit	56
Figure 6.1: Analog Transceiver	59
Figure 6.2: Class A Amplifier Input/Output Characteristic	60
Figure 6.3: Class B Amplifier Input/Output Characteristic for one transistor	61
Figure 6.4: Class AB Amplifier Input/Output Characteristic for one tran- sistor	61
Figure 6.5: Block diagram of a basic switching or PWM (Class-D) amplifier	63
Figure 6.6: Block diagram of the power amplifier design making use of a class AB and class D amplifier to achieve linearity and efficiency	63
Figure 6.7: Class AB Power Amplifier Linearity	64
Figure 6.8: Complete Power Amplifier Linearity	65
Figure 6.9: Power Amplifier Power Efficiency	66
Figure 6.10: Power Management Circuit	67

Figure 6.11: Maximum Power Transfer is achieved when Z_S matches Z_L . . .	68
Figure 6.12: Electrical Equivalent Circuit Model for a Transducer	69
Figure 6.13: Measured and Simulated Current of the Transducer	70
Figure 6.14: Measured and Simulated Impedance Magnitude of the Transducer	71
Figure 6.15: Measured and Simulated Impedance Phase of the Transducer .	72
Figure 6.16: Transducer Impedance Matching Circuit	73
Figure 6.17: Impedance Matched Measured and Simulated Current of the Transducer	74
Figure 6.18: Impedance Matched Measured and Simulated Impedance Mag- nitude of the Transducer	75
Figure 6.19: Impedance Matched Measured and Simulated Impedance Phase of the Transducer	76
Figure 6.20: Estimated Power Coupled into the Transducer	77
Figure 6.21: Receiver Block Diagram	78
Figure 6.22: Overall Receiver Gain	79
Figure 7.1: Block diagram of classic matched filter FSK demodulator . . .	82
Figure 7.2: Bit Error Rate of MFSK and MPSK for a given probability of error	83
Figure 7.3: Block diagram of a coherent PSK receiver	84
Figure 7.4: Block Diagram of Complete Digital Receiver	88
Figure 7.5: Block Diagram of FSK Modulator	90
Figure 7.6: Block Diagram of Digital Down Converter	91
Figure 7.7: Process of Symbol Synchronization	92
Figure 7.8: Auto Correlation (blue) and Cross Correlation (black) of Or- thogonal Gold (a), Walsh (b) and PN (c) Reference Codes . . .	95
Figure 7.9: MATLAB simulation of symbol synchronization for underwater FSK	97
Figure 7.10: Block Diagram of Symbol Synchronization for Underwater FSK	98
Figure 7.11: Hardware Units of Correlation Implementation for Underwater FSK	100
Figure 7.12: Control Structure of Symbol Synchronization for Underwater FSK	102
Figure 7.13: Block Diagram of Matched Filter FSK Demodulator	104
Figure 7.14: (a) Clock Division, (b) Added Flip Flop between clock domain to avoid metastability	105
Figure 7.15: HW/SW Co-Design for the digital transceiver	106
Figure 7.16: Digital Transceiver Control Flow. Interrupts are shown in red .	107
Figure 8.1: Mission Bay Test Set Up. (a) Transmitter on dock, (b) Receiver on boat	112
Figure 8.2: Mission Bay Receive Distances	113
Figure 8.3: DINI DMEG-AD/DA Test Platform	114

Figure 8.4:	HyperTerminal Output Window showing correct transmission of two hard wired packets	115
Figure 8.5:	ChipScope Internal Waveforms and signals from a 100-bit data length test	117
Figure 8.6:	12" Bucket Test	118
Figure 8.7:	Snapshot of hardware simulation result for 12" bucket test . . .	119
Figure 8.8:	Multipath Amplitude Delay Profile at 0.5 m in the tank	122
Figure 8.9:	Multipath Amplitude Delay Profile at 50m in the Canyon View Pool	123
Figure 8.10:	Test Locations in Westlake	125
Figure 8.11:	Multipath Amplitude Delay Profile at 5m in Westlake	126
Figure 8.12:	Multipath Amplitude Delay Profile at 50m in Westlake	126
Figure 8.13:	Multipath Amplitude Delay Profile at 95m in Westlake	127
Figure 8.14:	System Test Results	129
Figure 9.1:	Santa Barbara RelocaTable Mooring (CHARM)	133
Figure 9.2:	Routing schemes for optimal cost and energy (for 6 month deployment) or lifetime (for 140kJ of energy) on the CHARM . .	135

LIST OF TABLES

Table 2.1: 2009 Sensor Deployment around Moorea	5
Table 3.1: Rates, Ranges, and Uses of Wireless Fibre Systems RF Modems	18
Table 3.2: Comparison of RF, optical and acoustic communication under- water	31
Table 4.1: Commercial Underwater Acoustic Modem Comparison	36
Table 4.2: Research Underwater Acoustic Modem Comparison	41
Table 6.1: Power Management Characteristics	68
Table 7.1: Digital Transceiver Parameters	89
Table 7.2: Digital Design Resource Usage	108
Table 7.3: FPGA Power Consumption	109
Table 7.4: Digital Transceiver Design Comparison	109
Table 9.1: Data amounts for major sensors and sensor packages on the CHARM	134
Table 9.2: UCSDModem Power Characteristics	134
Table 9.3: Minimum Energy and Cost Requirements for a 6 month deploy- ment of the CHARM mooring	136
Table A.1: Underwater Modem Bill of Materials	144

ACKNOWLEDGEMENTS

I would first and foremost like to thank my research team, Kenneth Domond, Brian Faunce, and Ying Li, whose hard work on the modem transducer, analog transceiver, and digital transceiver respectively is incorporated in this text. I would also like to thank all those who have provided advice and support to our modem project including Don Kimball, Professor Curt Shurgers, Professor Feng Tong, Doug Palmer, Cuong Vu, Diba Mirza, Feng Lu, Paul Roberts, Fernando Simonet, Dr. Andrew Brooks, Professor Jules Jaffe, Professor Bill Hodgkiss, Jen Trezzo, S.N. Hemanth Meenakshisundaram, Digvijay Dalapathi, Brent Hurley, Ethan Roth, Daniel Johnson, and Barbara Lloyd.

I thank my advisor, Professor Ryan Kastner, for understanding my character and allowing me to explore many different exciting research areas before focusing on a dissertation topic. I thank him for pushing me to become a teaching assistant, apply for fellowships, and write research papers starting in my first year of graduate school to force me to hit the ground running and keep the momentum going throughout my graduate career. I also thank my committee members, Professor Curt Schurgers, Professor Rajesh Gupta, Professor Tajana Rosing, and Professor John Hildebrand, for guiding me through the writing of this thesis. I would also like to thank Professor Sally MacIntyre, Professor Diana Franklin, Dr. Grace Chang Spada, Professor Ron Iltis, and Professor Hua Lee for providing me with assistance and direction throughout graduate school.

I am indebted to my many student colleagues for providing a positive and fun environment in Santa Barbara and San Diego. I am especially grateful to Chris Utley, Tricia Fu, Daniel Doonan, Arron Layns, Ali Irturk, Arash Arfaee, Shahnam Mirzaei, Junguk Cho, Deborah Goshorn, Jason Oberg, Wei Hu, and Janarbek Matay.

I would like to thank all my family and friends who have supported me on my journey through graduate school and have made this dissertation possible. I would especially like to thank my parents, Joann and Stan Benson, my sisters, Gianna and Linda Fé Benson, and my significant other, Adam Volk, for always believing in me and providing me with unconditional love and support.

Finally, I thank the National Science Foundation for providing me with a Graduate Research Fellowship and my advisor with Grant #0816419 to support the work described in this dissertation.

The text of Chapter 5, is currently being prepared for submission for publication of the material. The dissertation author was a co-primary researcher and author (with Kenneth Domond). Ryan Kastner and Don Kimball directed and supervised the research which forms the basis for Chapter 5.

The text of Chapter 7.3.3 is in part a reprint of the material as it appears in the proceedings of the IEEE International Conference on Sensor Networks, Ubiquitous, and Trustworthy Computing. The dissertation author was a co-primary researcher and author (with Ying Li). The other co-authors listed on this publication [3] directed and supervised the research which forms the basis for Chapter 7.3.3.

The text of Chapter 7.3.1, 7.3.2, 7.3.4, and 7.3.6 is currently being prepared for submission for publication of the material. The dissertation author is a co-primary researcher and author (with Ying Li). Ryan Kastner and Xing Zhang directed and supervised the research which forms the basis for Chapter 7.3.1, 7.3.2, 7.3.4, and 7.3.6.

Selections of Chapter 8 are in part a reprint of the material as it appears in the proceedings of the IEEE Oceans Conference. The dissertation author was a co-primary researcher and author along with Ying Li, Brian Faunce, and Kenneth Domond. The other co-authors listed on this publication [1] directed and supervised the research which forms the basis for Chapter 8.

The ideas conveyed in the thesis are shared with the material in the proceedings of the IEEE Oceans Conference and the Embedded Systems Letters. The dissertation author was a co-primary researcher and author along with Ying Li, Brian Faunce, and Kenneth Domond. The other co-authors listed on these publications [1, 2] directed and supervised the research which forms the basis for the dissertation.

VITA

- 2005 B. S. in Computer Engineering *summa cum laude*, California Polytechnic State University, San Luis Obispo
- 2007 M. S. in Electrical and Computer Engineering, University of California, Santa Barbara
- 2010 Ph. D. in Computer Science and Engineering, University of California, San Diego

PUBLICATIONS

Bridget Benson, Ying Li, Brian Faunce, Kenneth Domond, Don Kimball, Curt Schurgers, and Ryan Kastner, “Design of a Low-Cost Underwater Acoustic Modem”, *Embedded Systems Letters*, accepted.

Bridget Benson, Ying Li, Brian Faunce, Kenneth Domond, Don Kimball, Curt Schurgers, and Ryan Kastner, “Design of a Low-Cost, Underwater Acoustic Modem for Short-Range Sensor Networks”, *IEEE Oceans Conference*, May 2010.

Ying Li, Bridget Benson, Ryan Kastner, and Xing Zhang, “Hardware Implementation of Symbol Synchronization for Underwater FSK”, *IEEE International Conference on Sensor Networks, Ubiquitous, and Trustworthy Computing*, June 2010.

Ying Li, Bridget Benson, Ryan Kastner, and Xing Zhang, “Bit Error Rate, Power, and Area Analysis of Multiple Implementations of Underwater FSK”, *Engineering of Reconfigurable Systems and Algorithms*, July 2009.

Bridget Benson, Ali Irturk, Junguk Cho and Ryan Kastner, “Energy Benefits of Reconfigurable Hardware for Use in Underwater Sensor Nets”, *IEEE Reconfigurable Architectures Workshop*, May 2009.

Bridget Benson, Ali Irturk, Junguk Cho, and Ryan Kastner, “Survey of Hardware Platforms for an Energy Efficient Implementation of Matching Pursuits Algorithm for Shallow Water Networks”, *International Workshop on UnderWater Networks*, September 2008.

Feng Tong, Bridget Benson, Ying Li, and Ryan Kastner, “Channel Equalization Based on Data Reuse LMS Algorithm for Shallow Water Acoustic Communication”, *IEEE International Conference on Sensor Networks, Ubiquitous, and Trustworthy Computing*, June 2010.

Bridget Benson, Frank Spada, Derek Manov, Grace Chang and Ryan Kastner, “Real Time Telemetry Options for Ocean Observing Systems”, *European Telemetry Conference*, April 2008.

Bridget Benson, Grace Chang, Derek Manov, Brian Graham and Ryan Kastner, “Design of a Low-cost Acoustic Modem for Moored Oceanographic Applications”, *International Workshop on Underwater Networks*, September 2006.

Bridget Benson, Junguk Cho, Deborah Goshorn, and Ryan Kastner, “Field Programmable Gate Array Based Fish Detection Using Haar Classifiers”, *American Academy of Underwater Sciences*, March 2009.

Bridget Benson, Arash Arfaee, Choon Kim, Ryan Kastner, and Rajesh Gupta, “Integrating Embedded Computing Systems into High School and Early Undergraduate Education”, *International Conference on Microelectronic Systems Education*, July 2009.

Junguk Cho, Bridget Benson, Sunsern Cheamanukul, and Ryan Kastner, “Increased Performance of an FPGA-Based Color Classification System”, *IEEE Symposium on Field-Programmable Custom Computing Machines*, May 2010.

Junguk Cho, Bridget Benson, and Ryan Kastner, “Hardware Acceleration of Multi-view Face Detection”, *IEEE Symposium on Application Specific Processors*, July 2009.

Junguk Cho, Bridget Benson, Shahnam Mirzaei, and Ryan Kastner. “Parallelized Architecture of Multiple Classifiers for Face Detection”, *IEEE International Conference on Application-specific Systems, Architectures, and Processors*, July 2009.

Ali Irturk, Bridget Benson, Shahnam Mirzaei and Ryan Kastner, “GUSTO: An Automatic Generation and Optimization Tool for Matrix Inversion Architectures”, *ACM Transactions on Embedded Computing Systems*.

Ali Irturk, Bridget Benson, Nikolay Laptev and Ryan Kastner, “Architectural Optimization of Decomposition Algorithms for Wireless Communication Systems”, *IEEE Wireless Communications and Networking Conference (WCNC 2009)*, April 2009.

Ali Irturk, Bridget Benson and Ryan Kastner, “Automatic Generation of Decomposition based Matrix Inversion Architectures”, *IEEE International Conference on Field-Programmable Technology (ICFPT)*, December 2008.

Ali Irturk, Bridget Benson, Nikolay Laptev and Ryan Kastner, “FPGA Acceleration of Mean Variance Framework for Optimum Asset Allocation”, *Workshop on High Performance Computational Finance at SC08 International Conference for High Performance Computing, Networking, Storage and Analysis*, November 2008.

Ali Irturk, Bridget Benson, Shahnam Mirzaei and Ryan Kastner, “An FPGA Design Space Exploration Tool for Matrix Inversion Architectures”, *IEEE Symposium on Application Specific Processors (SASP)*, June 2008.

ABSTRACT OF THE DISSERTATION

**Design of a Low-cost Underwater Acoustic Modem for Short-Range
Sensor Networks**

by

Bridget Benson

Doctor of Philosophy in Computer Science and Engineering

University of California, San Diego, 2010

Professor Ryan Kastner, Chair

Small, dense, wireless sensor networks are beginning to revolutionize our understanding of the physical world by providing fine resolution sampling of the surrounding environment. The ability to have many small devices streaming real-time data physically distributed near the objects being sensed brings new opportunities to observe and act on the world which could provide significant benefits to mankind.

While wireless sensor-net systems are beginning to be fielded in applications today on the ground, underwater sensor nets remain quite limited by comparison. Still, a large portion of ocean research is conducted by placing sensors (that measure current speeds, temperature, salinity, pressure, bioluminescence, chemicals, etc.) into the ocean and later physically retrieving them to download and analyze their collected data. Real-time underwater wireless sensor networks that do exist are often sparsely deployed over wide areas.

The existence of small, dense wireless sensor networks on land was made possible by the advent of low-cost radio platforms. These radio platforms cost a

few hundred U.S. dollars enabling researchers to purchase many nodes with a fixed budget allowing for dense, short-range deployment. The aquatic counterpart to the terrestrial radio is the underwater acoustic modem. Existing underwater acoustic modems' power consumption, ranges, and price points are all designed for sparse, long-range, expensive systems rather than for small, dense, and inexpensive sensor-nets. It is widely recognized that an aquatic counterpart to inexpensive terrestrial radio would be required to enable deployment of small dense underwater wireless sensor networks for advanced underwater ecological analyses.

This thesis describes the full design of an underwater acoustic modem for small, dense wireless sensor networks starting with the most critical component from a cost perspective - the transducer. The design replaces a commercial underwater transducer with a homemade underwater transducer using inexpensive piezoceramic material and builds the rest of the modem's components around the properties of the homemade transducer to extract as much performance as possible. By building the modem from inexpensive components, the design provides a low-cost, low-power alternative to existing commercial modems for use in short-range networks.

Chapter 1

Introduction

Small, dense, wireless sensor networks are beginning to revolutionize our understanding of the physical world by providing fine resolution sampling of the surrounding environment. The ability to have many small devices streaming real-time data physically distributed near the objects being sensed brings new opportunities to observe and act on the world which could provide significant benefits to mankind. For example, dense wireless sensor networks have been used in agriculture to improve the quality, yield and value of crops, by tracking soil temperatures and informing farmers of fruit maturity and potential damages from freezing temperatures [4]. They have been deployed in sensitive habitats to monitor the causes for mortality in endangered species [5]. Dense wireless sensor networks have also been used to detect structural damages on bridges and other civil structures to inform authorities of needed repair [6] and have been used to monitor the vibration signatures of industrial equipment in fabrication plants to predict mechanical failures [7].

While wireless sensor-net systems are beginning to be fielded in applications on the ground, underwater sensor nets remain quite limited by comparison [8]. Still, a large portion of ocean research is conducted by placing sensors (that measure current speeds, temperature, salinity, pressure, bioluminescence, chemicals, etc.) into the ocean and later physically retrieving them to download and analyze their collected data. This method does not provide for real-time analysis of data which is critical for event prediction. Real-time underwater wireless sensor networks that

do exist are often sparsely deployed over wide areas. For example, the Deep-ocean Assessment and Reporting of Tsunami (DART) project consists of 39 stations worldwide acquiring critical data for early detection of tsunamis [12]. The FRONT network consists of about 10 subsurface wirelessly networked sensors spaced about 9km apart in the inner continental shelf outside Block Island Sound to increase scientific understanding of the coastal ocean [9]. The SeaWeb network consists of tens of nodes spaced 2-5km apart for oceanographic telemetry, underwater vehicle control, and other uses of underwater wireless digital communications [10, 11]. Other real-time networks that exist are wired and extremely expensive [13, 14, 15, 16].

The existence of small, dense wireless sensor networks on land was made possible by the advent of low-cost radio platforms such as PicoRadio and Mica2 [17, 18]. These radio platforms cost a few hundred U.S. dollars enabling researchers to purchase many nodes with a fixed budget allowing for dense, short-range deployment. The aquatic counterpart to the terrestrial radio is the underwater acoustic modem. There are a number of acoustic modems currently available including commercial offerings from companies like Teledyne Benthos, DSPComm, LinkQuest and Tritech and academic projects, most notably the WHOI MicroModem. Unfortunately, these existing modems' power consumption, ranges, and price points are all designed for sparse, long-range, expensive systems rather than small, dense, and inexpensive sensor-nets [8, 19, 20]. It is widely recognized that an aquatic counterpart to inexpensive terrestrial radio is required to enable deployment of small dense underwater wireless sensor networks for advanced underwater ecological analyses.

Thesis Statement: This thesis describes the design of a short-range underwater acoustic modem starting with the most critical component from a cost perspective - the transducer. The transducer is the device that converts electrical energy to/from acoustic energy, which is equivalent to the antenna in radios. The design substitutes a commercial underwater transducer with a home-made underwater transducer using cheap piezoceramic material and builds the rest of the modem's components around the properties of the transducer to extract as much performance as possible. The modem provides bit rates of up to 200 bps for

ranges up to 400 m at a components cost of \sim \$350 U.S. The major contributions of this thesis are:

- The design and analysis of a low-cost omni-directional transducer
- The design of a novel acoustic analog transceiver
- The design of a field programmable gate array (FPGA) implementation of a frequency shift keying (FSK) based digital transceiver that provides comparable power consumption to other underwater digital transceiver designs
- A field-tested, proof-of-concept system prototype of a low-cost underwater acoustic modem that consists of the low-cost omni-directional transducer, the novel analog transceiver, and FPGA FSK based digital transceiver
- A linear programming model that optimizes for cost, energy consumption or deployment time for underwater modems deployed on a linear underwater network

This thesis is organized as follows: Chapter 2 describes a few applications of small, dense networks, that would be enabled if a low-cost underwater acoustic modem were available. Chapter 3 describes the selection of using acoustic modems (instead of RF or optical modems) for underwater communication based on the physics of the underwater environment. Chapter 4 describes existing commercial and research underwater acoustic modems to illustrate the novelty and applicability of our design. Chapters 5, 6, and 7 describe the transducer, analog transceiver, and digital transceiver design of the modem (hereinafter referred to as the UCSD-Modem) respectively. Chapter 8 reports analog, digital, and system test results of the UCSDModem from simulations, a test tank, and the field. Chapter 9 describes deployment considerations for the UCSDModem including a linear programming model to determine cost, energy, and lifetime of a deployment, as well as battery, housing, and marine life considerations. We conclude the thesis in Chapter 10 with a discussion on possible future improvements to the modem design. The complete bill of materials (BOM) is included in the Appendix.

Chapter 2

Motivating Applications

This chapter describes a few dense underwater sensor network applications that motivate the need for a low-cost underwater acoustic modem, including applications involving coral reefs, autonomous drifter swarms, shallow-water moorings, and power plants. We describe the application and its socio-scientific impact and describe how a low-cost underwater acoustic modem can enable or improve the application for further scientific advancement. We conclude by summarizing the common requirements of these applications.

2.1 Coral Reefs

Coral reefs are of prime ecological and economic importance, having the highest species diversity of any marine habitat. Unfortunately, they are under stress due to increasing temperature and acidity of the oceans, episodic pulses from major storms, and heightened incidence of disease.

Because of the complexity of coral reef ecosystems, there is an incomplete understanding of the processes that collectively determine their structure, function and dynamics. Fundamental to efforts to understand coral reef ecosystems is a broad suite of environmental observations ranging from basic environmental factors such as water temperature, salinity and bio-optical variables, to more complex measurements such as nutrient concentration, the presence/absence of environmental estrogens, volatile hydrocarbons, and pathogenic bacteria. More

complex observations include tracking fishes and monitoring currents including flows of nutrients in the reef. The opportunities for enhancing marine science through the development of advanced sensing systems are seemingly endless.

The University of California’s Gump Research Station on the island of Moorea, French Polynesia, is the National Science Foundation’s coral reef long term ecological research (LTER) site. Moorea is a high, 1.2 million year old volcanic island surrounded by a well-developed coral reef and lagoon system. The coastal environments of Moorea offer an excellent opportunity for studies of coral reef ecosystems. An offshore barrier reef forms a system of shallow, narrow lagoons around the 60 km perimeter of Moorea [21]. All major coral reef types are present and accessible by small boat. The reefs are in excellent condition and have been subject to relatively few natural disturbances in the last several decades. The cover of coral and abundance of reef fishes are high, and the Territorial Government recently set aside large tracts of reefs around Moorea as protected areas.

Table 2.1: 2009 Sensor Deployment around Moorea

Instrument	Quantity	Unit Cost	Sampling Regime
RDI Workhorse Sentinel Acoustic Doppler Current Profiler	3	\$35000	15 pings every minute at 120 Hz for currents 20 pings every 3 hours at 120KHz for waves
Seabird SBE26+ Wave/Tide Recorders	3	\$19000	Every 20 minutes for 60 seconds for tides and 4096 samples at 240Hz for waves
Seabird SBE39 Thermistor and Pressure sensor	8	\$1500	Every 2 minutes
Seabird SBE37 CTD recorder	8	\$6000	Every 2 minutes
Onset temperature loggers	12	\$110	Every 2 minutes
Seabird SBE39 thermistors	35	\$1000	Every 2 minutes

The present state of sensing systems in Moorea is primitive; ecological research could be significantly enhanced with appropriate technology. Currently,

scuba divers deploy sensors with data loggers. The sensors are typically deployed for months at a time, then recovered for cleaning, battery replacement, and data offload. Figure 2.1 shows the 2009 sensor deployment around the island and Table 2.1 describes the types, quantity, cost, and sampling regimes of these sensors.

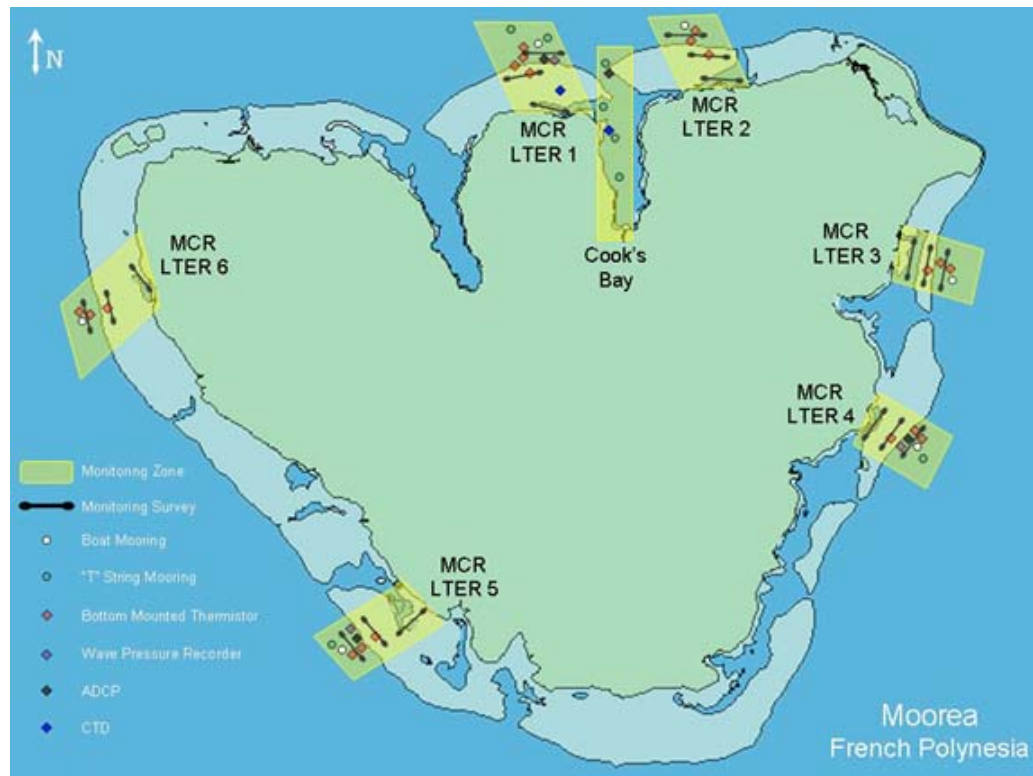


Figure 2.1: **2009 Sensor Deployment around Moorea**

The ability to perform real-time, adaptive ecological experiments would represent a significant advance in ecological sensing. The grand vision is a ‘Digital Moorea’: a prototype observation system which produces an accurate, virtual digital representation of Moorea’s coral reefs updated by real-time adaptive sampling. As underwater cabling requires extensive environmental permitting and can be damaging to the reefs, a wireless networking option is necessary to make Digital Moorea a reality. As sensors in a monitoring area are currently less than 500m apart (Figure 2.1), and the majority of the sensors deployed (i.e. thermistors) have low data rates (Table 2.1), expensive, long-range, high data rate commercial underwater modems are excessive and cost-prohibitive for this application. Thus a

low-cost underwater acoustic modem intended for dense, short-range, low data-rate applications would be well suited to enable advanced monitoring in coral reefs.

2.2 Autonomous Drifter Swarms

Another application that has potentially large scientific and socio-economic impact is the development of an autonomous drifter swarm [22, 23]. A drifter or subsurface float is an underwater vehicle that only possesses buoyancy control, allowing it to change its depth. It is not actively propelled in the x-y-direction; instead, it is carried directly by the currents and tides. When equipped with sensors, such a drifter enables scientists to observe subsurface phenomena as they move along with the current. This Lagrangian sampling regime is very different from that provided by actively propelled vehicles or stationary sensors. Furthermore, instead of considering only a single drifter, a swarm consisting of tens to hundreds of these devices can provide true 4-dimensional sampling in a Lagrangian framework. Figure 2.2 depicts an autonomous drifter swarm.



Figure 2.2: **Proposed Autonomous Drifter Swarm**

The potential applications of this new technology are far-reaching and promise to provide a wealth of new data. For example, the creation and movement of harmful toxic algal blooms (red tides) is poorly understood and requires correlating the related biological processes with currents and tides. Other important applications include the tracking of pollution or patches such as oil spills. Also, the ability to track the migration of larvae, which for many species rely on passive

oceanic transport, is instrumental in evaluating the efficacy of marine protected areas.

To operate as a 4-dimensional sampling system, the drifter swarm has to be able to track the positions of each drifter, as this is crucial to deduce correlations between sampling points. Efficient and scalable position tracking hinges on the ability of the drifters to communicate with each other while submerged, as it enables them to estimate inter-device distances and exchange information [24]. Acoustic communications is thus a crucial component of this overall system. Furthermore, the power of the drifter swarm also lies in the fact that this system can provide sampling at heretofore unattainable densities, relying on many vehicles. The reason why this is possible is that compared to other vehicle technologies, such as gliders or ROVs, drifters can be fabricated at a fraction of the cost [23]. However, this also means that cost-effectiveness is also crucial for the corresponding acoustic modem technology. Our low-cost underwater acoustic modem design is therefore a key component in realizing practical Lagrangian sampling using drifter swarms.

2.3 Shallow Water Moorings

Moorings provide an effective way to monitor ocean life and processes by providing a platform for sensors to collect data throughout the entire water column over large temporal scales. The high temporal resolution, long-term data collected from moorings capture a broad dynamic range of oceanic variability and provide important information concerning episodic and periodic processes ranging in scale from minutes to years [25, 26]. Such data greatly enhance our understanding of the earth's oceans and contribute to solving world problems such as natural disaster prediction and global warming.

Moorings provide important data sets; however, many moorings do not provide data sets in real-time as existing telemetry options to connect sensors mounted along the mooring line to the surface for data transmission are expensive and limited. Real-time data is crucial for scientists and managers to detect important

events (tsunamis, hurricanes and storms, eddies, harmful algal blooms) in order to respond appropriately, e.g. interrogating the moored instruments to increase their sampling rates.

Existing subsea to surface telemetry options include surface to bottom (hard-wired) cables, acoustic modems, and inductive modems. Surface to bottom cables offer virtually unlimited data rates at low cost, but are prone to mechanical failures. Electro-optical mechanical (EOM) cables are under development for increased resistance to mechanical failure [27], but cost on the order of one thousand to five thousand U.S. dollars for every 100 meters of cable. Inductive modems also make use of a hard-wire along a mooring line [28] and thus are also susceptible to mechanical failure. The cost of a subsurface inductive modem is about \$4000 and the cost of a surface inductive modem is about \$500, thus the total cost of the inductive modem solution depends on the depth of transmission and the number of sensors on the mooring line. Acoustic modems relieve the problems associated with wired transmission as they can transmit data wirelessly up a mooring line. However, existing acoustic modems are costly, making the use of acoustic modems another expensive option. Thus a cheaper acoustic modem could provide a reasonable telemetry option to make real-time data collection on mooring lines a reality.

Consider the Southern California Coastal Ocean Observing System (SCCOOS) mooring as an example of a typical shallow water (less than 300 m) mooring (Figure 2.3). This mooring is located in 80 m water depth, 6 km from shore, and its suite of sensors produce 57000 bytes of data per day. Equipping the mooring with an inexpensive communication cable would cost only \$50 (not including the cost of the underwater connectors), but such a cable would be highly susceptible to mechanical failure. An EOM cable would cost about \$5000. The mooring would require two subsurface modems (inductive or acoustic) and one surface modem. Using the costs noted above, an inductive modem solution would cost around \$8500 and the cost of an acoustic modem solution would be about \$25000 [29]. Thus equipping the mooring with a low cost modem that costs less than \$5000, would provide an inexpensive and reliable option for real-time telemetry.

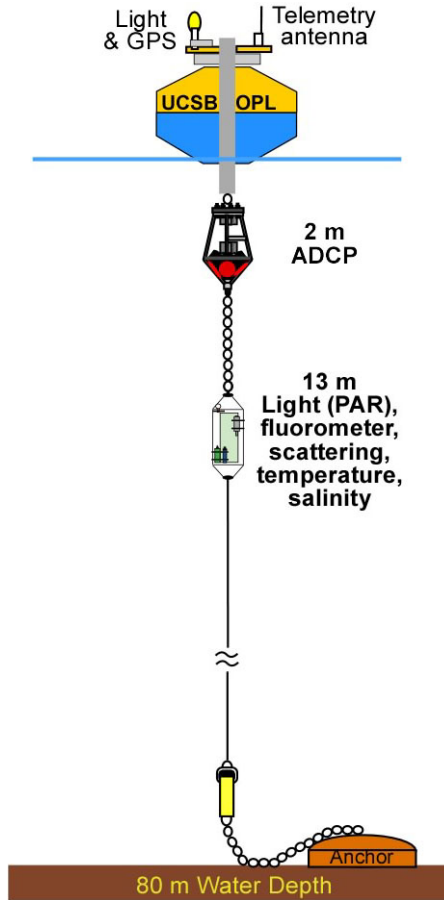


Figure 2.3: Southern California Coastal Ocean Observing System

2.4 Power Utilities

The Tennessee Valley Authority (TVA), located in Norse Tennessee, operates the largest, public owned power utility plant in the country. The TVA performs flood control, power production, and navigation. It operates 3 hydro-nuclear plants, 10 fossil fuel plants, and 20 dams along the Tennessee River. The Tennessee River is around 11ft deep in most areas, and up to 500 ft deep in some tributaries. Typical flow rates are 1-2 ft/sec with maximal flow rates of 6-7 ft/sec during storms.

In order to monitor plant inflow and outflow, the TVA deploys temperature and Dissolved Oxygen (DO) sensors at the intakes and outtakes of each plant. These sensors are deployed on the order of a few hundred meters apart and are

individually attached to surface buoys that telemeter the sub-surface measurement back to shore via radio or cellular modem. The instruments sample data once every 15 minutes and telemeter the four samples back to shore once every hour.

As the buoys and cellular modems or radios, are difficult and expensive to deploy, the TVA is interested in equipping their instruments with underwater acoustic modems to reduce costs and ease the deployment effort. Once again, current commercial modems are excessive and cost-prohibitive for this short-range, low-data rate application, making our low-cost modem an attractive option.

2.5 Summary

This chapter described a few applications that motivate the need for a low-cost underwater modem, including applications involving coral reefs, autonomous drifter swarms, shallow-water moorings, and power plants. These underwater sensor networks are all networks that would greatly benefit from a low-cost underwater modem primarily due to the potentially dense deployment of nodes. In addition, all of the networks require:

- low data rates
- moderate transmission ranges ($< 500\text{m}$)
- shallow deployment depths ($< 100\text{ m}$)
- high energy efficiency for increased deployment time

The next chapter describes the effect of the underwater environment on RF, optical and acoustic waves and describes the selection of using acoustics for our modem design to meet these sensor network requirements.

Chapter 3

Comparison of RF, Optical and Acoustic Communication Underwater

Present underwater communication systems involve the transmission of information in the form of radio frequency (RF) waves, optical waves, or acoustic waves. Each of these techniques has advantages and limitations. This chapter explores the effect of the underwater environment on RF, optical and acoustic waves and describes the rationale for using acoustics for the UCSDModem design to meet the requirements of the target applications described in Chapter 2.

3.1 Radio Frequency Waves

Radio frequency waves are electromagnetic waves in the frequency band below 300GHz. An electromagnetic wave is a wave of energy having a frequency within the electromagnetic spectrum (Figure 3.1) and propagated as a periodic disturbance of the electromagnetic field when an electric charge oscillates or accelerates [30]. Underwater radio frequency communications have been investigated since the very early days of radio [31], and had received considerable attention during the 1970s [32], however few underwater RF systems have been developed due to the highly conducting nature of salt water. This section discusses the effect

of conductivity, wavelength, and air/water interface on RF waves and describes existing underwater systems that make use of RF waves.

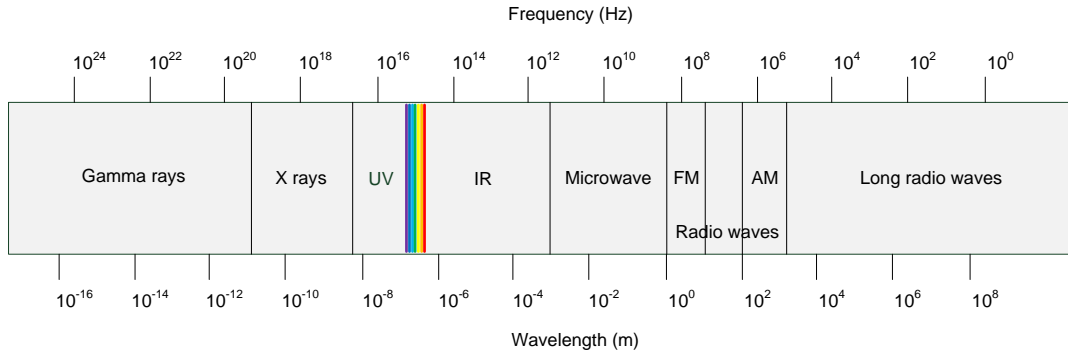


Figure 3.1: **Electromagnetic Spectrum**

3.1.1 Conductivity

Pure water is an insulator, but as found in its natural state, water contains dissolved salts and other matter, which makes it a partial conductor. The higher water's conductivity, the greater the attenuation of radio signals that pass through it. Propagating waves continually cycle energy between the electric and magnetic fields, hence conduction leads to strong attenuation of electromagnetic propagating waves [33]. Sea water has a high salt content and thus high conductivity varying from 2 Siemens/meter (S/m) in the cold arctic region to 8 S/m in the Red Sea [34]. Average conductivity of sea water is considered to be 4 S/m whereas conductivity of fresh water is typically on the order of a few mS/m [35].

Attenuation of radio waves in water increases both with increase in conductivity and increase in frequency. It can be calculated from the following formula [34]:

$$\alpha = 0.0173\sqrt{f\sigma} \quad (3.1)$$

Where α is attenuation in dB/meter, f is the frequency in Hertz, and σ is the conductivity in S/m.

Figure 3.2 shows attenuation as a function of frequency for sea water (4 S/m) and fresh water (0.01 S/m). Attenuation in sea water is very high and to communicate at any reasonable distance, it is necessary to use very low frequencies. However, the consequence of using very low frequencies is the need to use larger antennas to capture the signal of larger wavelength.

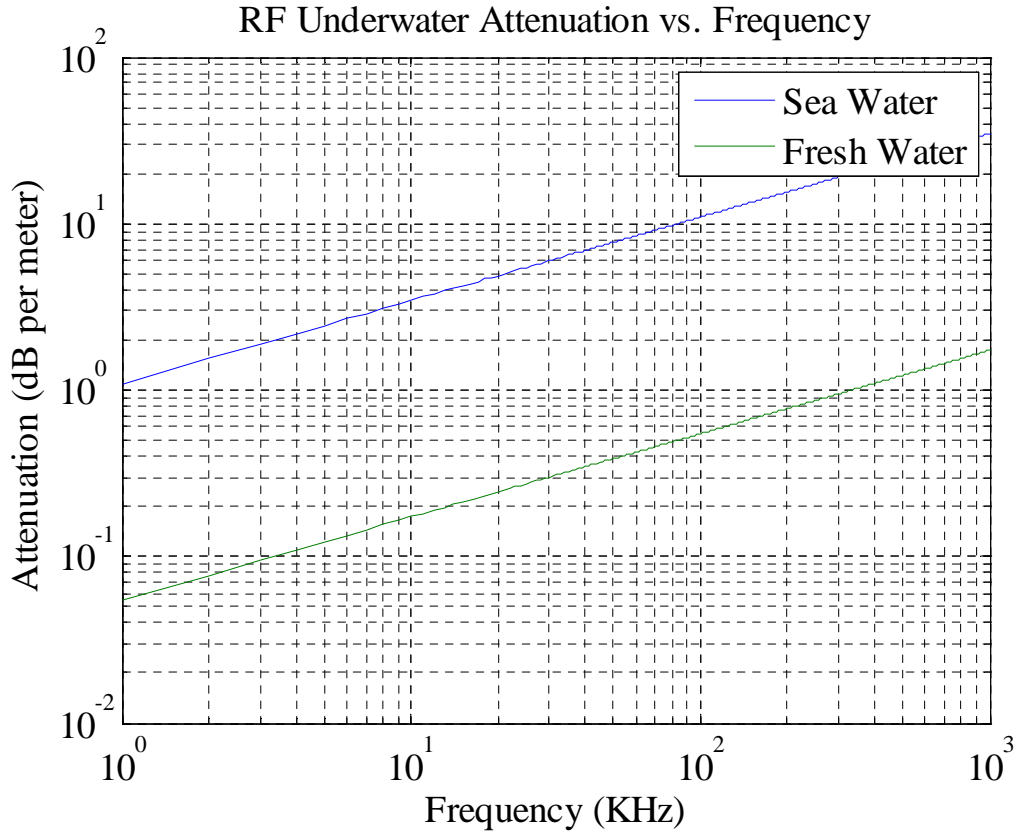


Figure 3.2: **RF Attenuation vs. Frequency in Fresh and Sea Water**

3.1.2 Wavelength

Wavelength in water is calculated from the following formula [34]:

$$\lambda = 1000\sqrt{10/(f\sigma)} \quad (3.2)$$

Where λ is the wavelength in meters, f is the frequency in Hz, and σ is the conductivity in S/m. Figure 3.3 plots wavelength vs frequency in air, sea

water (with conductivity 4 S/m), and fresh water (with conductivity 0.01 S/m). A signal's wavelength in air is considerably reduced underwater (especially in salt water) leading to considerable differences in antenna engineering for terrestrial and underwater communications.

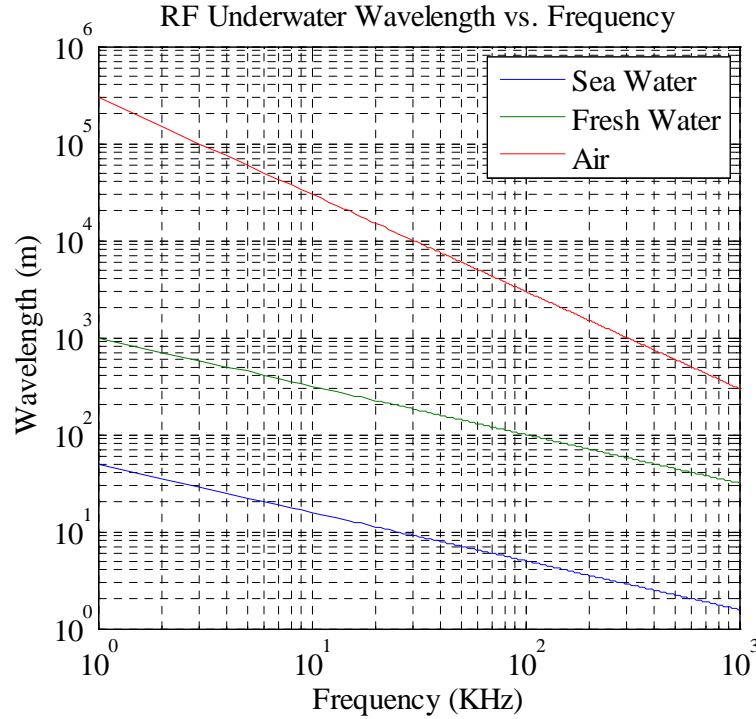


Figure 3.3: RF Wavelength vs. Frequency in Sea Water, Fresh Water, and Air

3.1.3 Air/Water Interface

As the attenuation loss in water is high, higher transmission distances may be achieved by having the signal leave the water near the transmitter, travel via an air-path, (where attenuation loss is low) and re-enter the water near the receiver. However, as RF waves travel from air to water or water to air, there is a refraction loss due to the change in the medium. This loss can be calculated via the following formula [34]:

$$RefractionLoss(dB) = -20\log(7.4586/10^6)\sqrt{10/(f/\sigma)} \quad (3.3)$$

Where f is the frequency in Hz, and σ is the conductivity in S/m.

Figure 3.4 illustrates refraction loss as a function of frequency for sea water and fresh water. As frequency increases refraction loss decreases.

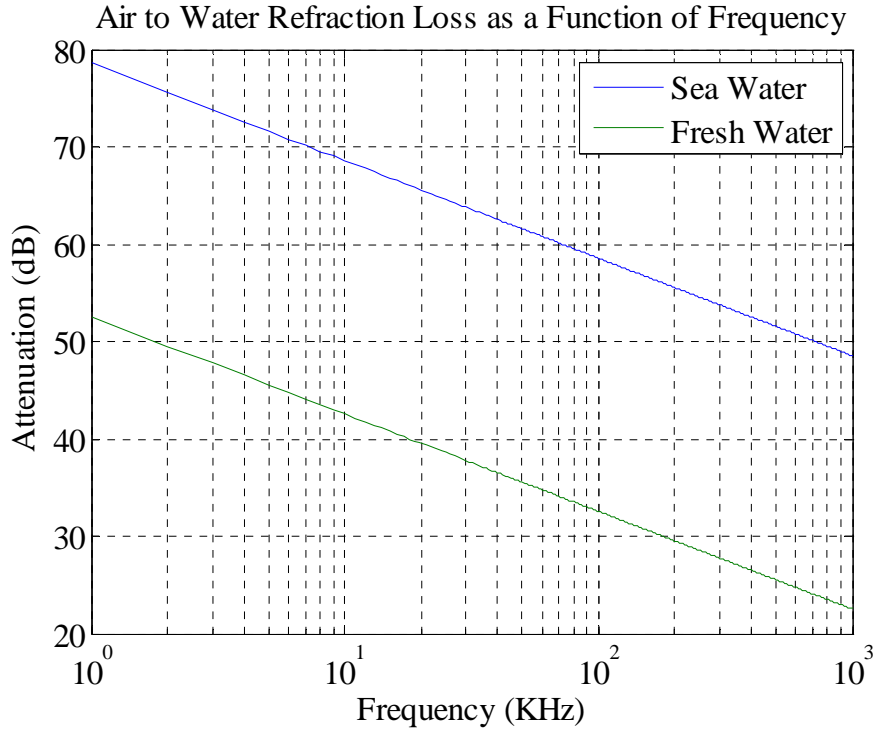


Figure 3.4: **Air to Water Refraction Loss as a Function of Frequency**

Similar communications could be carried out underground depending on the conductivity of the surrounding rock [33, 34].

3.1.4 Existing RF Systems

Because the conductivity of sea water poses severe attenuation to RF signals, only a few systems using RF underwater have been designed. Extremely low frequency (ELF) radio signals have been used in military applications. Germany pioneered radio communications to submarines underwater during World War II, where their "Goliath," antenna was capable of outputting up to 1 to 2 Mega-Watt (MW) of power, strong enough to send signals to submarines submerged in the In-

dian Ocean [36]. Later, a U.S. and Russian ELF system used 76Hz and 82Hz radio frequency signals respectively to transmit a one-way ‘bell ring’ to call an individual submarine to the surface to terrestrial radio for higher bandwidth communication [37].

Until recently it was deemed impractical to use high frequency waves for communication purposes. However, with new antenna designs, recent experiments indicate that radio waves within the frequency range 1-20MHz can propagate over distances up to 100 m, at rates beyond 1 Mbps, using dipole radiation with transmission powers on the order of 100W [38, 39]. The antennas are very different from those used for terrestrial communications [36, 38, 39]; instead of having direct contact with seawater (as terrestrial antennas have direct contact with air), the metal transmitting and receiving aerials are surrounded by waterproof electrically insulating materials [38, 39] allowing an electromagnetic signal to be launched from a transmitter into a body of seawater and picked up by a distant receiver.



Figure 3.5: **Wireless Fibre Systems SeaText Modem**

The first commercial underwater radio-frequency (RF) modem in the world, SeaText (Figure 3.5), was released by Wireless Fibre Systems [40] in September 2006. It can communicate over several tens of meters at a rate of 100bps. Wireless Fibre Systems released a second RF modem, SeaTooth, which can support 1-100 Mbps within a 1 meter range [40].

Table 3.1, provided by [40] shows the possible rates and ranges of the Wireless Fibre Systems RF modems in both sea and fresh water and their potential applications.

Table 3.1: Rates, Ranges, and Uses of Wireless Fibre Systems RF Modems

Range	< 1m	10m	50m	200m	2km	10km
RF (Sea Water)	100 Mbps	100 Kbps	6 Kbps	100 bps	1 bps	1 bps
RF (Fresh Water)	100 Mbps	1 Mbps	100 Kbps	1 Kbps	10 bps	1 bps
Applications	-AUV docking -Wireless connectors	-AUV data download -Diver Comm	-Networking -Diver Comm	-Networking -AUV Control -Diver Comm	-Deep water Telemetry	-Deep water Telemetry

3.2 Optical Waves

Optical waves are electromagnetic waves having wavelengths between 400nm (blue light) and 700nm (red light). Due to their very short wavelength, high frequency, and high speed (light in the ocean travels at a velocity equal to the velocity of light in a vacuum divided by the index of refraction (n), which is typically $n = 1.33$ [41]), optical waves offer the possibility for very high speed communication underwater (up to 1Gbps). However, optical waves used as wireless communication carriers are generally limited to very short distances because of severe water absorption at the optical frequency band and strong backscatter from suspended particles [42]. The section discusses the basic physics of optical waves underwater and existing underwater systems that make use of optical waves.

3.2.1 Physics of Optical Waves Underwater

The amount of light attenuation in sea water can be described by Beer's Law:

$$I(\lambda) = I_0(\lambda)e^{-\kappa(\lambda)d} \quad (3.4)$$

Where $I(\lambda)$ is the intensity of light of wavelength λ observed at the receiver d meters from the source of intensity I_0 . $\kappa(\lambda)$ is the attenuation coefficient which can be approximated as [43]:

$$\kappa(\lambda) = \alpha_w(\lambda) + \zeta_p(\lambda) \quad (3.5)$$

Where $\alpha_w(\lambda)$ is the absorption of water and $\zeta_p(\lambda)$ is the turbidity, a measure

of scattering caused by suspended particles. The scattering of water molecules and absorption of particles may be neglected as they are small enough compared to the parameters in Equation 3.5 [43].

The absorption of pure sea water, $\alpha_w(\lambda)$, is given in Figure 3.6 [44, 45]. Sea water is composed primarily of H₂O which absorbs heavily towards the red spectrum, but also contains dissolved salts such as NaCl, MgCl₂, Na₂SO₄, CaCl₂, and KCl that absorb specific wavelengths [46]. As seen in Figure 3.6, pure seawater is least absorptive around 400-500nm, the blue-green region of the visible light spectrum.

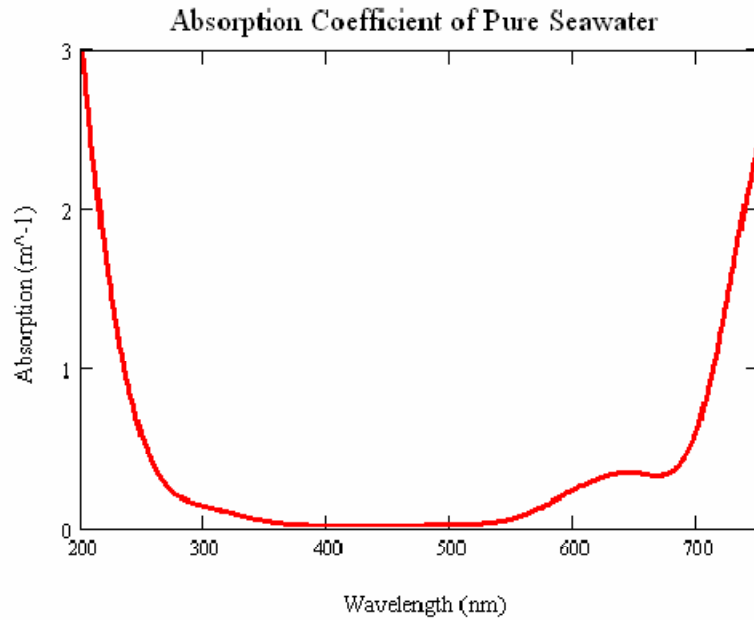


Figure 3.6: **Absorption Coefficient of Pure Seawater** [44, 45]

The scattering process of optical waves and the wavelength dependence of underwater optical channels can be evaluated by the Mie scattering theory which is valid for all possible ratios of particle diameter to wavelength [47]. Scattering in the ocean is due to both inorganic and organic particles floating within the water column. In coastal waters and continental shelf, inorganic matter contributes to 40-80% of the total scattering where in the open ocean scattering comes mainly from organic particles (phytoplankton, etc.), [44]. According to the Mie theory,

light interacts with a particle over a cross-sectional area larger than the geometric cross section of the particle when the light wavelength is similar to the particle diameter. The scattering cross section area, C_{sca} , defined as the total energy scattered by a particle in all directions, as [47]:

$$C_{sca} = \frac{\int_0^{2\pi} \int_0^\pi I_{sca} r^2 \sin\phi d\phi d\theta}{I_0} \quad (3.6)$$

where I_{sca} is the scattered light intensity, I_0 is the incident light intensity, and r is the radius of the particle. The scattering cross section area is related to turbidity as:

$$\zeta = \int C_{sca}(x)p(x)dx \quad (3.7)$$

where x is the particle diameter, $C_{sca}(x)$ is the scattering cross section for particles with diameter x ; and $p(x)$ is the probability distribution function of particle size.

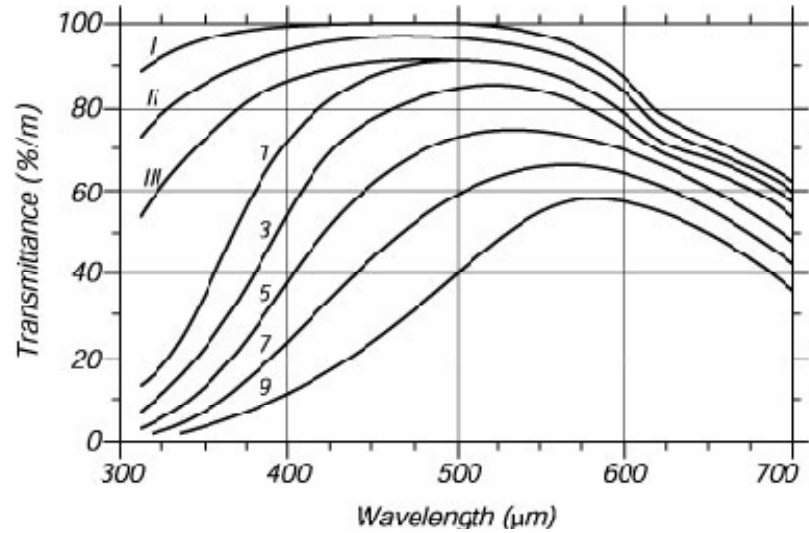


Figure 3.7:

The Spectral transmittance over the upper 10m of water for Jerlov water types I: extremely pure ocean water; II: turbid tropical-subtropical water; III: mid-latitude water; 1-9: coastal waters of increasing turbidity [44, 48]

Figure 3.7 shows the effect of turbidity on optical transmittance across the globe. In 1976, N. G Jerlov published the book *Marine Optics* that proposed a system for classifying the clarity of the water [48]. This system divided the globe's sea water into two categories: oceanic (blue water) and coastal waters (littoral zone). The oceanic group is subdivided into 3 groups; Type I-III and the coastal group are subdivided into Types 1 through 9. Figure 3.7 shows the clarity of oceanic water is much greater than the clarity of coastal water. Oceanic waters are so clear that 10% of the light transmitted below the sea surface can reach a depth of 90m. On the other hand, coastal waters, such as the Baltic sea (under the category of coastal water 3) have large quantities of chlorophyll, causing highly turbid water and a 10% transmittance depth of only 15 m [46].

3.2.2 Existing Optical Systems

Because water clarity plays such a significant role in determining whether optical waves can be used for underwater communication, no commercial underwater optical modems have been developed. However, recent interests in underwater sensor networks and sea floor observatories have greatly stimulated research interest in short-range high-rate optical communication in water [42]. For example, in [50], a dual mode (acoustic and optical) transceiver is used to assist robotic networks where the optical transceiver achieves a data rate of 320 Kbps over a few meters. The optical modem described by Schill et al achieves a range of 2 meters for a rate of 57 Kbps [51]. In [52], an optical modem prototype is designed for deep sea floor observatories and can operate up to 10 Mbps over 100 meters; and in [53] a 1 Mbps LED-based communication system was demonstrated in a 12 foot, 1200 gallon tank. Furthermore, a recent study using Monte Carlo simulations over seawater paths of several tens of meters indicates that optical communication data rates greater than 1 Gbps can be supported and are compatible with high-capacity data transfer applications that require no physical contact [54].

Recent experiments have also involved an acousto-optical hybrid approach which uses laser to make sound underwater. In 2009, the U.S. Navy announced the use of blue/green lasers to produce bubbles of steam that pop and create tiny,

220 decibel explosions [49]. The laser beam incident at the air-water boundary is exponentially attenuated by the medium, creating an array of thermo-acoustic sources relating to the heat energy and physical dimensions of the laser beam in water, thus producing local temperature fluctuations that give rise to volume expansion and contraction. The volume fluctuations in turn generate a propagating pressure wave with the acoustic signal characteristics of the laser modulation signal [55, 56, 57]. Controlling the rate of temperature fluctuations could provide a means of communication.

3.3 Acoustic Waves

Acoustic waves are caused from variations of pressure in a medium. Due to the greater density of water, they travel 4-5 times faster in water than they do in air (traveling in water at an average of 1500 m/s - the speed of sound subject to the water's temperature, salinity and pressure), but are about 5 orders of magnitude slower than electromagnetic waves (traveling near the speed of light as discussed in Section 3.2). They have been widely used in underwater communication systems due to the relatively low attenuation of sound in water. However, acoustic waves can be adversely affected by absorption loss, spreading loss, ambient noise, and severe multipath, which is discussed in this section.

3.3.1 Absorption Loss

The absorption of acoustic waves in sea water depends on the temperature, salinity, and acidity of the sea water as well as the frequency of the sound wave. The absorptive loss for acoustic wave propagation can be expressed as $e^{\alpha(f)d}$, where d is the propagation distance and $\alpha(f)$ is the absorption coefficient of frequency f [42]. For seawater, the absorption coefficient at frequency f in kHz can be written as the sum of chemical relaxation processes and absorption from pure water [58]:

$$\alpha(f) = \frac{A_1 P_1 f_1 f^2}{f_1^2 + f^2} + \frac{A_2 P_2 f_2 f^2}{f_2^2 + f^2} + A_3 P_3 f^2 \quad (3.8)$$

Where the first term is the contribution from boric acid with f_1 as its relaxation frequency, the second term is from the contribution of magnesium sulphate with f_2 and its relaxation frequency, and the third term is from the contribution of pure water. The pressure dependencies are given by P_1 , P_2 , and P_3 and A_1 , A_2 , and A_3 are constants. Figure 3.8 shows the variation in total absorption vs. frequency for different oceans of different temperature, pressure, and pH [59]. Since $\alpha(f)$ increases with frequency, high frequency waves will be considerably attenuated within a short distance while low frequency acoustic waves can travel far.

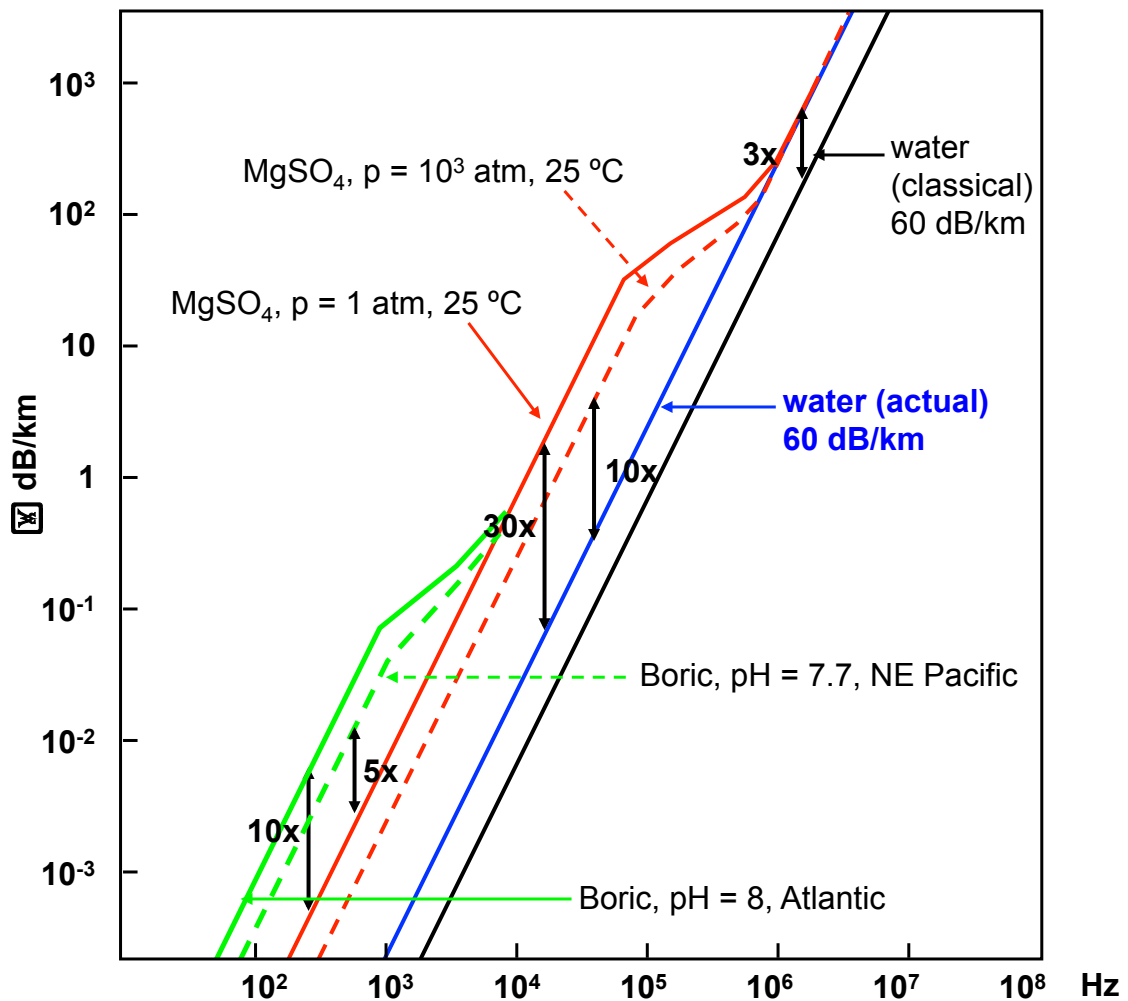


Figure 3.8: Acoustic Absorption as a function of temperature, pressure, and pH [59]

3.3.2 Spreading Loss

The energy radiated from an omni-directional source spreads spherically through a body of water. Since all the energy is not directed in a single direction but in all directions, much of the energy is lost. This is called spreading loss. Note that spreading loss is frequency independent. In deep water, the power loss caused by spreading is proportional to the square of the distance. In shallow water, sound is bounded by the surface and the sea floor resulting in cylindrical spreading. In this case, sound power loss increases linearly with the distance from the source. For a practical underwater setting, the spreading loss falls somewhere between spherical and cylindrical spreading, with power loss proportional to d^β where β is between 1 (for cylindrical spreading) and 2 (for spherical spreading) [60]. In logarithmic terms, the classical equation for spreading loss is $10 \log (d^\beta)$ [60] (see Figure 3.9).

3.3.3 Noise

Ambient noise is defined as “the noise associated with the background din emanating from a myriad of unidentified sources. Its distinguishing features are that it is due to multiple sources, individual sources are not identified, and no one source dominates the received field.” [61] Underwater sound is generated by a variety of natural and man-made sources including breaking waves, rain, marine life, bubbles, surface-ships, and military sonars. The primary source of ambient noise can be categorized by the frequency of sound. In the frequency range of 20-500 Hz, ambient noise is primarily generated by distant shipping, in the range 500-100,000 Hz ambient noise is mostly due to spray and bubbles associated with breaking waves. At frequencies above 100 KHz, thermal noise (noise generated by the Brownian motion of water molecules) dominates.

In 1962 Wenz and colleagues set out to measure background sounds in the ocean and summarized them in a graph showing typical sound levels at different frequencies [62]). (Figure 3.10 was adapted from [62] by [61]. The sound levels in this graph are in dB relative to $1 \mu\text{Pa}$. Thus, when selecting a suitable frequency band for communication, besides path loss, noise should be also considered [63, 64].

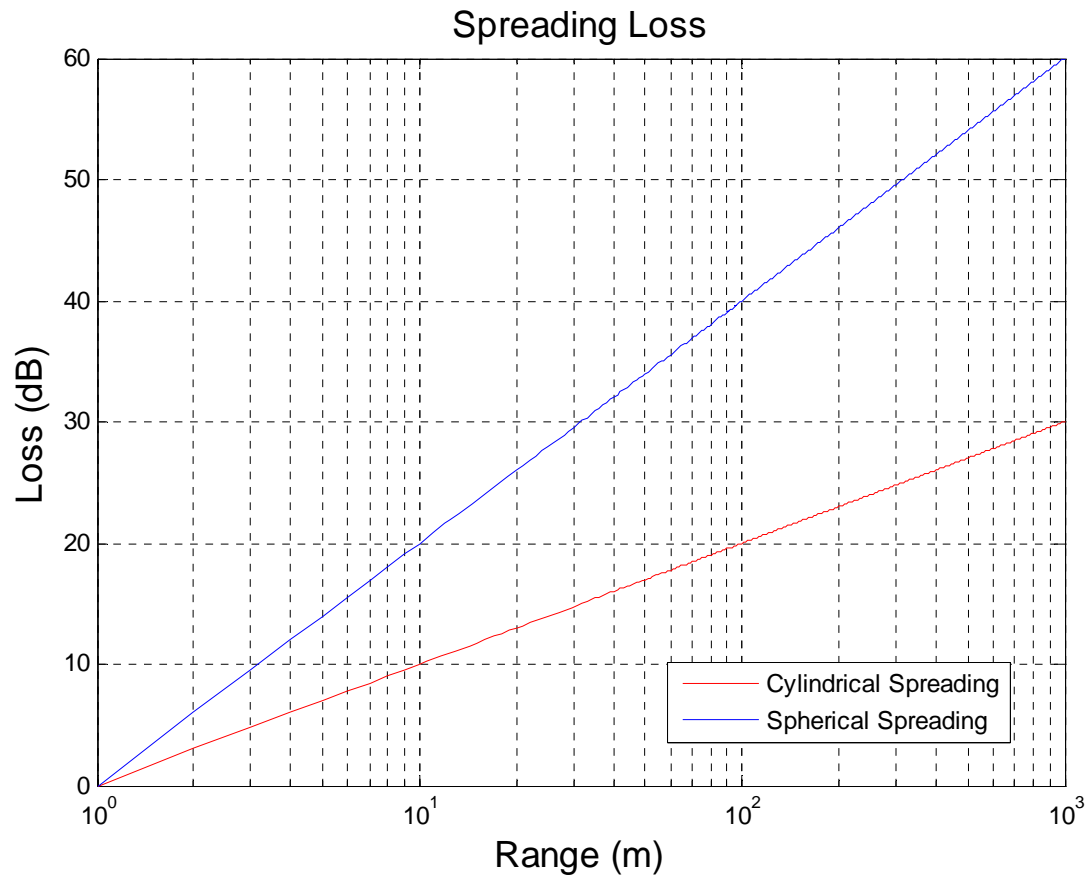


Figure 3.9: Acoustic Spherical and Cylindrical Spreading Loss

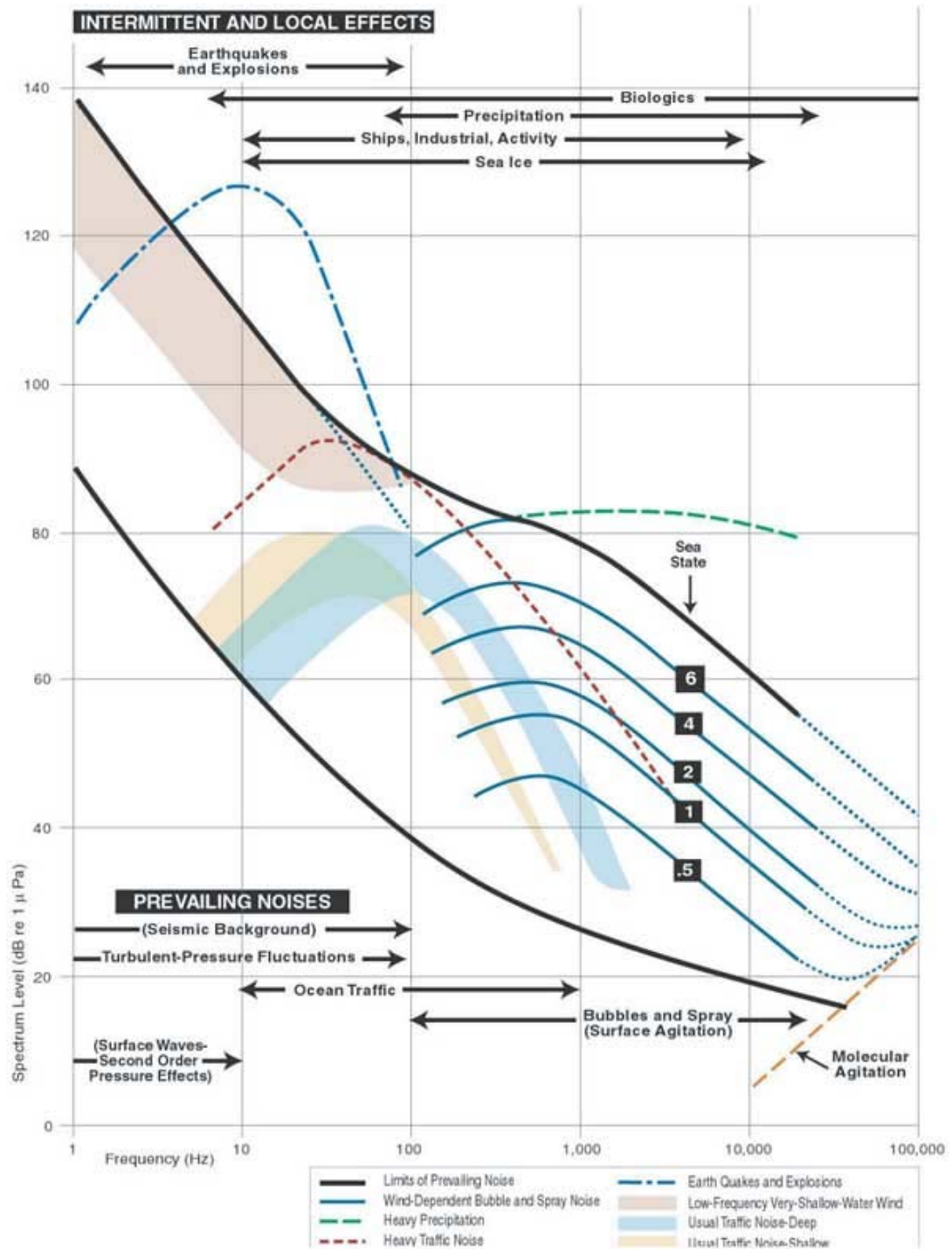


Figure 3.10: The typical sound levels of ocean background noises at different frequencies [61].

3.3.4 Passive Sonar Equation

Given a source level, ambient noise level and equations for absorption and spreading loss, one can use the passive sonar equation to determine the maximum transmission distance achievable for a desired signal to noise ratio at the receiver. The passive sonar equation is given by:

$$SNR(dB) = SL - TL - NL \quad (3.9)$$

Where SNR is the desired signal to noise ratio at the receiver, SL is the source level, TL is the transmission loss due to absorption and spreading, and NL is the noise level attributed to the ambient noise level of the environment and $10 * \log_{10}(SignalBandwidth)$. Figure 3.11 shows the relationship between required source level and range for four different SNR values at the receiver for a 40 kHz carrier with 1kHz bandwidth and an ambient noise of 50 dB re 1 μ Pa (see Figure 3.10).

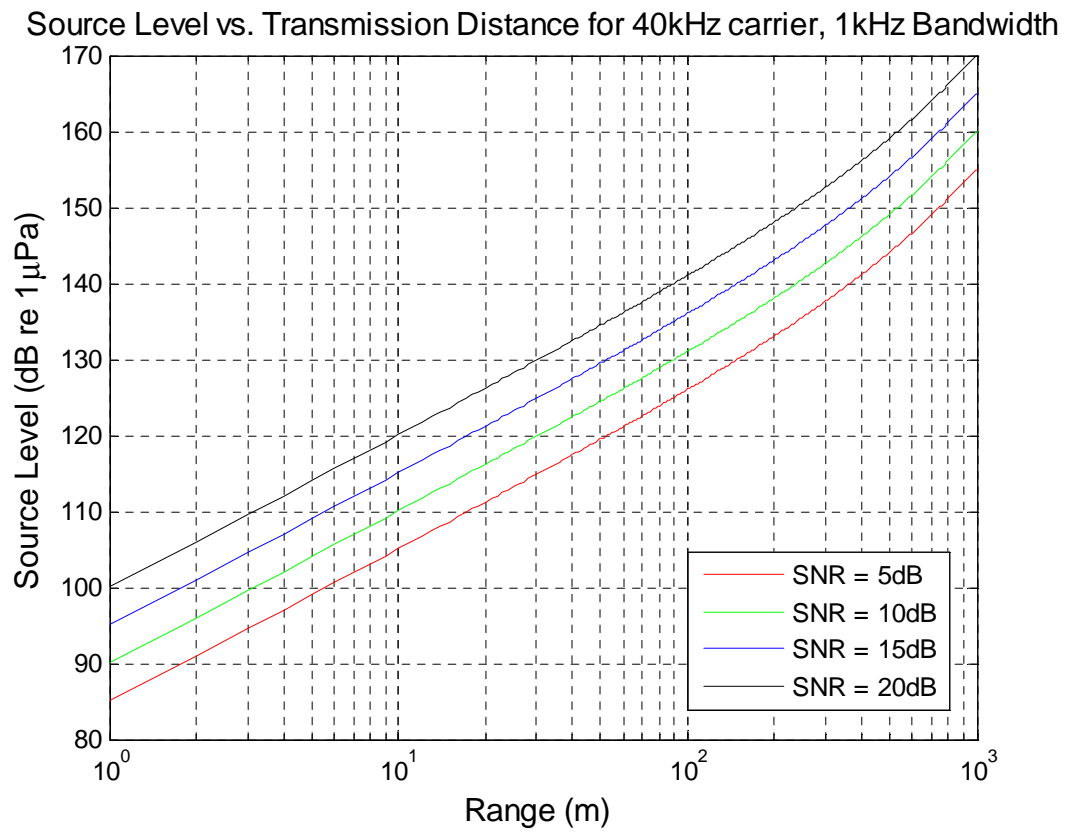


Figure 3.11: Source Level vs. Transmission Distance for a 40 kHz carrier and an ambient noise of 50 dB re 1 μ Pa at various levels of SNR

3.3.5 Multipath

Underwater, there exist multiple paths from the transmitter to receiver, or multipath. Two fundamental mechanisms of multipath formation are reflection at the boundaries (bottom, surface and any objects in the water), and ray bending (as sound speed is a function of temperature, salinity, and depth, rays of sound always bend towards regions of lower propagation speed) [65]. Multipath due to reflections off the surface and bottom is common in shallow waters whereas multipath due to ray bending is common in deep waters. Understanding of these mechanisms is based on the theory and models of sound propagation. Ray theory and the theory of normal modes provide the basis for such propagation modeling.

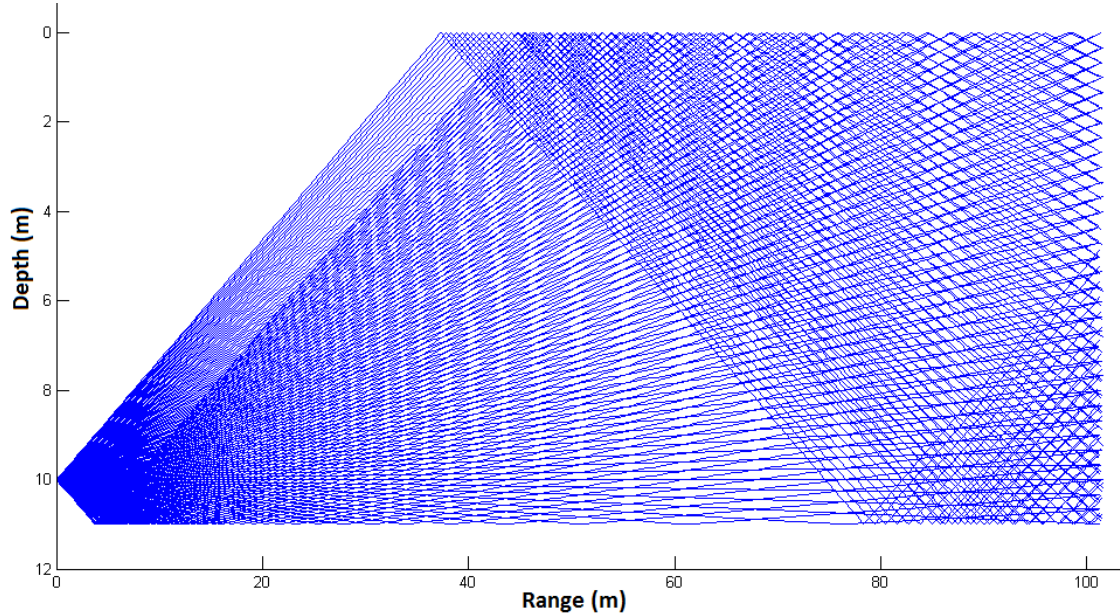


Figure 3.12: **Ray Trace for a 40kHz source with a 15 degree beam angle placed at 10 meters depth in a body of water 11 meters deep with a constant sound speed of 1500 m/s**

Bellhop is a commonly used, highly efficient ray tracing model. The underwater acoustic propagation modeling software, AcTUP [66], can perform two-dimensional Bellhop acoustic ray tracing for a given sound speed profile $c(z)$ or a given sound speed field $c(r, z)$, in ocean waveguides with flat or variable absorbing boundaries. Output options include ray coordinates, travel time, amplitude,

acoustic pressure or transmission loss. Figure 3.12 shows the Bellhop ray tracing model for a 35kHz source with a 15 degree beam angle placed at 10 meters in a body of water 11 meters deep with a constant sound speed of 1500 m/s.

Multipath can adversely affect communications because a large delay spread (the time difference of arrival of the first and last path at the receiver) introduces time dispersion of a signal, which causes severe inter-symbol interference. Typical underwater channels may have a delay spread around 10ms, but occasionally delay spread can be as large as 50 to 100ms [67] or as small as 3 ms [68]. The delay spread of a receiver placed at 10m, 100m from the source in Figure 3.12 is only 300 microseconds.

3.4 Summary

This chapter described the effect of the underwater environment on RF, optical and acoustic waves. Table 3.2 (based on information in Tables II and III in [42]) summarizes and compares the characteristics of radio, optical, and acoustic communication underwater. All three physical wave fields have their own advantages and limitations for acting as an underwater wireless communications carrier; radio waves can provide high data rates, but are subject to strong attenuation by the conductivity of sea water, optical waves provide even higher data rates, but are subject to attenuation by the turbidity of sea water, acoustic waves provide long transmission distances but support relatively low data rates and are subject to multipath. As our sensor network applications (described in Chapter 2) require low data rates and transmission distances greater than 100 meters, acoustics remains the most robust and feasible carrier to date for wireless communication in these underwater sensor networks. As acoustics have been widely used in underwater communications and we have selected acoustics for our modem design, the next chapter is devoted to describing and comparing existing commercial and research underwater acoustic modems.

Table 3.2: Comparison of RF, optical and acoustic communication underwater

	RF	Optical	Acoustic
Wave speed (m/s)	$\sim 3E8$	$\sim 3E8$	$\sim 1.5E3$
Data rate	< 10 Mbps	< 1 Gbps	< 100 Kbps
Effective range	$\sim 1-100$ m	$\sim 1-100$ m	\sim km
Power Loss	~ 28 dB/1km/100MHz	\propto turbidity	> 0.1 dB/m/Hz
Frequency Band	\sim MHz	$\sim 10^{14} - 10^{15}$ Hz	\sim kHz
Major hurdles	power limited	environment limited	bandwidth limited interference-limited

Chapter 4

Existing Underwater Acoustic Modems

As stated in the previous chapter, acoustic waves are widely used in underwater communication systems due to the relatively low attenuation of sound in water. Thus, quite a few companies and research groups have developed underwater acoustic modems for various undersea applications. This chapter describes and compares existing commercial and recent research underwater acoustic modems to better illustrate the novelty and applicability of the UCSDmodem design.

4.1 Commercial Modems

Commercial underwater acoustic modems are used by major offshore oil companies, commercial survey companies, government agencies, universities and defense contractors. This subsection discusses modems that are currently in production and available for purchase. We focus on six commercial companies - LinkQuest, Teledyne Benthos, TriTech International, Aquatec Group, EvoLogics, and DSPComm, and the open architecture Micro-Modem developed at the Woods Hole Oceanographic Institute (WHOI). In each case, we highlight the benefits, use scenarios, and drawbacks of the modems.

LinkQuest claims to be the underwater acoustic modem market leader. They produce a number of modems [69] ranging from the UWM1000 (a shallow

water, low power (2W transmit, 0.75 W receive) modem that can communicate up to 350 meters with a data rate of 9600 to 19200 bps) to the UWM10000 (a full ocean range and depth modem (40 W transmit, 0.8 W receive) that can communicate up to 10 km with a data rate of 2500 to 5000 bps). The data rates vary primarily as a function of the environment -a higher noise, higher multipath environment having a lower data rate. As LinkQuest offers quite a range of modems, they can be suited to many applications, however, their smallest and least expensive modem (the UWM1000) costs \$6500. LinkQuest also uses a proprietary signaling format which causes concerns about interoperability between sensor nodes and inhibits competition potentially increasing cost in the long term.

Teledyne Benthos manufactures modems that have been used in sub-sea networks including the US Navy Seaweb program [10, 11], and the Front Resolving Observation Network (FRONT) [9]. Their modems are marketed primarily for point-to-point deep water vertical communication, e.g. from ocean floor directly to the ocean surface [70]. They have demonstrated communication in over 1 kilometer of water at 10240 bits/second with no errors in ideal situations; however they claim typical data rates less than 2400 bits/second. The modems are also relatively power-hungry consuming 28-84 W transmit power and 0.7 W receive power. Furthermore, the modems are quite expensive, costing over \$7000.

TriTech International developed the Micron Data Modem [71] for small remotely operated vehicle (ROV) communications. The Micron Modem appears to be the smallest and lightest acoustic modem on the market thus making it suitable for applications that have size and weight constraints (such as on board small AUVs or ROVs). It is also half the cost of other acoustic modems on the market with a retail cost of \$3360. However, the Micron Modem has moderate power consumption (7.92 W transmitting and 720mW receiving) for a maximum range of 1km and low data rate (40 bps).

The Aquatec Group is a company that designs acoustic modems tailored to suit the application of interest [72]. As part of their AquaModem long-range series, they can offer modem configurations that provide a bit rate of 300-2000 bps and a range of up to 20km. As part of their AquaModem500 short-range series,

they can offer modem configurations that provide a bit rate of 25-100bps, a range of up to 250 meters. Modem costs start at \$7600.

EvoLogics developed six underwater acoustic modems that make use of their patented sweep spread carrier (S2C) underwater technology [73]. S2C was designed to mimic a dolphin's sound pattern and continuously spread the signal energy over a wide range of frequencies so that the multipath components do not interfere with each other. Their modems range from high speed modems (28kbps) for small to medium range applications (1000 meters) in shallow water to long distance (8km), lower data rate (6.5kbps) in deep water. Costs once again vary depending on modem configuration.

DSPComm produces the AquaComm, an underwater wireless modem that provides the user with the ability to set the receive and transmit power thus offering a low-power solution for short range applications [74]. The AquaComm has been tested to a range of 3km and offers data rates of 100 or 480 bps depending on the model. A 100 bps model costs \$2800 and a 480bps model costs \$3500 for the electronics. The transducer and plastic case cost an additional \$3100.

The Woods Hole Oceanographic Institute (WHOI) Micro-Modem [75] is a popular open architecture alternative to the commercial solutions. It is user-programmable and can support multiple instruments. It is currently used for communication and navigation of autonomous underwater vehicles and autonomous surface vehicles, buoy sensor telemetry and deep-water ocean observatories. The Micro-Modem employs frequency-hopping frequency shift keying (FH/FSK) or phase-shift keying (PSK) at the physical layer. FH/FSK is used in difficult channels, e.g. shallow water, littoral zones, communication to/from autonomous underwater vehicles (AUVs), at low data rates (80bps). PSK is used for relatively simple channels, e.g., deep water sea floor to surface, at higher data rates (up to 5400 bps). The modem electronics (without a water proof housing) cost \$4900 with an additional \$1200 for the PSK co-processor. The transducer and cable assembly for the modem costs \$3200.

Table 4.1 compares modems from each of the above mentioned companies in terms of operating frequency, transmit power, range, receive power, modulation

scheme, bit rate, and cost. For values not specified in the literature we denote 'NS.' The cost estimates were obtained from requesting a quote from each company (note that the costs may vary depending on the actual hardware components selected for the modem including the transducer and housing). Operating frequencies range from 8kHz - 78kHz (using lower frequencies to obtain longer ranges), transmit powers vary from 2.5W - 80 W depending on the range, bit rate, and modulation scheme, and bit rates range from 40-15000 bps. All modems make use of proprietary commercial transducers which alone cost a few thousand dollars, contributing a large portion to the overall cost of the modem. The last line of the table denotes the properties of the UCSDModem design showing it provides less range, lower bit rate and comparable power to most available commercial modems, but costs an order of magnitude less. Note that the cost of the full UCSDModem is solely for parts and does not include labor or market price, however, the parts cost for the entire modem is still less than the cost of the commercial transducers used in the other modem designs. Additional commercial modem comparisons may be found in [76].

Table 4.1: Commercial Underwater Acoustic Modem Comparison

Company	Modem	Frequency (kHz)	Tx Power (W)	Range (km)	Rx Power (W)	Mod	Bit Rate (bps)	Cost (\$)
Aquatec	AQUAModem	8-16	20	10	0.6	DSSS	300-2000	> 7600
DSPComm	AquaComm	16-30	varied	3	varied	DSSS/OFDM	480	6600
TriTech	MicronModem	20-24	7.92	0.5	0.72	DSSS	40	3500
WHOI	MicroModem	25	<50	1-10	0.23 / 2	FSK/PSK	80/5400	8100/9400
Benthos	ATM885	16-21	28-84	2-6	0.7	FSK/PSK	140-15360	7200-11000
EvoLogics	S2CM48/78	48-78	2.5-80	1	0.5	S2C	15000	12500
LinkQuest	UWM2000H	NS	1.5	0.8	NS	Proprietary	9600	7000
UCSD	UCSDModem	40	1.3-7.0	400	0.42	FSK	200	350*

* Component cost estimate only

4.2 Research Modems

Research underwater acoustic modems have been designed with the objective of reducing power consumption or cost or with the objective of testing new communication algorithms to increase bit rate or better counter the effects of harsh environments. This section presents an overview of some of the research modems that have been designed in the past decade.

The University of Southern California's Information Sciences Institute designed a prototype modem for the Sensor Networks for Undersea Seismic Experimentation (SNUSE) project [77]. Their primary design goal was to provide an inexpensive, low power modem to operate over 50-500 meters for seismic monitoring applications. To accomplish their objective, the prototype included an inexpensive ultra low-power wake up receiver that consumes only 500 microWatts and an inexpensive off the shelf 8-bit microcontroller and radio frequency integrated circuit for control and frequency shift keying based communication. They did achieve a prototype costing less than \$100 with a maximum transmit power of 2W, receive power of 25mW, and idle power of 500uW, but could only perform in-air testing with the hardware they designed.

Researchers at the University of California Irvine proposed the use of software acoustic modems running on generic speakers and microphones to establish acoustic communications for underwater sensor networks with the idea that the use of generic hardware can greatly reduce the cost of the modem design [78]. Their frequency shift keying based modem design implemented on the Tmote Invent module [79] can achieve a bit rate of 24 bps at a 10 meter range or 48 bps at a 3 meter range in water.

The AquaModem [80], designed at the University of California Santa Barbara, was designed for short range ($< 1\text{km}$) eco-sensing applications in a shallow horizontal underwater channel. The AquaModem uses M-ary direct sequence spread spectrum signaling, with joint detection and channel estimation performed by matching pursuits to effectively handle multipath interference. It was implemented on a TI TMS320C6713 DSP and made use of custom made \$2500 transducers with a center frequency of 24kHz and a double-sided bandwidth of 7.8 kHz.

The modem was field tested in a shallow water coral reef and achieved ranges up to 440 meters with a bit rate of 133 bps and an uncoded symbol error rate $< 1\%$ [81].

Researchers at Kookmin University, Korea, designed an underwater acoustic modem that makes use of four small air transducers to communicate to other nodes facing to the north, east, south, and west respectively and a fifth transducer to communicate to a surface node. The design uses an ATmega128 as its microcontroller unit which interfaces to an Arm PXA270 processor for medium access layer (MAC) control. It operates at 30kHz and is capable of transmitting data up to 5 kbps at ranges up to 30 meters [82].

Vasilescu et. al developed the AquaNode that is dually networked: optically for point-to-point transmission at 330 kbps and acoustically for broadcast communication over ranges of hundreds of meters at 300 bps [83]. The acoustic modem is are built around an Analog Device Blackfin BF533 fixed point DSP processor and uses FSK modulation on a 30kHz carrier frequency. The nodes self-localize and can be used to form static undersea networks. With all the nodes running at full power, the battery provides 1-2 weeks of continuous operation.

Researchers at the University of Connecticut designed an orthogonal frequency division multiplexing based modem on a TMS320C6713 DSP with the goal of providing a higher data rate solution to other research modems [84]. The modem is capable of transmitting data at a raw data rate 3.1 kbps after rate 1/2 nonbinary LDPC coding and QPSK modulation. The modem has been tested in water in a lab test tank, but has not been field tested, thus no range information is available [85]. Researchers at Northwestern Polytechnical University in China also designed a DSP based OFDM modem, implementing the design on a ADSP-TS101 and achieving an uncoded bit rate of 1kbps in a lake (range not specified) [86].

Sozer and Stojanovic developed a reconfigurable acoustic modem (rModem) [87] designed to act as a physical layer prototyping platform. This platform includes a high processing power floating point DSP for the implementation of various physical layer protocols and an FPGA that enables users to operate at any carrier frequency and bandwidth within the 1kHz - 100kHz band by setting carrier coeffi-

cients, filter coefficients, and interpolation/decimation rates. The current rModem design interfaces to a daughter card that can drive a Teledyne AT-408 transducer that operates in the 9-14kHz band. Because the rModem is intended to be used as a research tool rather than a commercial product, high processing power and cost is tolerated. The rModem hardware and software operability was field tested in Woods Hole, MA [88]. Similar to the rModem is the Universal Software Radio Peripheral (USRP) underwater modem proposed to act as a solution for research in implementing underwater modems and related signal processing [89].

Numerous other researchers have implemented communication algorithms on a laptop computer and used commercially bought hardware to connect to the laptop and conduct in-water experiments. Examples include OFDM based implementations [90, 91, 93, 94, 95, 96] and multiple-input, multiple-output (MIMO) based implementations [97, 98, 99]. These designs are useful for examining the capabilities of different modulation schemes, but are not designed for real-time deployment.

Table 4.2 compares the described research modems in terms of platform, modulation scheme, bit rate, and range. ‘NS’ denotes values not specified in the literature. The last line of the table denotes the properties of the UCSDModem design showing it provides similar rate and range performance to the AquaModem and AquaNode, but was designed with low-cost as the primary design goal. The UCSDModem design is also the only research modem design to implement FSK on an FPGA.

4.3 Summary

This chapter described and compared existing commercial and recent research underwater acoustic modems. The modem described in this thesis differs from the commercial and research modems described above in that it focuses on obtaining a cost-effective solution while still providing sufficient bit rate and range. The design substitutes a commercial underwater transducer with a home-made underwater transducer using inexpensive piezoceramic material and builds the rest

of the modem's components around the properties of the transducer to extract as much performance as possible. It is also the first design to implement frequency shift keying on a field programmable gate array for underwater acoustic communication. The following 3 chapters describe the design details of each component of the UCSDModem, including the low cost transducer, the analog transceiver and digital transceiver.

Table 4.2: Research Underwater Acoustic Modem Comparison

Modem	Platform	Mod	Bit Rate	Range	BER	Comments
USC	MCU	FSK	NS	NS	10^{-5} (coded)	in air tests only low-power wake up circuit
UCI	Tmote	FSK	12	5	10%	uses generic hardware
uConn	DSP	OFDM	6200	NS	NS	for increased bit rate tank tests only
rModem	DSP	varied	varied	varied	NS	prototyping platform
AquaModem	DSP	DSSS	133	440	1%	for high multipath
Kookmin	MCU	NS	5000	30	NS	for very short range
AquaNode	MCU	FSK	300	400	NS	dual networked functionality
UCSD	FPGA	FSK	200	400	4%	for low cost

Chapter 5

Transducer Design

This chapter describes the design of our low-cost transducer, an electromagnetic device responsible for converting electrical energy to mechanical energy (sound pressure) and vice versa. We first describe the selection of the transducer's piezoceramic based on its type and geometry. We then describe our transducer construction techniques including the selection of wiring, potting compound, and mold. We finally describe the procedures used to measure the electromechanical properties of our homemade transducer and present the experimentally determined electromechanical properties that are used to govern the rest of the UCSDModem design.

5.1 Piezo Ceramics

In 1880, Jacques and Pierre Curie discovered that certain naturally occurring crystalline substances (such as quartz) exhibit an unusual characteristic: when subjected to a mechanical force, the crystals became polarized and when exposed to an electric field the crystals lengthened or shortened according to the polarity and in proportion to the strength of the field. These behaviors were labeled the piezoelectric effect and the inverse piezoelectric effect, respectively [100, 103, 102].

In the 20th century, researchers began to manufacture synthetic materials that exhibit the piezoelectric effect using polycrystalline ceramics or certain synthetic polymers. These materials are relatively inexpensive to manufacture, phys-

ically strong, and chemically inert. Common compositions include lead zirconate-titanate and barium-titanate [100]. The type of the ceramic and its geometry affect the ceramic's piezoelectric properties and are described in more detail in the following subsections.

5.1.1 Type

Although several standards exist, in the US, piezoceramics are popularly classified into 6 types created by DOD-STD-1376A [104] which was replaced by MIL-STD-1376B [105] in 1995 and discontinued in 1999. Although the standard is no longer officially used, most ceramics manufactures still use it as a guideline and have options of their product that comply with the standard. If a ceramic is chosen from one type, it will be very similar in properties to other ceramics in the same type. The typical properties of each type are [105]:

- *TYPE I*- A modified lead zirconate-titanate composition generally recommended for medium- to high-power acoustic applications. Its "resistance" to depoling at high electric drive and/or mechanical stress makes it suitable for deep-submersion acoustic applications.
- *TYPE II*- A lead zirconate-titanate composition modified to yield higher charge sensitivity but one that is not suitable for high electric drive due to dielectric heating. This material is more suitable for passive devices such as hydrophones. Advantages also include better time stability.
- *TYPE III*- Similar to Type I but greatly improved for use at high electric drive because of lower losses. Its field dependency of dielectric and mechanical losses is substantially reduced. However, at low to moderate electric drive levels Type I material may actually be a better choice because of greater electromechanical activity.
- *TYPE IV*- A modified barium-titanate body for use in moderate electric-drive applications. It is characterized by lower piezoelectric activity and lower Curie temperature than any of the lead zirconate-titanate compositions.

- *TYPE V*- A composition intermediate to Types II and VI and thus to be used accordingly.
- *TYPE VI*- Similar to Type II with higher charge sensitivity and dielectric constant, at the expense of a reduced Curie temperature.

The six types of ceramics can be further lumped into two very general groups: hard and soft ceramics. Hard ceramics have low dielectric and mechanical loss and are generally better at producing a signal whereas soft ceramics have large dielectric losses, low mechanic quality factors, and poor linearity, but are generally better at receiving a signal [100, 101]. Soft ceramics produce large displacements and wider signal bandwidth, but they exhibit greater hysteresis and are more susceptible to depolarization [100]. Either of these ceramics is still capable of producing and receiving signals regardless of which group it is in because of piezoelectric reciprocity. For underwater network communication where one transducer is used for transmitting and receiving for cost effectiveness, a piezoelectric element that is good at doing both is desired.

We selected to use a ‘hard’ modified Navy Type I ceramic due to its low dielectric and mechanical loss and high electromechanical coupling efficiency making it suitable as both a transmitter and receiver. Also, ceramics manufactured from formulations of lead zirconate-titanate (PZT) are the most widely used because they exhibit greater sensitivity and higher operating temperatures, relative to ceramics of other compositions [102]. A typical Type I PZTs can experience up to 12 Vpp AC per .001 inches wall thickness without much effect to its electromechanical properties [106]. A thickness of 0.1 inches (2.54 mm) gives a maximum voltage of 1200 Vpp or 425 Vrms.

5.1.2 Geometry

After selecting the type of ceramic necessary for the application, the geometry selection is the next important step. The cost of the PZT element can vary greatly and is significantly affected by geometry. Not only are some shapes harder to make, more intricate shapes make poling the ceramic more difficult as well.

Element geometry and polarization direction determine the radiated direction of acoustic signals as well as the electro-mechanical properties of the ceramic element itself, such as resonance frequency, capacitance, generated voltage under load, and displacement. Exactly how they are affected depends on the geometry selected. Simplified equations for commonly used shapes can be found on many ceramic manufactures' websites [101, 102]. Geometry- independent properties include the electromechanical coupling coefficient, piezoelectric constants, dielectric constant, curie temperature, and dissipation factor which depend on the material.

For underwater communication, ceramics are usually omni-directional in the horizontal plane to reduce reflection off the surface and bottom [103]. A radial expanding ring provides 2D omni directionality in the plane perpendicular to the axis and near omni directionality in planes through the axis only if the height of the ring is small compared to the wavelength of sound being sent through the medium. Note, if the ring is too tall, extension along the axis and bending modes of the ring may become a problem [103].

A radial expanding ring ceramic element can be made of several ceramics cemented together, providing greater electromechanical coupling, power output, and electrical efficiency than one-piece ceramic rings. The piezoelectric constant and coupling coefficient are approximately double that of a one-piece ceramic ring [103]. They work better because the polarization can be done in the direction of primary stresses and strains along the circumference. However, these are much more difficult to manufacture and are therefore much more expensive than a one-piece radial expanding piezoelectric ceramic.

Thus, a one piece modified Type I ring transducer with radial resonance mode, 26 mm outer diameter, 22 mm inner diameter, and 2.54 mm wall thickness was selected. Specifically, part SMC26D22H13SMQA from Steiner and Martins, Inc. [108] was purchased for approximately \$10 per element with no minimum purchase. This is much less than many other piezoelectric manufactures charge for ceramics with very similar geometry and electro-mechanical properties. Much of the cost difference stems from the difficulty of manufacturing PZTs with consistent properties under tight tolerances. Many piezoceramics for underwater communi-

cation are being used for oil and military use where they must comply with tight specifications and operate under extreme conditions. These extreme conditions include deep ocean and long range operation. Thus many companies cater towards this market selling high quality parts that are not necessarily needed for short-range underwater communication research. In this context lower quality does not mean lower performance, but a looser control on tolerances and increase in availability to drive down costs.

For a single radial expanding ceramic ring, the resonance frequency occurs when the circumference approximately equals the operating wavelength [103]. The resonance frequency and anti-resonance frequency occur at minimum and maximum impedances, respectively [103, 107]. In air, the resonance frequency is about 41 kHz for every inch in diameter; for the ring made of several ceramics cemented together, in the case that there is not inactive material (such as electrodes or cement), the resonance frequency is approx 37 kHz for every inch [103]. If the ring is too tall, problems with length extensional and bending modes of vibration may be experienced. The bandwidth of the ceramic is broader if the thickness is much smaller than the radius [103]. The SMC26D22H13SMQA has an outer diameter of 26mm (approx 1 in) and has a nominal resonance frequency of about 43 kHz. Steiner and Martins, Inc. specifies that the ceramic ring has a nominal resonance frequency of 43kHz +/- 1.5kHz.

5.2 Transducer Construction

Although the piezoelectric element is a key component of the transducer, there are other aspects to manufacturing a transducer that are important to its performance. Attaching electrical leads, reducing unwanted acoustic radiation, and potting the piezoceramic should be paid special attention. Figure 5.1 depicts our raw piezoceramic, transducer before potting, and fully potted transducer.

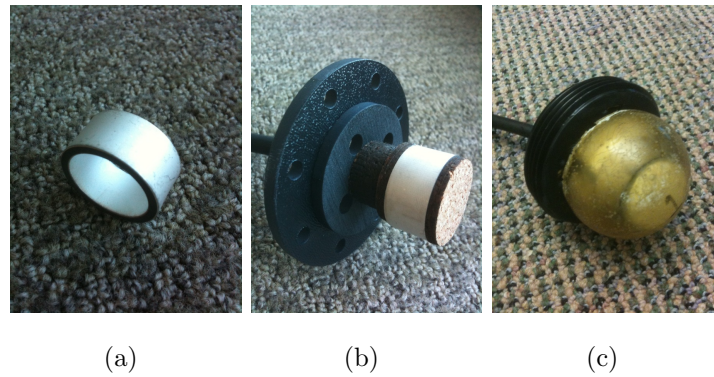


Figure 5.1:

(a) Raw PZT , (b) Pre-potted Transducer , (c) and Potted Transducer

5.2.1 Wiring

Using shielded cables to attach to the ceramic will greatly enhance the performance of the transducer. Unshielded wires can act as antennas and pick up much unwanted electromagnetic noise that can bury small signals received by the transducer. When soldering to the ceramic's electrodes, care should be taken to prevent contact of the soldering tip to the ceramic for more than a few seconds. Heating the ceramic above its curie temperature will damage its electromechanical properties. If possible, the soldering iron's temperature should be also be adjusted accordingly. Solder with 3% silver is recommended by Steminc [108].

5.2.2 Potting

The piezoelectric ceramic needs to be encapsulated in a potting compound to prevent contact with any conductive fluids. Urethanes are the most common material used for potting because of their versatility. The most important design consideration is to find a urethane that is acoustically transparent in the medium that the transducer will be used; this is more important for higher frequency or more sensitive applications where wavelength and amplitude is smaller than the thickness of the potting material. Many urethane manufactures do not know the acoustical properties of their urethanes. However, information on similarities to water's acoustical properties is becoming easier to find. Generally, similar density

provides similar acoustical properties. Mineral oil is another good way to pot the ceramics because it is inert and has similar acoustical properties to water. Some prefer using mineral oil to urethane because it is not permanent. However, the oil still needs to be contained by something, which is often a urethane tube. A two-part urethane potting compound, EN12, manufactured by Cytex Industries [109] was selected as it has a density identical to that of water, providing for efficient mechanical to acoustical energy coupling.

Creating a transducer by potting the ceramic shifts its resonant frequency due to the additional mass moving immediately around the transducer. The extent of the shift depends on the type, age, and amount of potting as well as the temperature and mixing method of the compound. Having tight control over these variables to ensure exact reproducibility requires expensive equipment. To keep costs low, we used the following simplistic potting method.

As urethanes are toxic, when potting the ceramic, avoid touching or inhaling the fumes of the urethane compound as specified by the MSDS provided by the manufacture. Urethanes must have the correct ratio of both parts. Adding more of one will not help it cure faster, will change its physical properties, and many times will prevent it from fully curing at all. A scale was used to measure the exact proportions of the two part compound and hand-poured the parts into a plastic container for mixing. Larger batches will help with keeping mixing ratios more consistent between separate batches.

Urethanes are very susceptible to moisture absorption. The moisture creates bubbles within the urethane and are undesired because they absorb acoustic waves propagating from the piezoceramic. Much of the moisture is introduced during mixing. Using plastic or metal spoons and containers over paper or wooden ones during mixing will reduce the amount of bubbles that appear in the cured urethane. Unmixed urethane in opened containers are often stored in metal cans and covered with a blanket of nitrogen to reduce moisture absorption [110].

Although this was not done on our own transducer, placing a vacuum on the urethane mixture while curing will cause many of the bubbles to enlarge and rise out of the curing liquid. In addition, the curing urethane can subsequently

be placed under pressure to reduce the remaining bubbles' size. Higher vacuums and putting unmixed urethane components into a vacuum separately may cause boiling of certain chemicals that need to remain in the liquid components in order to cure [110]. Again, processing parameters in the urethane's technical specifications should be followed for best results. Tips on making molds, and other potting tips can be found at [111].

A tennis ball with a hole cut in it and an ABS pipe cap with holes drilled in it were glued together using silicone and used as our transducer's mold. The ABS cap was only used for mounting. Mixed and uncured urethane was poured into the mold through the holes in the ABS cap. After the urethane was fully cured the tennis ball and silicone were removed.

5.2.3 Reducing Unwanted Acoustic Radiation

For a ring transducer with radial acoustic radiation, only pressure waves from the outer surface are desired. Pressure waves formed at the top, bottom, and inner surfaces create pressure waves that are out of phase with those formed by the outer surface leading to destructive interference in the far field regime. For this reason many cylindrical transducers are constructed with air or other acoustic damping material within the piezoceramic. Cork was used for our transducer (as shown in Figure 5.1(b)). Discs of cork with an adhesive backing were placed on the top and bottom surfaces of the piezoceramic as well, to absorb radiation from these surfaces.

At depth, having a pocket of air in the transducer can be problematic. For deep water cylindrical transducers, end caps are often made of metal plates or curved ceramics to withstand pressures at depth; to prevent clamping sometimes a rod is run along the cylinder's axis [103]. The end caps should be acoustically isolated from the piezoelectric ceramic. If the circumferential stress (the quantity of pressure multiplied by radius over thickness) is above 10000 to 15000 psi the piezoceramic's parameters will start to deteriorate [103]. The pressure at 100m depth is only about 150 psi above the pressure at sea level. Free flooded rings are still used for some deep water circumstances.

5.2.4 Material Costs

The material cost of each of our transducers was less than \$45 excluding the ABS mounts which are not necessary. The Steminc PZT (SMC26D22H13SMQA) cost \$10 each with no minimum order. The Cytec EN12 potting compound cost \$150 per quart. A 100ft roll of shielded cable (C1202-100-ND) from Digikey cost \$130, and adhesive backed quarter and eight inch thick 1x3 feet cork sheets (9487K51 and 9487K54) cost \$6 and \$13 respectively. The mold's costs are relatively low as well; tennis balls can be purchased for less than \$2 per ball.

The next section describes the procedures used to determine the electromechanical properties of the homemade transducer.

5.3 Calibration Procedures

The calibration of a transducer consists of the determination of its electromechanical response as a function of frequency; namely its transmitting voltage response (TVR) and its receiving voltage response (RVR). The TVR is defined as the sound pressure level experienced at 1m range, generated by the transducer per 1 V of input voltage as a function of frequency. The RVR is a measure of the voltage generated by a plane wave of unit acoustic pressure at the receiver and is a function of frequency. The units of the transmitting response are typically expressed in dB/1uPa/m and the units of the receiving response are typically expressed in dB/1V/uPa. Although numerous calibration procedures exist [112], the following subsections describe the two most commonly used methods: comparison method and reciprocity method.

5.3.1 Comparison Method

The comparison method is the simplest transducer calibration procedure wherein the output of the unknown transducer is compared with that of a previously calibrated reference transducer. The unknown and reference transducers are placed in a tank of water at known separation (typically 1 m). To obtain the RVR, the reference transducer sends sinusoidal signals of a known duration across

the desired frequency range and the unknown transducer collects the sinusoidal signals over the same duration at each frequency. The collected data represent the combination of the transmitting response of the reference transducer plus the receiving response of the unknown transducer and the effects of attenuation at the separation distance. The RVR may be calculated using the following equations :

$$D = 20\log_{10}\left(\frac{V_{receiver}}{V_{transmitter}}\right) \quad (5.1)$$

$$RVR = D_{from.ref} + TVR_{ref} + A \quad (5.2)$$

where $V_{receiver}$ is the average amplitude voltage of the receiver over the known duration, $V_{transmitter}$ is the average amplitude voltage of the transmitter over the known duration and A is the attenuation of the signal due to the separation distance.

To obtain the TVR, the unknown transducer sends sinusoidal signals of reference duration across the desired frequency range and the reference transducer collects the sinusoidal signals over the reference duration at each frequency. The collected data represents the combination of the transmitting response of the unknown transducer plus the receiving response of the reference transducer and the affects of attenuation at the separation distance. The RVR may similarly be calculated as:

$$TVR = D_{to.ref} - RVR_{ref} + A \quad (5.3)$$

5.3.2 Reciprocity Method

As the reciprocity method does not require the use of a reference transducer, it is a useful and often used calibration technique. The reciprocity technique was first introduced by MacLean [113] and applied to underwater sound by Ebaugh and Meuser [114]. The self-reciprocity technique was later described by Simmons and Urick [115]. The reciprocity method is based off the electroacoustic reciprocity principle which relates current and open-circuit voltage on the electrical side to the

diaphragm velocity and impressed force on the acoustical side of an electroacoustic device:

$$\frac{|E|}{|v|} = \frac{|F|}{|I|} \quad (5.4)$$

Where E is the electric voltage, I is the electric current, v is the velocity on the diaphragm and F is the force of the diaphragm. This expression can be used to calibrate a transducer by relating velocity v to the pressure produced at a distance when the transducer is acting as a transmitter and by relating the force F to the incident sound wave when the transducer is acting as a receiver. The relationship depends on whether the transducer generates spherical, cylindrical, or plane waves [112].

For a cylindrical transducer, the acoustic pressure at distance r can be shown to be [112]:

$$P_r = \pi \rho a v \left(\frac{cf}{r} \right)^{1/2} \quad (5.5)$$

where ρ is the density of water, a is the radius of the cylinder, v is the surface velocity of the cylinder, c is the velocity of sound and f is the carrier frequency. If the transducer acts as a receiver, the force exerted upon it by an incident sound field of pressure P_i will be [112] :

$$F = AP_i = 2\pi a L P_i \quad (5.6)$$

where A is the face area of the cylinder and L is the length of the cylinder. Inserting into the reciprocity relationship 5.4 we obtain [112]:

$$\frac{E}{P_i 2\pi a L} = \frac{P_r}{I} \left(\frac{r}{cf} \right)^{1/2} \frac{1}{\pi \rho a} \quad (5.7)$$

Writing equation 5.7 as the relationship between the receiving response $M = E/P_i$ and the transmitting response $S = P_r/I$ we obtain [112]:

$$J_c = \frac{M}{S} = \frac{2L}{\rho c} \left(\frac{cr}{f} \right)^{1/2} \quad (5.8)$$

The ratio J_c was first derived by Bobber and Sabin [116] and is called the cylindrical wave reciprocity parameter. It can be empirically measured.

Using self-reciprocity, $P_i = P_r$ assuming the pressure field incident on the receiver is the same as that generated by the transmitter. The receiving response may then be measured as [115]:

$$M = \left(\frac{J_c E_r}{I} \right)^{1/2} = \left(J_c \frac{E_r Z}{E_t} \right)^{1/2} \quad (5.9)$$

where the current I equals the known transmitted voltage, E_t , divided by the measured impedance Z , and E_r is the measured received voltage.

5.4 Experimental Measurements

Due to its simplicity, we made use of the comparison method to calibrate the homemade transducers. We suspended both the homemade transducer and reference transducer, a spherical ITC 1042 [118], 0.18 meters apart in the middle of a 3 meter deep, 2 meter wide cylindrical test tank filled with salt water. Burst signals of duration 2ms, across frequencies in 1kHz increments were sent from the reference transducer to the homemade transducer and vice versa. Signals were sent and collected via LabView. Figures 5.2 and 5.3 show the TVR and RVR of the ITC transducer, a Marport transducer [117] (a directional commercial transducer), and the homemade transducer (T1). As expected, the gain of the Marport (directional) transducer is higher than that of transducer T1 as it can concentrate its energy in one direction. The gain of transducer T1 is higher than that of the ITC transducer due to the larger physical size of its ceramic.

Adding the TVR and RVR gives a quantity known as the ‘Figure of Merit’ which gives an indication of the transducer’s best operating frequencies when acting as both a transmitter and receiver. Figure 5.4 shows the Figure of Merit calculated from the Lab View data indicating an operating frequency range around 40kHz for transducer T1. The peaks and valleys of the Figure of Merit can be attributed to constructive and destructive interference caused by reflections off the sides of the small calibration tank.

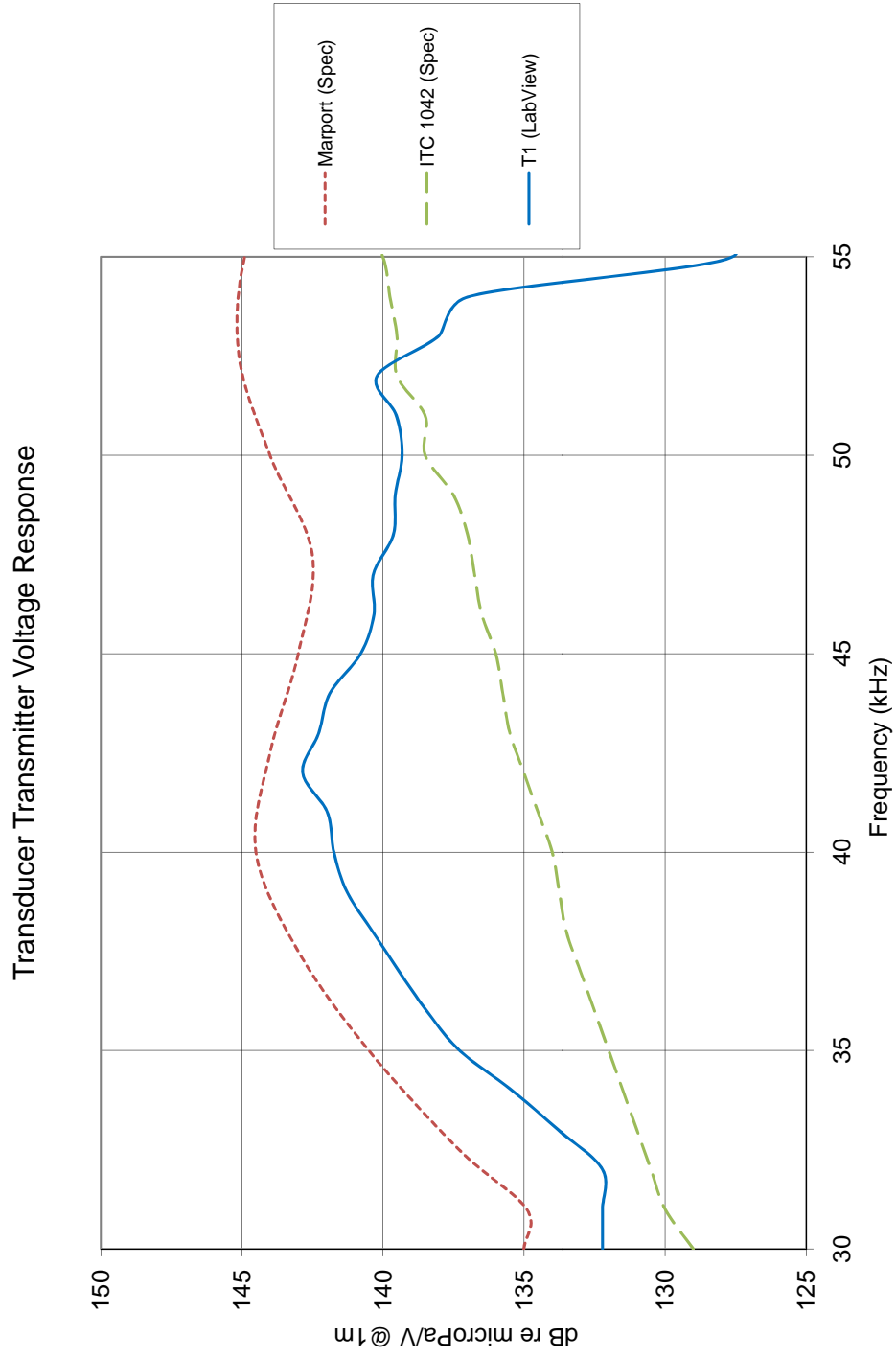


Figure 5.2: Transducer Transmitter Voltage Response

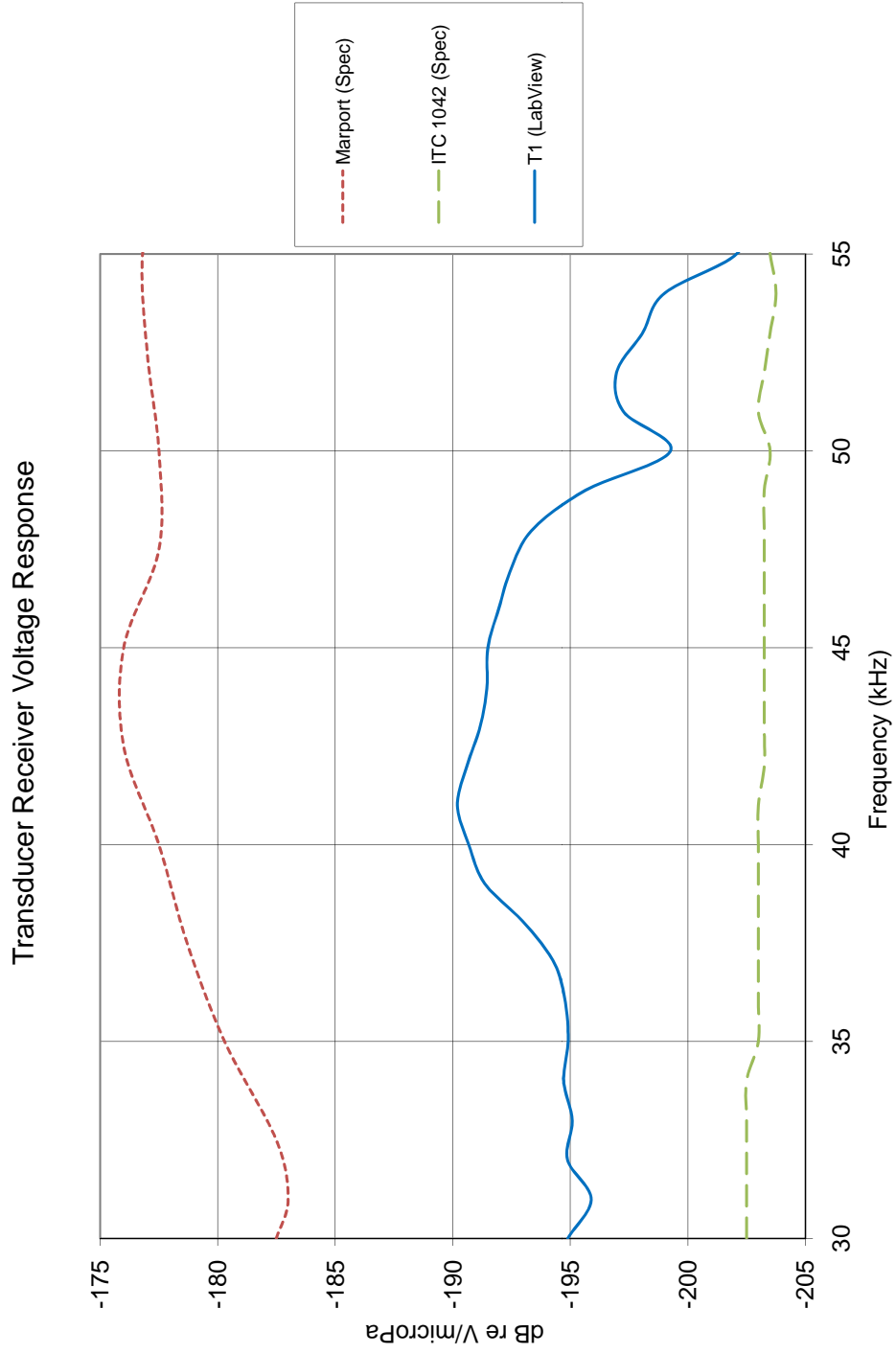


Figure 5.3: Transducer Receiver Voltage Response

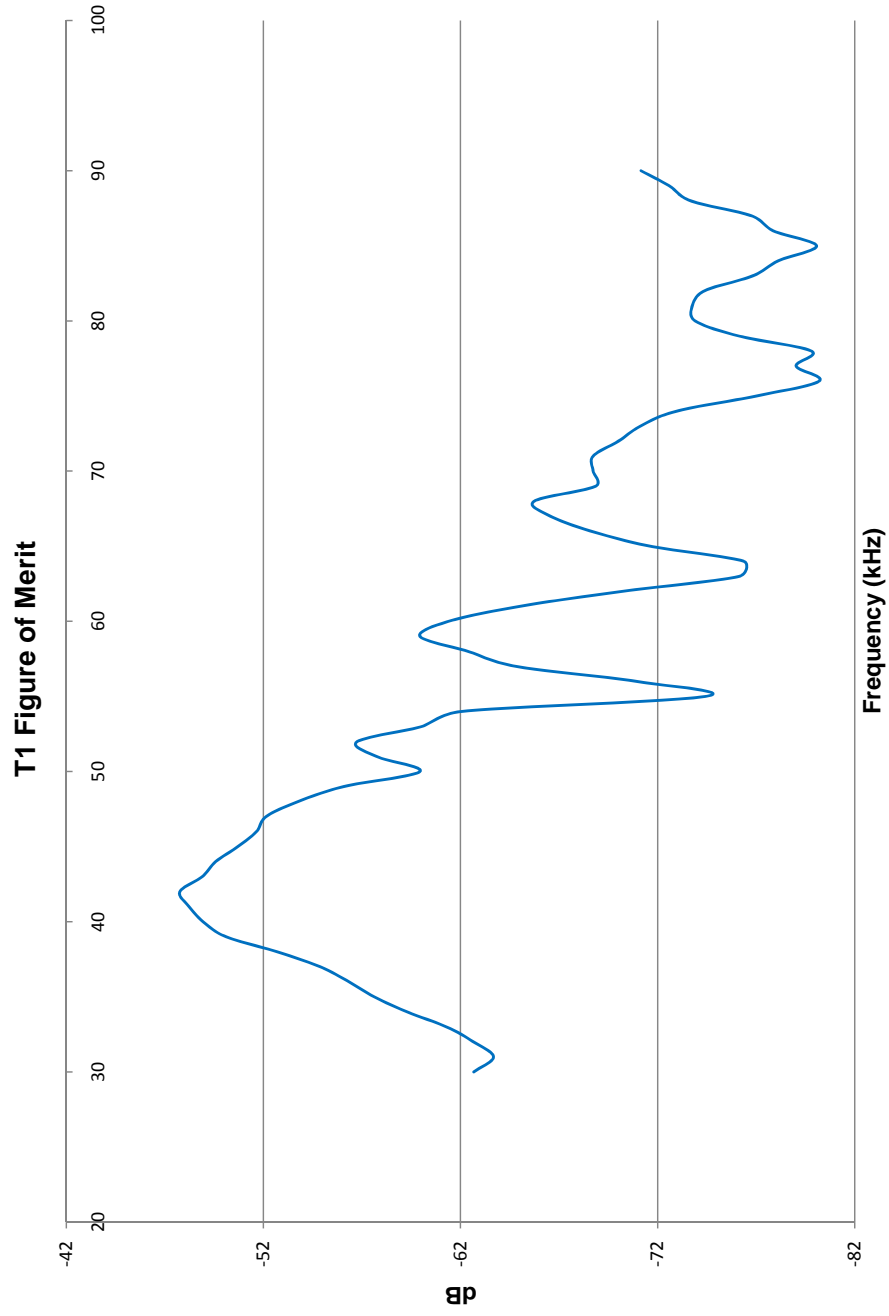


Figure 5.4: Transducer Figure of Merit

5.5 Summary

This chapter described the design of our low-cost transducer, its ceramic type and geometry, its potting compound and procedure, and its electro-mechanical properties. The low-cost transducer costs \sim \$40, is omni-directional in the horizontal plane, operates in a narrow frequency band around 40kHz, and has a source level of about 140 dB re 1uPa @ 1m. The next chapter describes the UCSD-Modem's analog transceiver which was designed to operate in the transducer's operating frequency range.

The text of Chapter 5, is currently being prepared for submission for publication of the material. The dissertation author was a co-primary researcher and author (with Kenneth Domond). Ryan Kastner and Don Kimball directed and supervised the research which forms the basis for Chapter 5.

Chapter 6

Analog Transceiver Design

The analog transceiver consists of a power amplifier, a power management circuit, an impedance matching circuit, and a pre-amplifier (Figure 6.1). The power amplifier is responsible for amplifying the modulated signal from the digital hardware platform. It sends the signal to the power management circuit which further amplifies the signal to a power level that matches the actual distance between the transmitter and receiver. The power management circuit then sends the amplified signal to the impedance matching circuit, which is matched to the transducer's resonance frequency, so that the signal may be transmitted efficiently to the water. The pre-amplifier amplifies the signal that is detected by the transducer so that the digital hardware platform can effectively demodulate the signal and analyze the received data. This chapter describes the design of the power amplifier, power management circuit, impedance matching circuit, and pre-amplifier of the analog transceiver.

6.1 Power Amplifier Design

When designing the power amplifier we considered the following requirements:

- The amplifier should provide a linear, undistorted output over a relatively wide bandwidth (10 - 100kHz) to allow for use with a variety of underwater



Figure 6.1: **Analog Transceiver**

transducers

- The amplifier must be power efficient (especially for large output power) as a deployed modem must be powered from batteries

Power amplifiers are classified according to their circuit configurations and methods of operation into different classes such as A, B, AB, C, D, G and H. These classes range from entirely linear with low efficiency to entirely non-linear with high efficiency [119]. An amplifier is said to be linear if it preserves the details of the signal waveform, that is:

$$V_o(t) = AV_i(t) \quad (6.1)$$

The amplifier is said to be efficient if it can convert the majority of the dc power of the supply into the signal power delivered to the load. Efficiency, is defined as:

$$\text{efficiency} = \frac{\text{signal_power_delivered_to_load}}{\text{DC_power_supplied_to_output_circuit}} \quad (6.2)$$

To meet our design requirements, we wished to design a power amplifier that was both linear and efficient. We considered the characteristics of the most common amplifier classes (A, B, AB, and D). The following material was gathered from [120, 121, 122].

A Class A amplifier consists of a single transistor for its output stage conducting over the whole of the input cycle such that the output signal is an exact, scaled-up, replica of the input and thus completely linear. However, because the amplifier is continuously conducting, Class A amplifiers are not very efficient, having a theoretical maximum efficiency of 50% (with typical operation at 10-25% efficiency). A typical Class A input / output characteristic is shown in Figure 6.2.

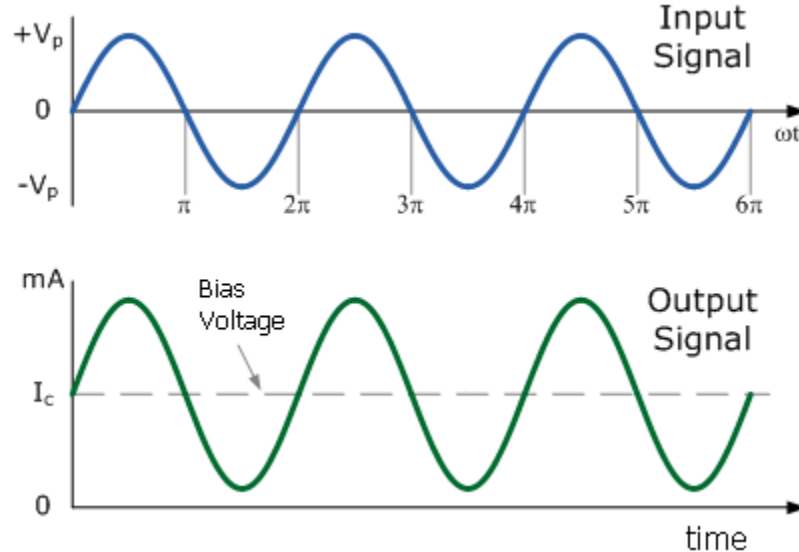


Figure 6.2: **Class A Amplifier Input/Output Characteristic**

Unlike a Class A amplifier, a Class B amplifier consists of two complimentary transistors to handle both halves of the waveform. Each amplifying device conducts for only half the sinusoidal cycle and neither device conducts when there is no input, thus increasing the efficiency of the amplifier. Class B amplifiers typically have an efficiency of about 50%, but have some issues with linearity at the crossover point, due to the time it takes to turn one transistor off and turn the other transistor on. A typical Class B input / output characteristic for one of its

transistors is shown in Figure 6.3.

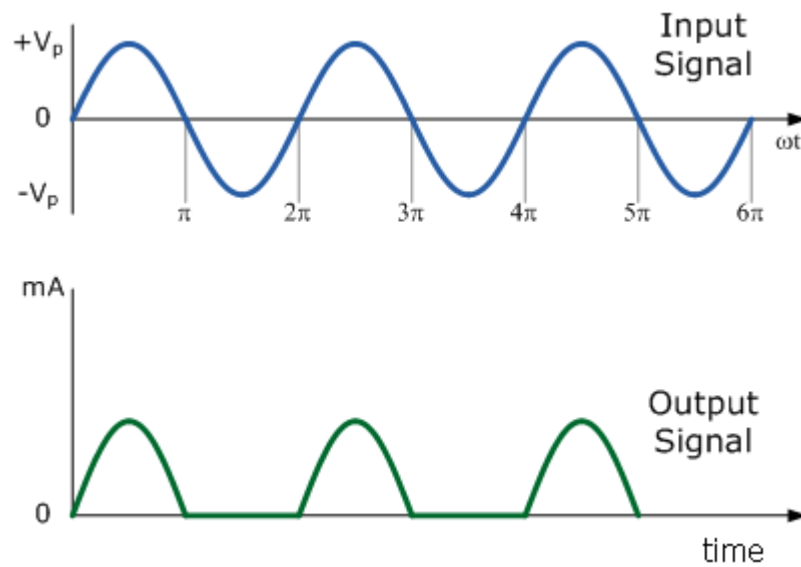


Figure 6.3: Class B Amplifier Input/Output Characteristic for one transistor

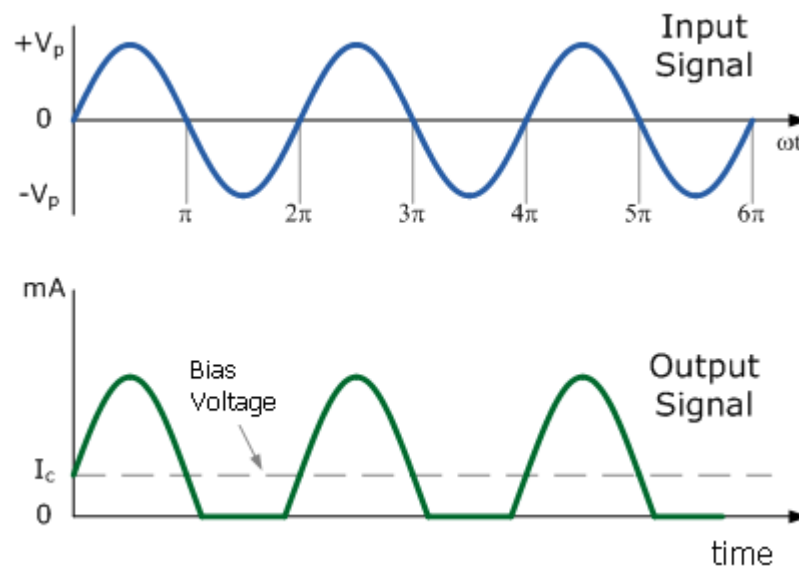


Figure 6.4: Class AB Amplifier Input/Output Characteristic for one transistor

The Class AB amplifier is a compromise between the Class A and Class B configurations and is currently one of the most common types of power amplifiers

in existence. Like a Class B amplifier, the Class AB amplifier consists of two complementary transistors, but unlike the Class B amplifier, both devices are allowed to conduct at the same time, but just a small amount near the crossover point. Thus each device conducts for more than half a cycle but less than a whole cycle, overcoming the inherent non-linearity of Class B designs without the inefficiencies of a Class A design. Efficiencies for Class AB amplifiers are typically 50% with a theoretical maximum of 72%. A typical Class AB input / output characteristic for one of its transistors is shown in Figure 6.4.

The Class D amplifier is a ‘switching amplifier.’ The basic Class D amplifier consists of a comparator, a switching stage (typically two MOSFET transistors) and a low pass filter. A block diagram of a basic Class D amplifier is shown in Figure 6.5. The input signal is compared to a sawtooth waveform (of higher frequency than the highest frequency component of the input signal) and the output signal of the comparator goes high when the input signal is higher than the sawtooth waveform. The output of the comparator drives two transistors which operate as switches creating a pulse width modulated waveform. The switches are either fully on or fully off, significantly reducing the power losses in the output devices. The low pass filter removes inaccurate spectral components resulting in an output signal that is an amplified replica of the input (although not completely linear). Efficiencies of 90-95% are possible.

As we desired a highly linear amplifier (in the range of 10-100kHz) with high power efficiency (especially for large power outputs) we designed a unique architecture that consists of a Class AB and a Class D amplifier working in parallel (Figure 6.6).

The primary amplifier is a highly linear Class AB amplifier that provides a highly linear voltage gain of 27 across input voltages and frequencies (see Figure 6.7). The output of the Class AB amplifier is connected to current sense circuitry that in turn controls the secondary amplifier, which is a Class D switching amplifier. The Class D amplifier is inherently nonlinear, but when working in tandem with the Class A/B amplifier, it produces a linear output for input voltages greater than 500 mVpp across frequencies (see Figure 6.8). The Class D amplifier provides high

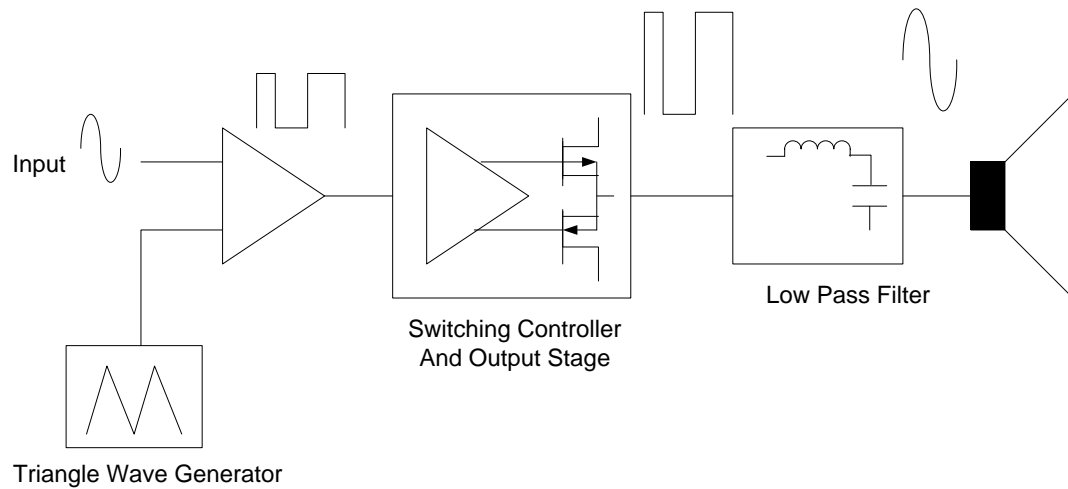


Figure 6.5: **Block diagram of a basic switching or PWM (Class-D) amplifier**

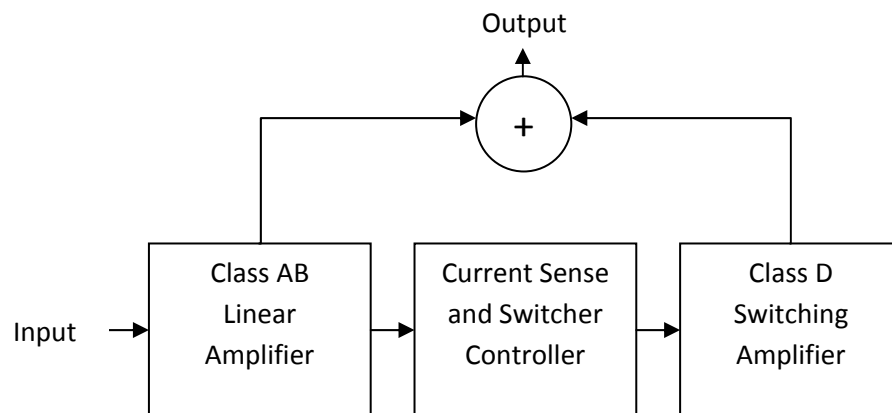


Figure 6.6: **Block diagram of the power amplifier design making use of a class AB and class D amplifier to achieve linearity and efficiency**

power efficiency to the complete amplifier for large power outputs (where the load resistance is below 15 ohms) but must be turned off for lower power outputs where its efficiency drops below that of the Class A/B amplifier alone.

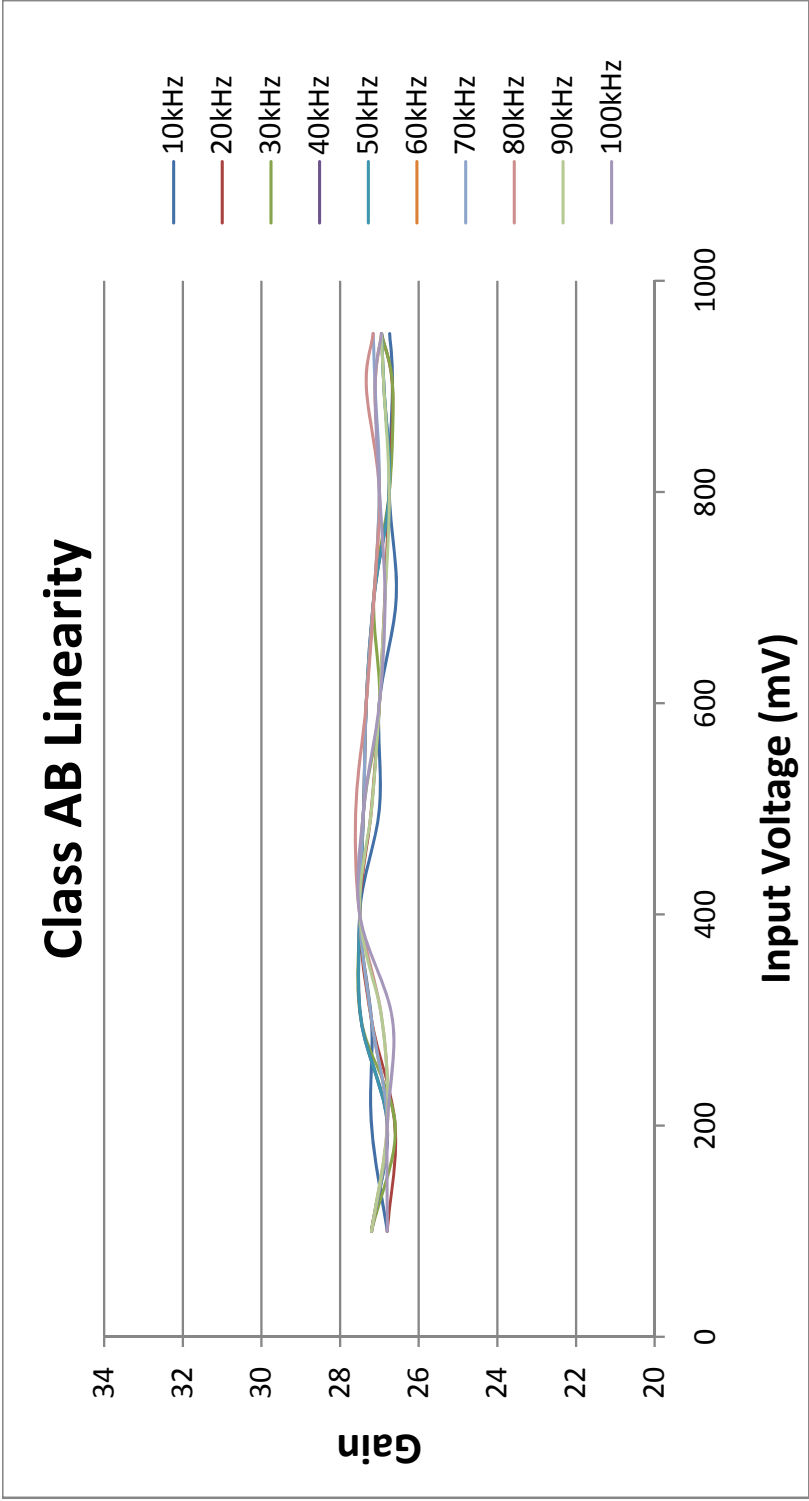


Figure 6.7: Class AB Power Amplifier Linearity

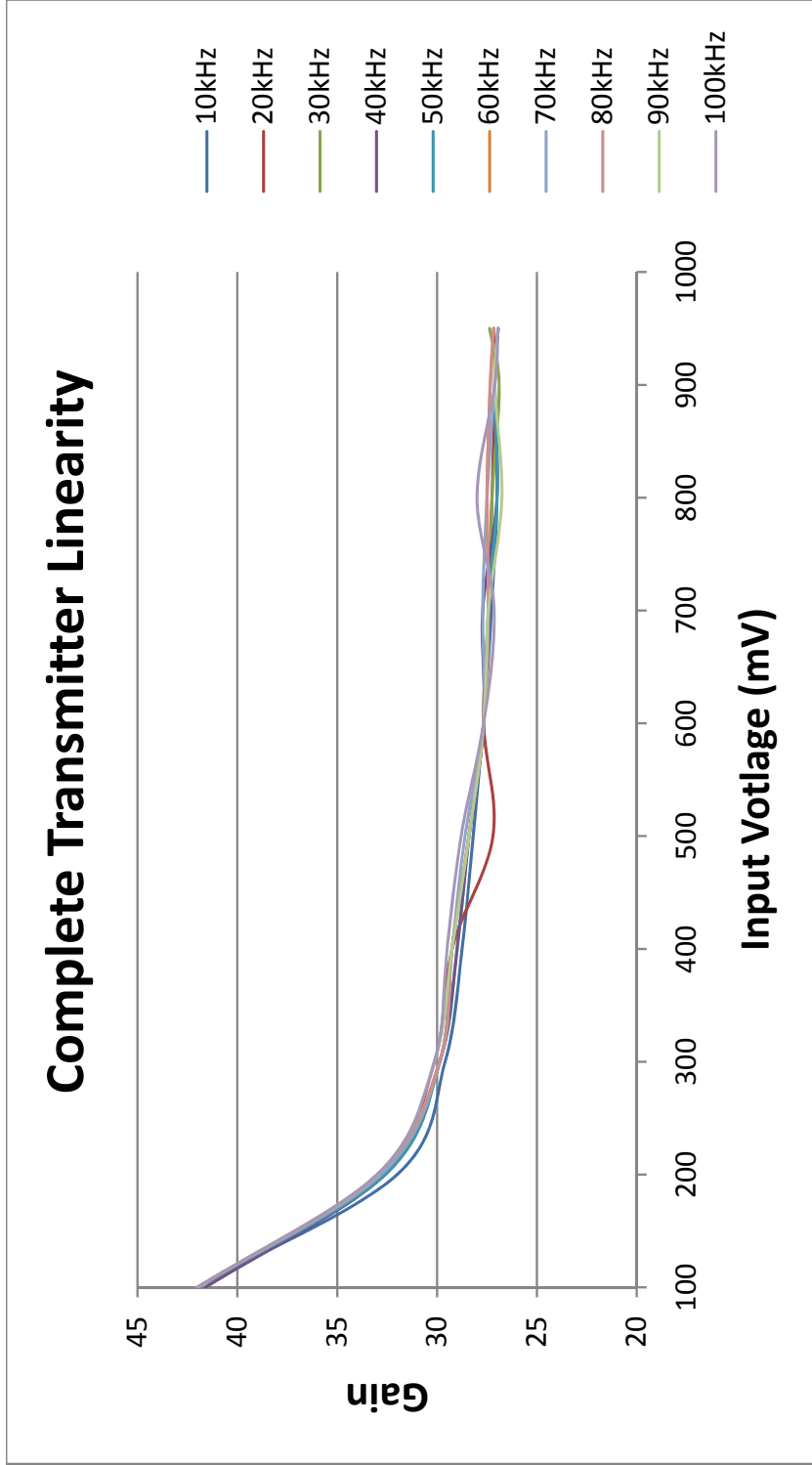


Figure 6.8: Complete Power Amplifier Linearity

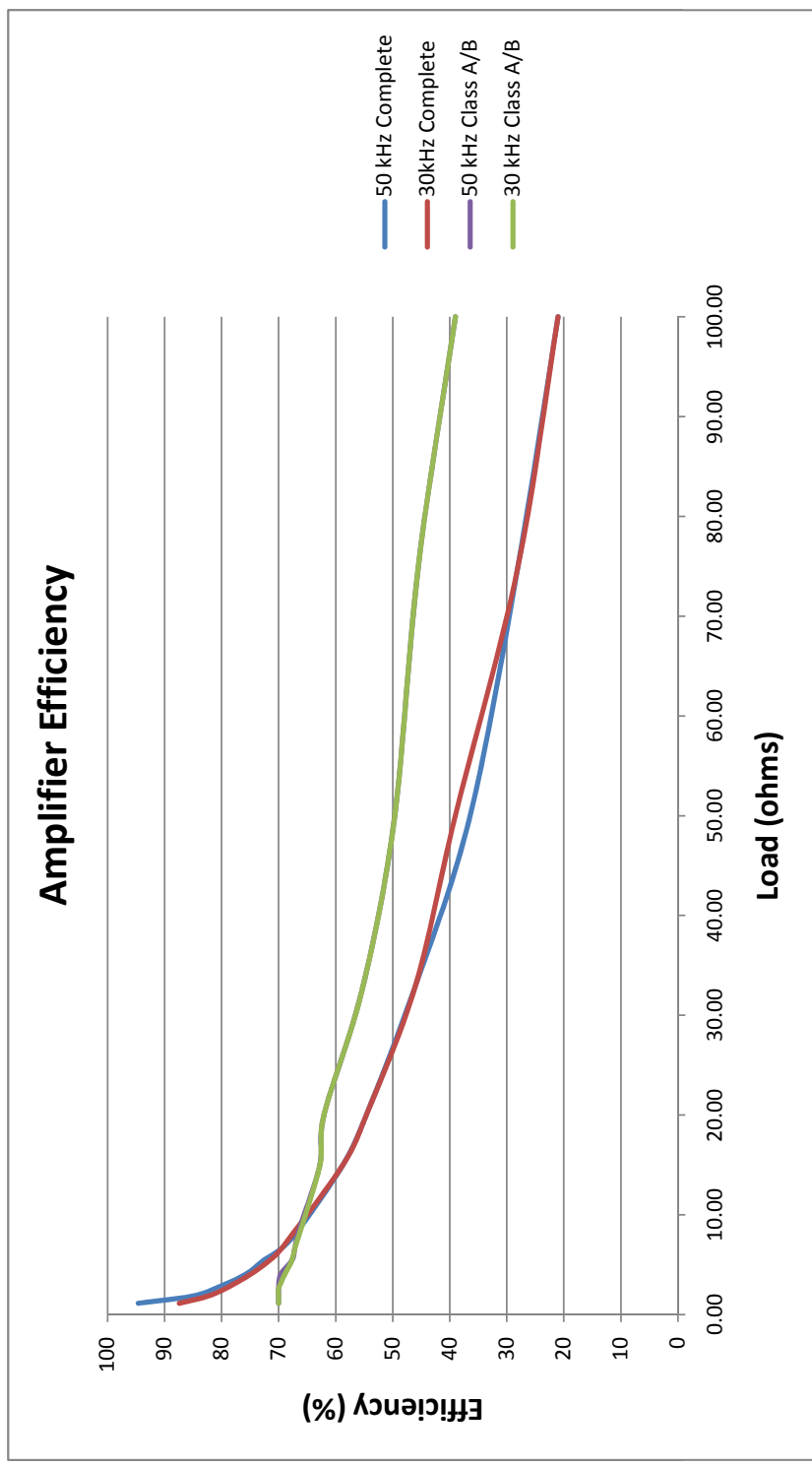


Figure 6.9: Power Amplifier Power Efficiency

6.2 Power Management Circuit

The power management circuit is provided to adjust the output power of the transceiver in real-time to match the actual distance between transmitter and receiver. The power management circuit takes the output of the power amplifier and further amplifies it to one of five power levels depending on how far the modem must transmit the signal. This is enabled through five different outputs at the taps on the secondary coil of the transformer (Figure 6.10). The number of windings on the secondary coil (N) divides the effective resistance of the load by N^2 thus increasing the power. The different transformer taps are connected to the impedance matching network (explained in the next section) by a series of relays. The relays are single pole, single throw and are controlled by a 5V, 40mA signal. Each of the relay outputs are connected to one another but none are open unless the relay is energized.

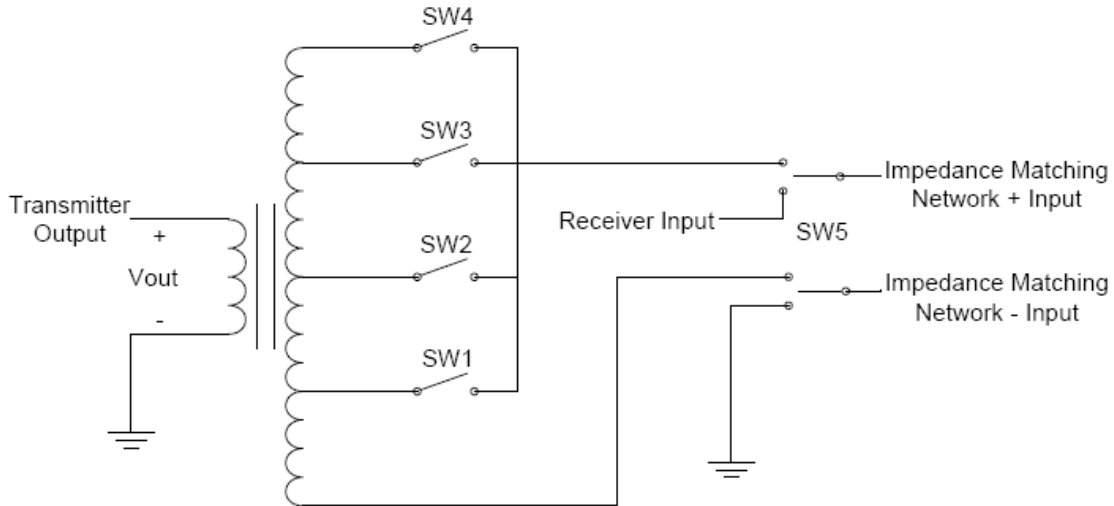


Figure 6.10: **Power Management Circuit**

The number of windings (N), voltage output, and transceiver power consumption of each power setting when connected to the homemade transducer and given a 1V_{pp} input is given in table 6.1. Note that because the output load of the transducer is high (750 ohms divided by the appropriate N^2), only the class A/B amplifier is used in this current configuration of the transceiver.

Table 6.1: Power Management Characteristics

Power Level	No. Windings (N)	V_O (Vpp)	$P_{consumed}$ (W)
0	0	23	1.2
1	2.5	62	1.8
2	5	122	2.7
3	7.5	180	4.5
4	10	230	6.9

6.3 Impedance Matching Circuit

Impedance matching is the practice of setting the input impedance of an electrical load equal to the output impedance of the signal source to which it is connected in order to maximize power transfer. Thus the output impedance of the power amplifier must match the input impedance of the transducer. Matching is obtained when $Z_S = Z_L^*$ (where Z_S is the impedance of the source (or power amplifier) and Z_L^* is the complex conjugate of the impedance of the load (or transducer)).

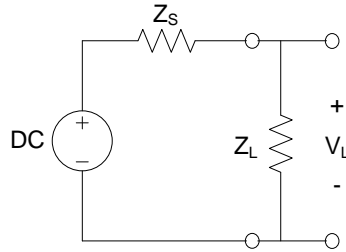


Figure 6.11: **Maximum Power Transfer is achieved when Z_S matches Z_L**

The transducer's impedance varies across frequencies as it is an active element that can be modeled with the following RLC circuit shown in Figure 6.12 [103]. The static capacitance is the only physical component and is a direct consequence of the type of piezoelectric material and transducer geometry. It can be measured by an RLC meter and for the homemade transducer equals approximately 6.0nF across frequencies.

To experimentally determine the transducer's electrical impedance, we mea-

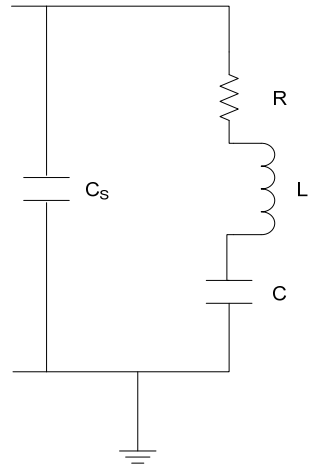
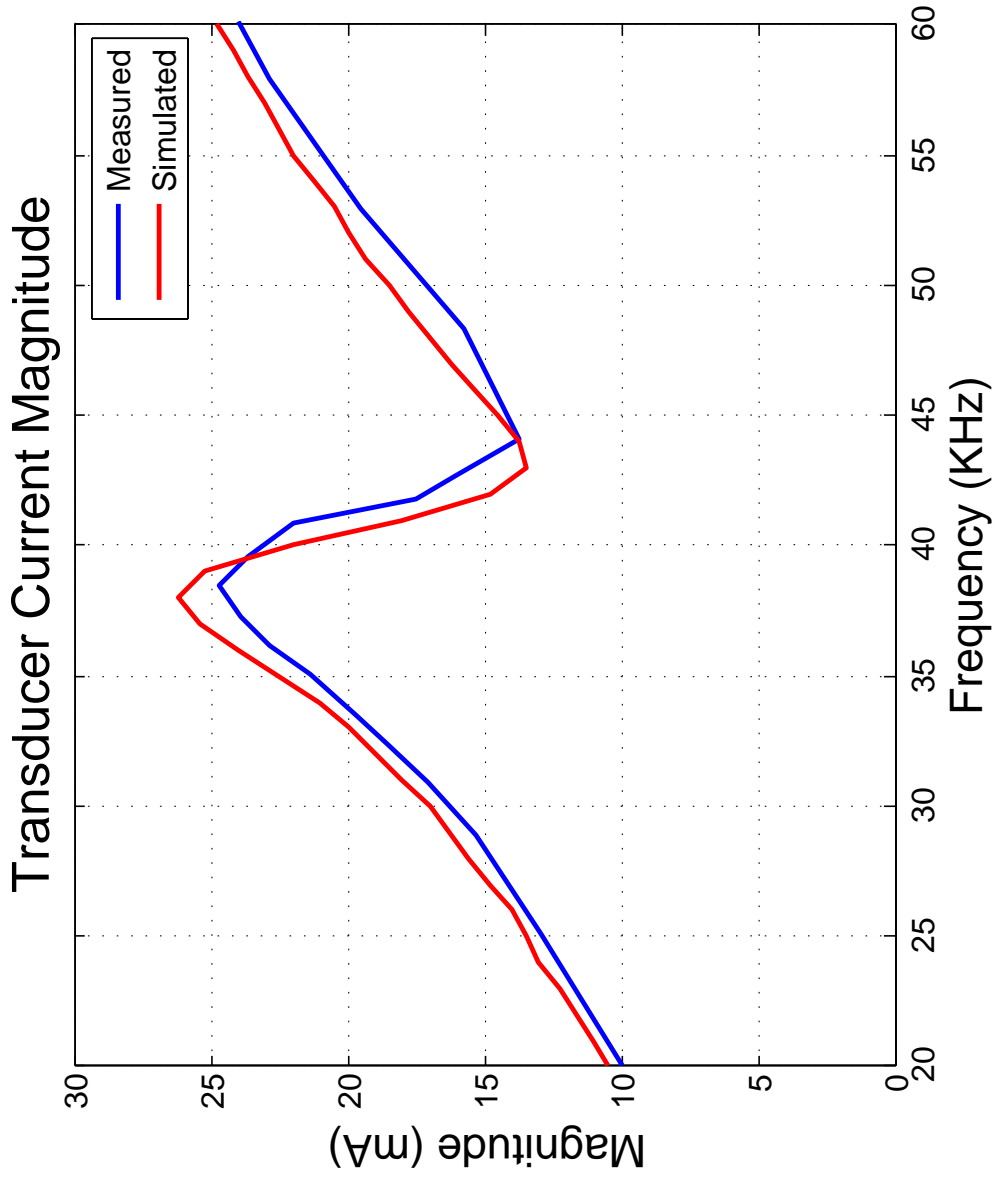
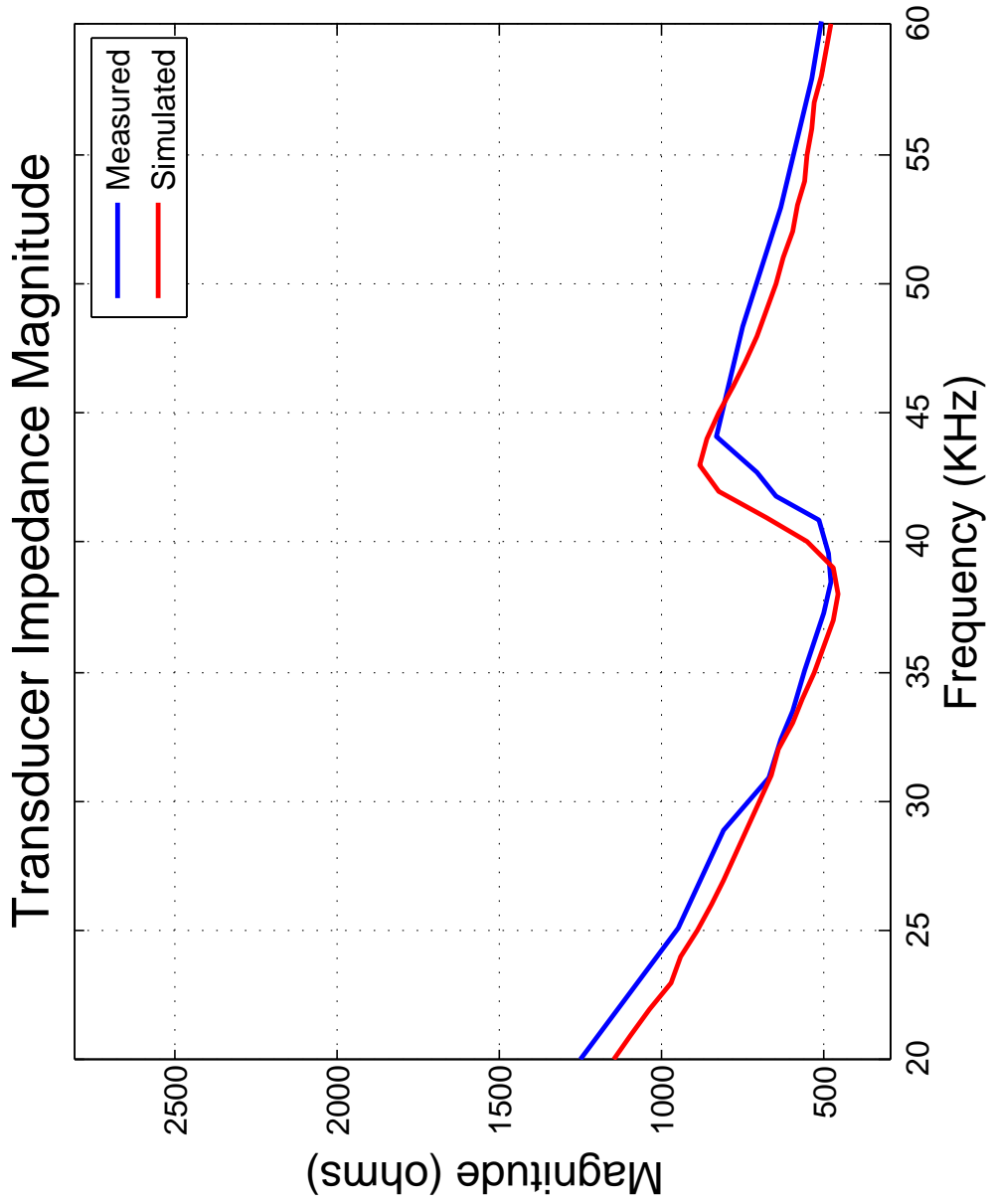
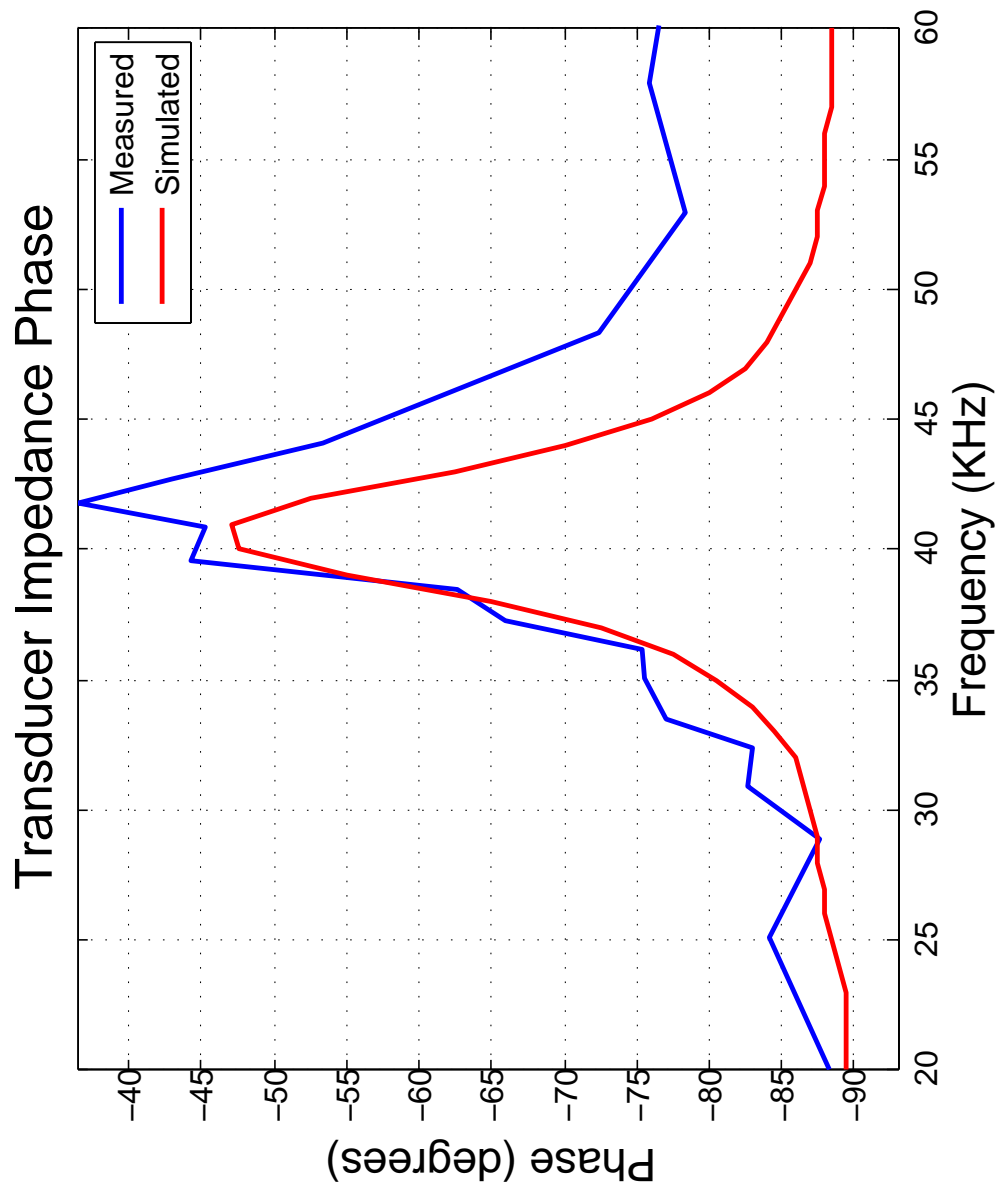


Figure 6.12: **Electrical Equivalent Circuit Model for a Transducer**

sured the voltage, current, and phase difference between the voltage and current across frequencies. We then modeled the circuit in Figure 6.12 in PSpice [92] with values of the RLC circuit selected to match the characteristics of the measured values. Figures 6.13, 6.14, and 6.15 show the measured and simulated current, impedance magnitude, and phase of transducer. The selected values for the RLC circuit were 750 ohms, 2.3mH, and 700pF respectively. Notice the agreement between the measured and simulated values indicating the equivalent circuit is a good model for the transducer's electrical behavior. Notice that the current reaches a relative maximum and the impedance magnitude reaches a relative minimum around 40kHz, the operating frequency of the transducer as described in Chapter 5. The impedance phase is almost always near -90 degrees (suggesting the transducer element is mostly capacitive), but decreases to about -45 degrees around 40kHz.







As the transducer is mostly capacitive, the impedance matching circuit consists of a single 2.5 mH inductor. This inductor value was experimentally chosen to make the circuit look mostly resistive (0 phase) around the operating frequency (40 kHz).

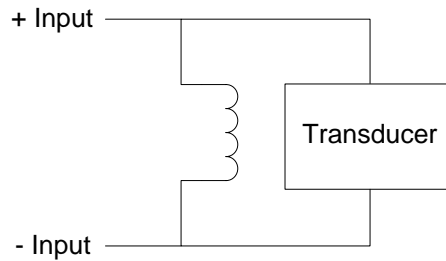
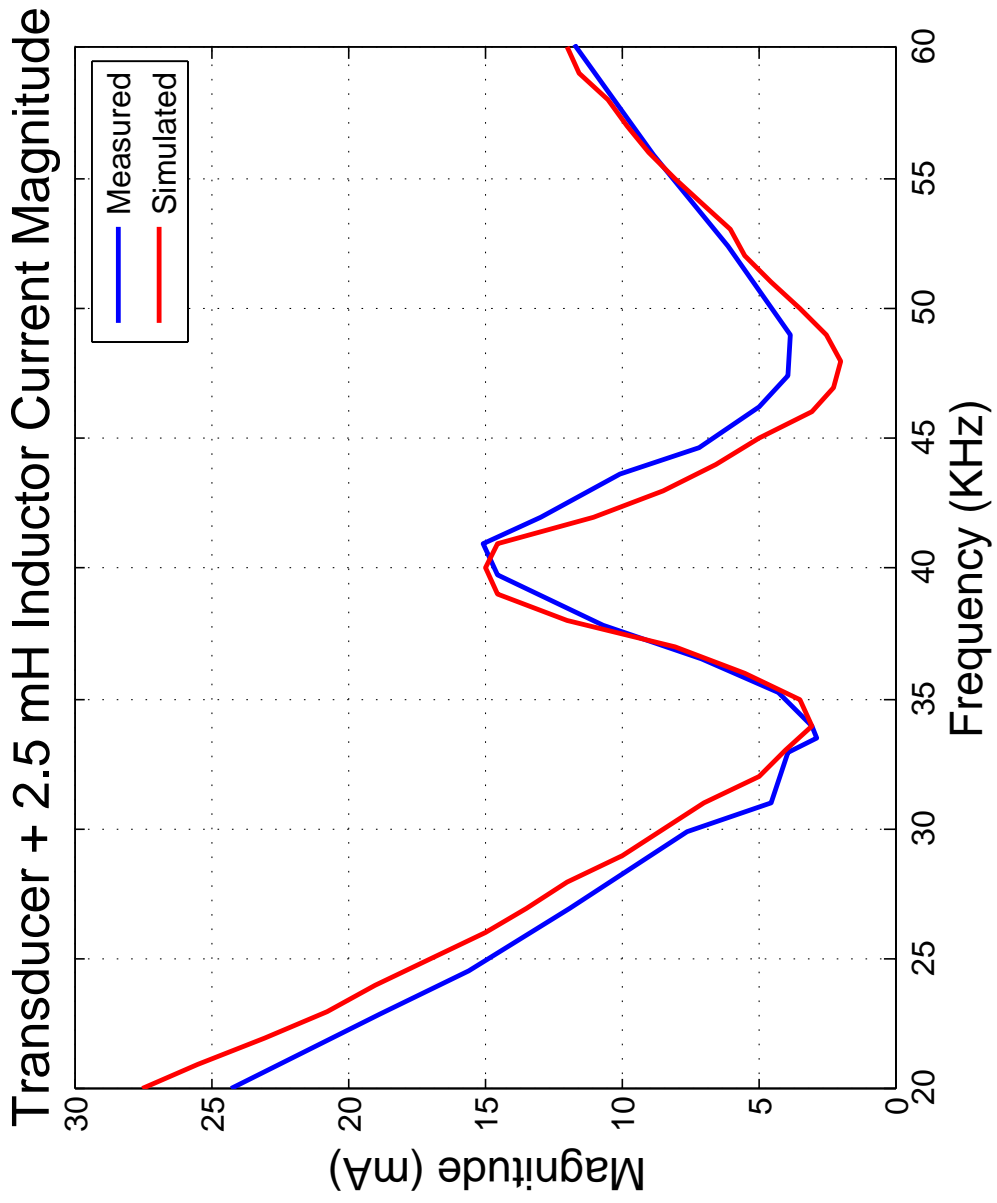
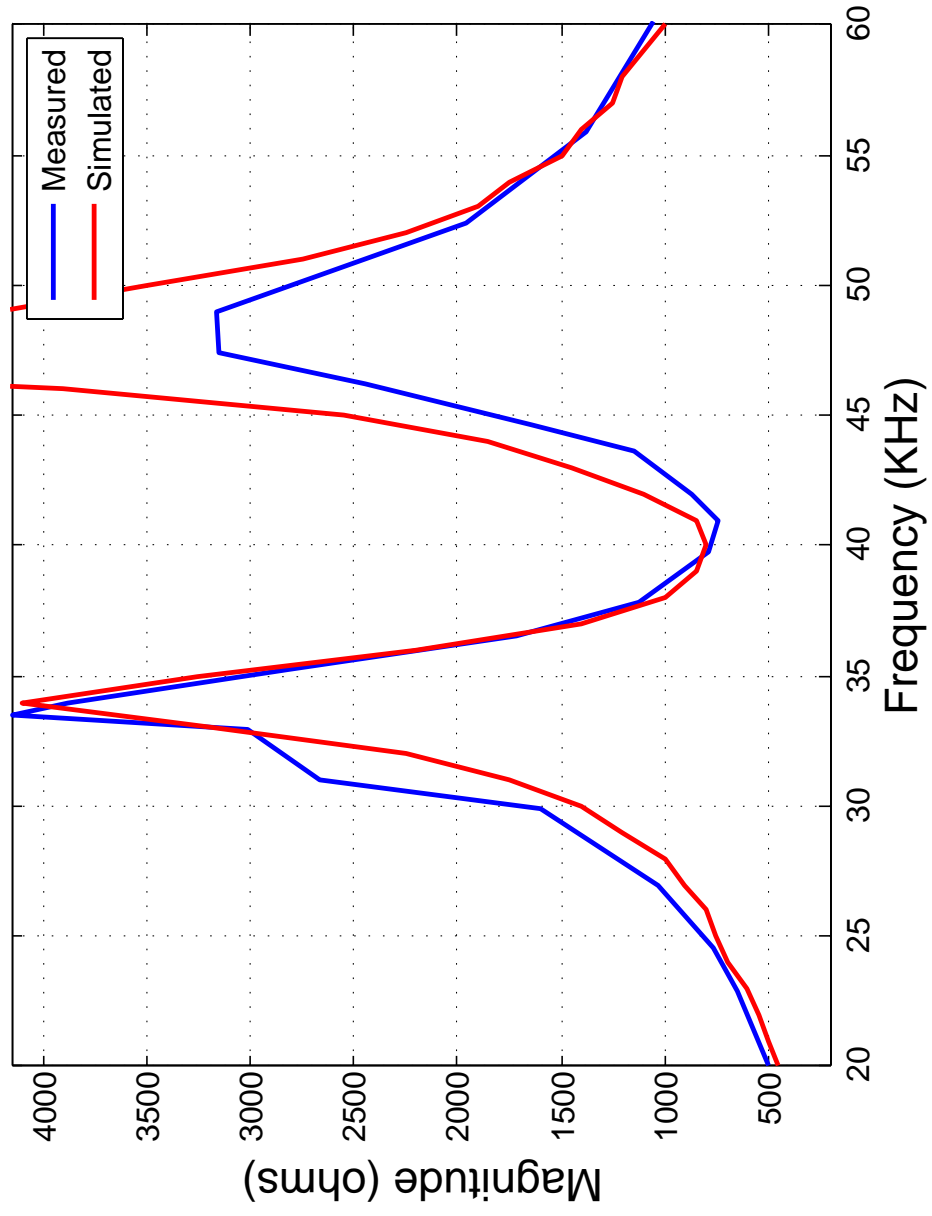


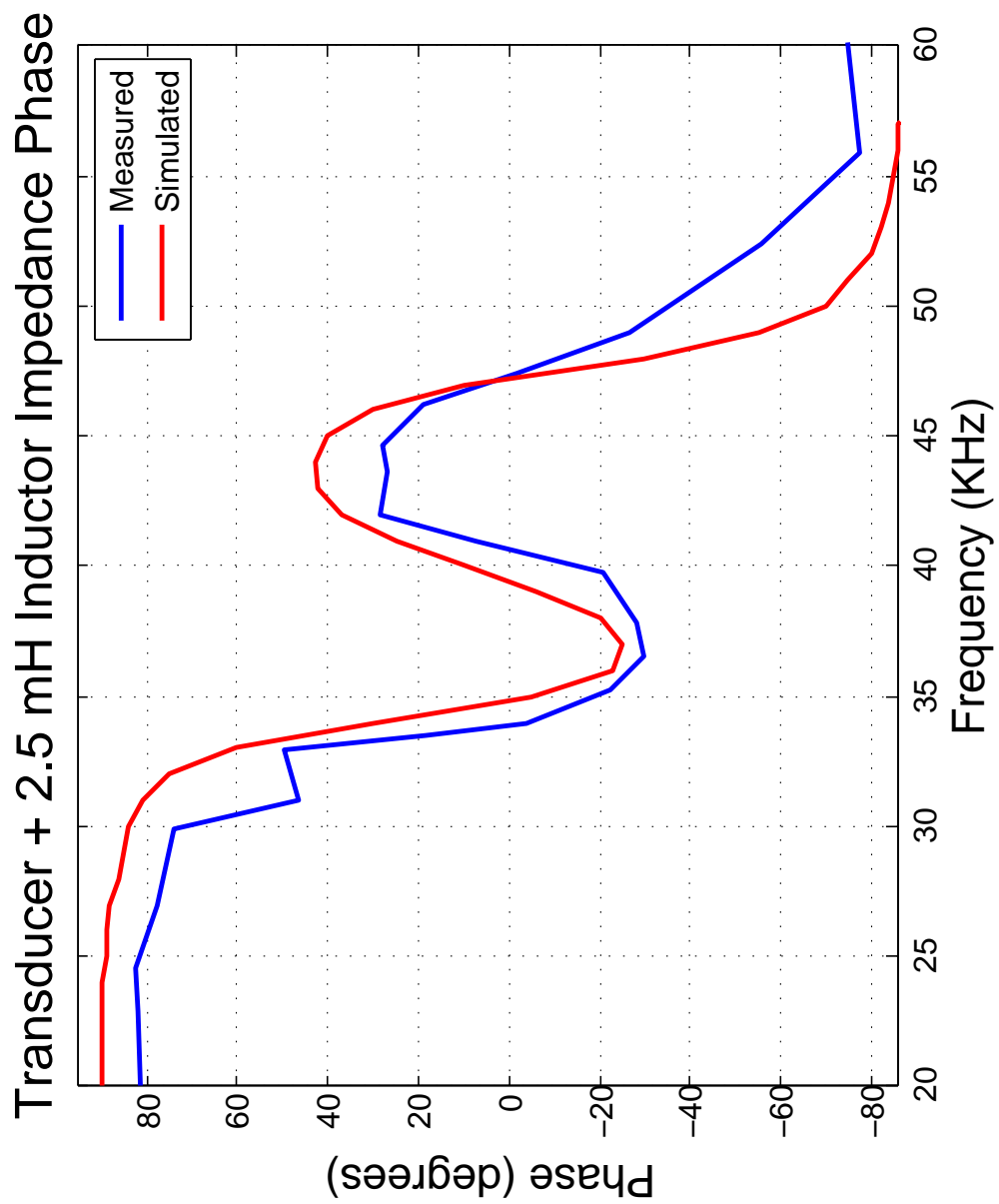
Figure 6.16: **Transducer Impedance Matching Circuit**

With the circuit shown in Figure 6.16, Figures 6.17, 6.18, and 6.19 show the new measured and simulated current, impedance magnitude, and phase of the transducer when combined with the impedance matching inductor. The figures still show a relative minimum impedance and relative maximum current around 40kHz. Figure 6.19 shows the circuit is mostly resistive (close to 0 degree phase) between 35kHz and 45kHz suggesting the circuit could be fairly power efficient in this range.



Transducer + 2.5 mH Inductor Impedance Magnitude





Although the power coupled into the transducer cannot directly be measured, we can use the equivalent circuit in PSpice to estimate the power delivered to the load. Figure 6.20 shows the majority of the amplifier's output power is coupled into the transducer between 35kHz and 45kHz as expected from Figure 6.19.

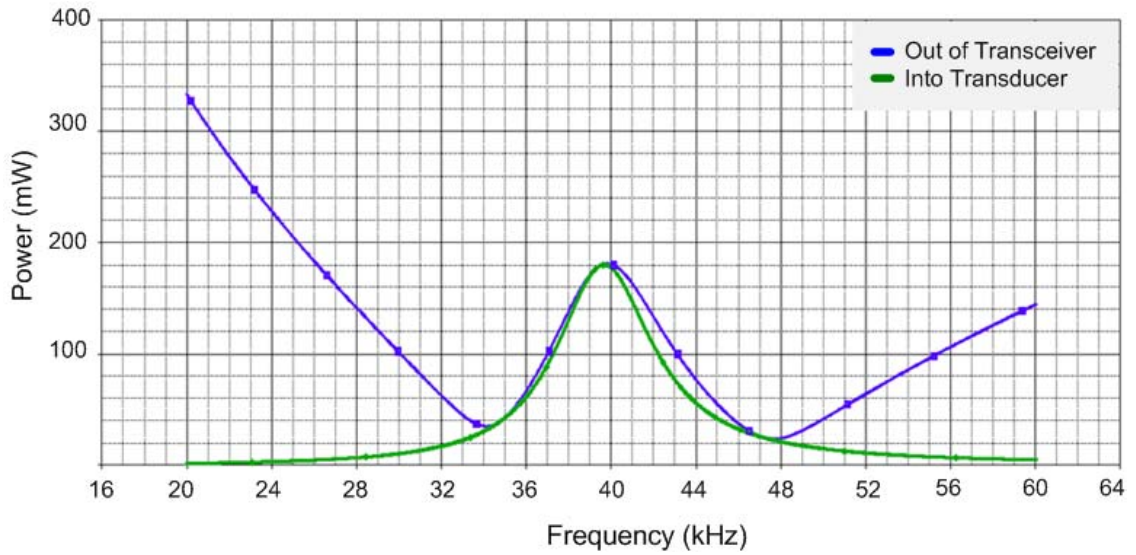


Figure 6.20: **Estimated Power Coupled into the Transducer**

6.4 Pre-Amplifier Design

When designing the pre-amplifier for the receiver, we considered the following requirements:

- The pre-amplifier must amplify signals around the transducer's resonance frequency (40kHz) and filter out all other frequencies
- The pre-amplifier must provide high gain to pick up signals as small as a couple hundred microVolts
- The design must be easily modifiable to accommodate different transducers with different resonance frequencies and bandwidths

To meet the above design requirements of a highly sensitive, high gain, narrow band receiver, the architecture consists of two main components: 1. a 40dB per decade rolloff high-pass filter and 2. an 80 dB per decade rolloff band-pass filter as shown in Figure 6.21.

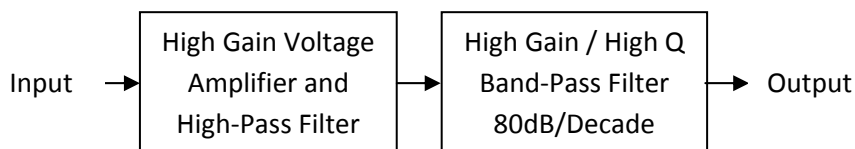


Figure 6.21: **Receiver Block Diagram**

As underwater noise is concentrated in low frequencies (see Figure 3.10) the first stage (a high pass filter) cancels out a majority of unwanted noise. The high pass filter consists of two cascaded filters, each with a 20dB per decade rolloff. Each filter has a gain of 10 and a cutoff frequency of 16kHz thus giving a total gain of 100 (40dB). The second stage is a bandpass filter used to further amplify signals in the transducer's operating band. It consists of four cascaded biquad filters, each with a 20dB per decade rolloff. The current configuration has the center frequency of the first and third filters set to 40kHz and the center frequency of the second and fourth filters set to 41kHz to obtain a flatter frequency response in the pass band. Thus the combined pre-amplifier provides an ~ 80 dB gain around 40Khz while attenuating low frequencies at a rate of 120dB per decade and high frequencies at a rate of 80dB per decade (Figure 6.22). The pre-amplifier's gain, cut-off and center frequencies can be easily modified by replacing a few standard resistor and capacitor components.

The current receiver configuration consumes about 240 mW when in standby mode and less about 275 mW when fully engaged.

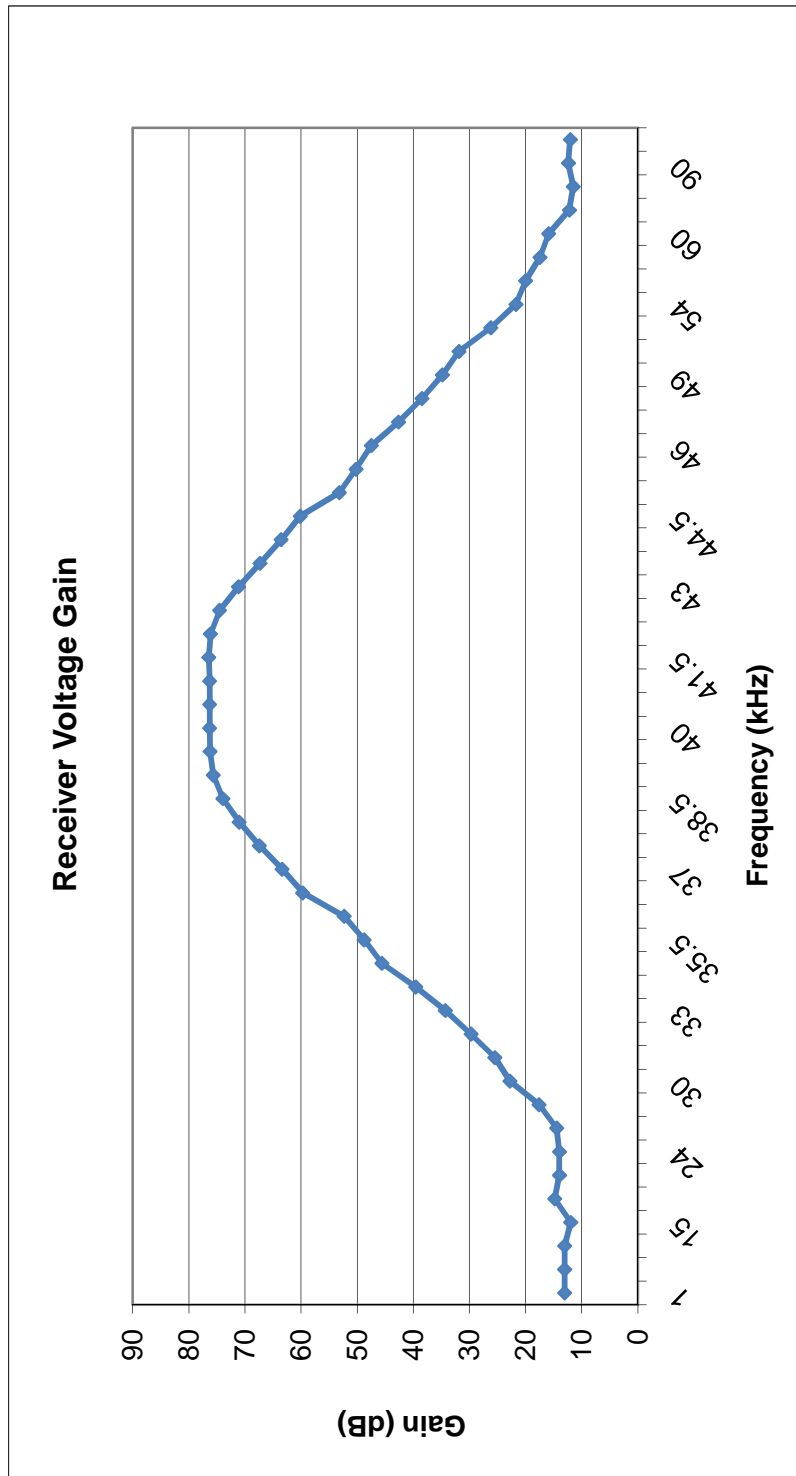


Figure 6.22: Overall Receiver Gain

6.5 Summary

This chapter described the full design of the analog transceiver including the power amplifier, power management circuit, impedance matching circuit, and pre-amplifier. The power amplifier is linear in the 10-100kHz band for inputs greater than 500 mV_{pp} and up to 95% efficient for high power outputs. The impedance matching circuit makes the transducer look resistive between 35-45kHz coupling the majority of the amplifier's output power to the transducer in that frequency band. The pre-amplifier provides a flat, high gain for frequencies 38-42kHz matching the operating frequency of the transducer and allowing for reception of a signal as low as 200 microvolts. The power management circuit provides five different output power levels that consume 1.2, 1.8, 2.7, 4.5, and 6.9 Watts respectively allowing the modem to adjust the output power in real-time to match it to the actual distance between transmitter and receiver. All components can be easily modified by replacing a few standard components.

The next chapter describes the design of the digital transceiver.

Chapter 7

Digital Design

This chapter describes the digital design of the UCSDModem. We begin with a discussion on different modulation schemes, describing the reason for the selection of the use of frequency shift keying (FSK). We then discuss various digital hardware platforms and the selection of a field programmable gate array (FPGA) for our design. These discussions are followed by a thorough description of the FPGA implementation of the FSK digital transceiver, including the modulator, digital down converter, symbol synchronizer, demodulator, clock structure, and HW/SW Co-design controller. The chapter concludes by presenting the resource requirements of the complete digital design.

7.1 Modulation Schemes

As described in Chapter 4, various modulation schemes have been implemented in existing commercial and research modems. These schemes all attempt to combat the performance limitations induced by the underwater acoustic channel while at the same time improving the bandwidth efficiency and bit rate as much as possible. This section briefly describes the characteristics of some of these schemes and reasons for our selection of the use of frequency shift keying for our modem design.

Frequency Shift Keying: Frequency shift keying is a simple modulation scheme that has been widely used in underwater communications over the past two

decades [75, 67]. In M-ary FSK, the data are transmitted by shifting the frequency of a continuous carrier to one of M discrete frequencies. The simplistic receiver typically compares the energy at different frequencies to infer what data have been sent (Figure 7.1). Using only non-coherent energy detection at the receiver, this scheme bypasses the need for phase tracking which is a very difficult task because of Doppler spread in the underwater channel. [123] To combat intersymbol interference caused by multipath and frequency spreading, guard intervals are typically inserted between successive symbol transmissions for channel clearing [42] or symbols with durations longer than the multipath spread are used. As a result, the data rate of FSK is very low. Frequency hopped FSK improves the data rate as it does not need to wait for channel clearing but requires a larger bandwidth. The minimum theoretical bandwidth for a binary FSK scheme is 2X the bit rate (in Hz).

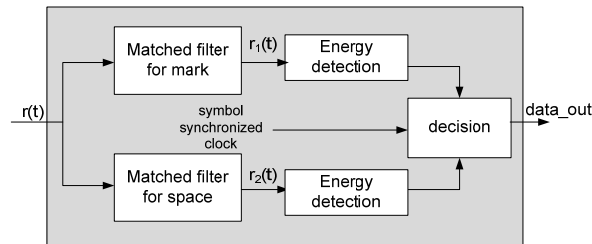


Figure 7.1: **Block diagram of classic matched filter FSK demodulator**

Phase Shift Keying: In M-ary phase shift keying (PSK), the data are transmitted by shifting the phase of a continuous carrier to one of M discrete phases. PSK signals require less transmitted power for a given probability of error than FSK systems (as shown in Figure 7.2) and require less bandwidth (the minimum theoretical bandwidth for a PSK scheme is bit rate (in Hz)) , but require more coherent detection, either by regenerating a local carrier in the receiver (as shown in Figure 7.3, or by using differential detection in which the previous bit is used as the phase reference for the current bit [124]. Although coherent detection could be used with FSK, the complexity required in the receiver for carrier regeneration justifies the better bit error rate (BER) performance of PSK. To combat intersymbol interference caused by multipath and frequency spreading, channel equalization

techniques are exploited. Decision feedback equalizers are used to track slowly varying channels and used to track faster varying channels when combined with a Phase locked loop [125]. Parameters in the equalizer may have to be fine-tuned to meet channel conditions. As coherent modulation does not have to wait for channel clearing, higher bit rates may be achieved at the expense of a more complex receiver.

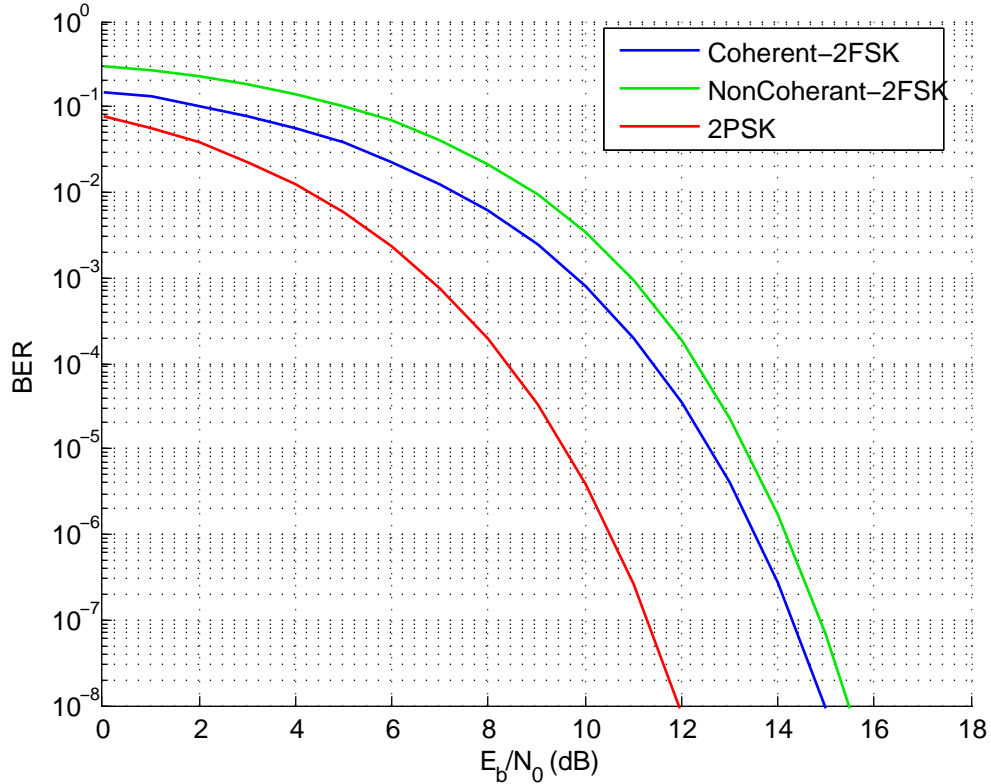


Figure 7.2: **Bit Error Rate of MFSK and MPSK for a given probability of error**

Direct Sequence Spread Spectrum: In DSSS modulation, the transmitted signal takes up more bandwidth than the information signal that is being modulated by multiplying each symbol with a spreading code and transmitting the resulting sequence at a rate allowed by the wider bandwidth. Due to the auto-correlation properties of the spreading sequence, intersymbol interference caused by the underwater channel is suppressed by the de-spreading operation at the receiver. Channel estimation and tracking are needed if phase-coherent modulation such as

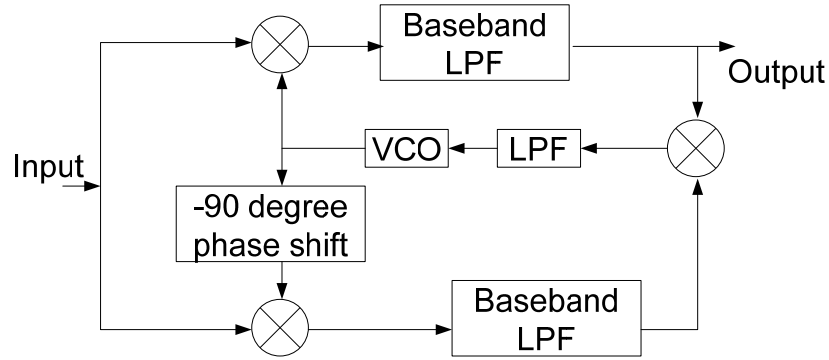


Figure 7.3: **Block diagram of a coherent PSK receiver**

phase-shift-keying (PSK) is used to map information bits to symbols before spreading [126]. For noncoherent DSSS, channel estimation and tracking may be avoided by using the information bits to select different spreading codes and comparing the amplitudes of the outputs from different matched filters (each matched to one spreading code) at the receiver [42]. Direct sequence spread spectrum techniques such as those seen in [80] require less transmitted power for a given probability of error than FSK.

Orthogonal Frequency Division Multiplexing: Orthogonal Frequency Division Multiplexing (OFDM) is often referred to as multicarrier modulation because it transmits signals over overlapping sub-carriers simultaneously. Sub-carriers (specific frequency bands) that experience higher SNR, are allotted with a higher number of bits, whereas less bits are allotted to sub-carriers experiencing lower SNR. Underwater OFDM has been shown to provide data rates of 12 kbps, 25 kbps, and 50 kbps with bandwidths of 12kHz, 25kHz and 50kHz respectively [95]. The subcarriers are divided in a way to ensure that each carrier is long compared to the multipath spread in the channel [127, 128] so that intersymbol interference may be ignored, greatly simplifying the receiver complexity. Although intersymbol interference may be ignored, the large Doppler spread in the underwater channel introduces significant interference between subcarriers; thus receivers must be designed to overcome intercarrier interference increasing their complexity.

Selection of FSK: The proven robustness of FSK and its simplicity make

it an attractive modulation scheme for our low-cost modem design for short-range, low-data rate applications. The scheme requires a simple receiver which can fit onto a small, low-power device as evidenced by the FSK mode of the WHOI modem which only uses 0.18 W for the receive processing as compared to its PSK receiver which uses 2 W for processing [139], or the UCSB DSSS AquaModem which uses 1.6 W for processing [140]. Binary FSK also does not require a large bandwidth which is suitable for our narrow-band low-cost transducer and corresponding analog transceiver design. Although data rates are low, they are suitable for the low-data rate applications of interest.

7.2 Hardware Platforms

This section briefly discusses four possible digital hardware platforms for our digital transceiver design including Microcontrollers (MCUs), Digital Signal Processors (DSPs), Application Specific Processors (ASICs), and Field Programmable Gate Arrays (FPGAs). We highlight the advantages and disadvantages of each platform and describe the selection of an FPGA for the UCSDModem.

Microcontrollers: Microcontrollers, or MCUs, are general-purpose devices consisting of a relatively small CPU, clocks, timers, I/O ports and memory. They are used for information processing and control and can be adapted to a wide variety of applications by software. Microcontrollers offer design flexibility and non recurring engineering costs as they can be easily reprogrammed in software and are widely available. The disadvantage is that an MCU has limited computation abilities and is only a viable solution for relatively simple applications at low sample rates. Compact code that makes the most efficient use of the MCU architecture is essential.

A few research underwater acoustic modem designs discussed in Chapter 4 make use of microcontrollers, including the Atmega128L [77, 82] and the Blackfin 533 [83]. The design in [77] is claimed to have a power consumption of only 25mW, but it relies on an RF ASIC to do most of the processing. The Blackfin 533 used in [83] is claimed to have a power consumption of 280 mW [129].

Digital Signal Processors: Digital signal processors are specialized microprocessors with an optimized architecture for the fast operational needs of digital signal processing applications [130]. DSPs offer many architectural features that reduce the number of instructions necessary for efficient signal processing. Integrated specialized compute engines increase performance by executing complex functions in hardware. Like MCUs, DSPs offer design flexibility and non recurring engineering costs as they can be easily reprogrammed in software and are widely available. Until recent years, DSPs were notoriously power hungry, but with the advent of new low-power, fixed point DSPs, power consumption has come down.

Most existing research underwater modem designs (both commercial and research) make use of DSPs as they are relatively easy to program and can meet the computational requirements of more complex digital signal processing algorithms. The DSSS design in [80] and the PSK design in [75] both make use of a floating-point TI TMS320C6713 processor and consume 2W and 1.6 W respectively. The FSK mode of [75] makes use of a low-power fixed point DSP consuming only 180mW of power.

Application Specific Processors: An application specific processor, or ASIC, is custom-designed for a particular application, with as much system functionality implemented on a single die. ASICs offer exceptional performance, small size, and low power as they optimize transistor use and clock cycles at the expense of flexibility. They have been shown to offer 20X [131] to orders of magnitude lower power consumption than any competing platform [132]. ASICs have a long time to market and high non recurring engineering costs making them practical only for high volume production or for designs that demand extremely tight size and power requirements. To the best of our knowledge, no ASIC underwater acoustic modem exists.

Field Programmable Gate Arrays: A field programmable gate array is an integrated circuit designed to be configured by the customer or designer after manufacturing. FPGAs strike a balance between solely hardware (ASIC) and solely software (DSP or MCU) solutions as they have the programmability of software with performance capacity approaching that of a custom hardware implementation.

They also present designers with substantially more parallelism allowing for a more efficient application implementation [133, 134, 135, 136, 137, 138]. Studies have shown that FPGAs have evolved into highly valued digital signal processing solutions platforms that reduce overall system costs and power consumption for high throughput applications [141, 142](further comparison studies are required to determine whether an FPGA provides power and cost benefits for simpler, lower throughput applications [142]). However, they require specialized knowledge and increased design time over DSP and MCUs.

Of the research modems we discussed in Section 2, none solely make use of an FPGA, although two designs use an FPGA for pre-processing [86, 87]. Power consumption estimates are not provided.

Selection of FSK: As FSK based underwater acoustic modems have already been implemented on a DSP [75] and a Microcontroller [83], we selected to implement our FSK modem on an FPGA to serve as a comparison (particularly in terms of cost and power consumption) to these designs. Also, FPGAs provide a relatively easy transition to ASIC should a large volume of modems need to be produced.

7.3 Digital Transceiver

Now that we have described the selection of the modulation scheme and the hardware platform, this section provides a thorough description of our FPGA implementation of the FSK digital transceiver, including the modulator, digital down converter, symbol synchronizer, demodulator, and clock structure. The complete design is shown in Figure 7.4. Each component was designed in Verilog and initially tested individually in ModelSim [143] to verify its operation prior to system integration.

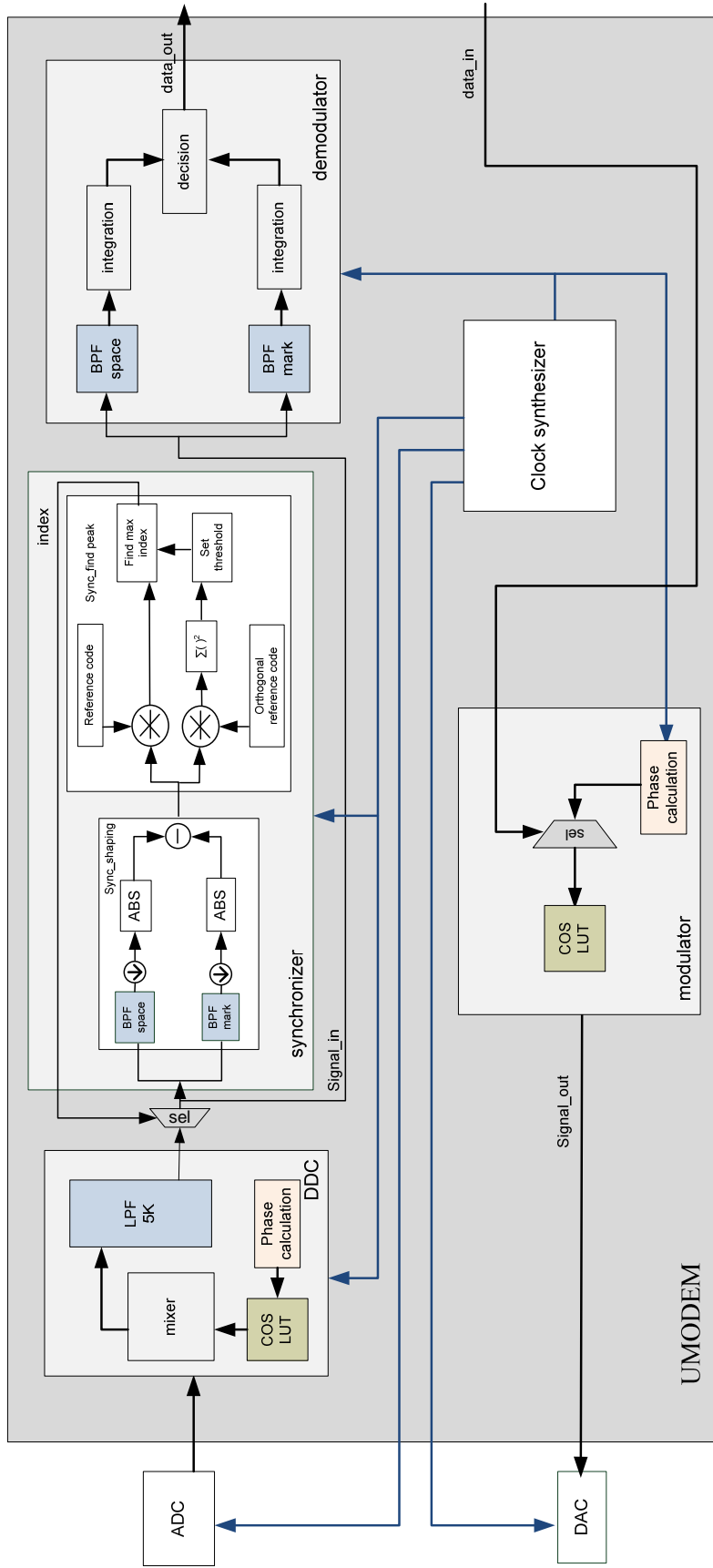


Figure 7.4: Block Diagram of Complete Digital Receiver

The digital transceiver design makes use of the parameters given in Table 7.1. The carrier frequency and frequency separation were selected to match the transducer’s resonance frequency and narrow bandwidth. Nyquist sampling necessitates that the signal be sampled at 2X the frequency of the highest frequency component of the signal, but in practical applications 4-6X sampling is desired. Thus the given sampling frequency and processing frequency were selected to provide sufficient oversampling of the desired frequency component while being integer multiples of one another. The symbol duration was selected to provide a suitable raw bit rate for low-data rate sensor networking applications.

Table 7.1: Digital Transceiver Parameters

Properties	Assignment
Modulation	FSK
Carrier Frequency	40 kHz
Mark Frequency	2 kHz
Space Frequency	1 kHz
Symbol Duration	5 ms
Sampling Frequency	192 kHz
Processing Frequency	16 kHz

7.3.1 Modulator

In a digital transceiver, the modulator is responsible for translating a bit stream into a waveform that can be physically transmitted. For binary FSK, digital data are transmitted over the analog channel by shifting the frequency of a continuous carrier to the ‘mark’ or ‘space’ frequency every symbol period depending on whether a digital ‘1’ or ‘0’ is present respectively. Figure 7.5 shows the implementation of the FSK modulator. The modulator takes a binary input (*data_in*) and selects (*sel*) to generate a sinusoidal wave (*Signal_out*) with the mark or space frequency using a cosine look-up table (*COSLUT*). The correct frequency is generated by calculating the phase angle offset required to represent the desired frequency and accumulating the phase offset over one symbol period to produce the sine wave (*Phasecalculation*). The offset is calculated using the

formula:

$$Offset = round(size * F/F_s) \quad (7.1)$$

Where *size* is the number of elements in the look up table, *F* is the mark or space frequency and *F_s* is the sampling rate (in our case 192kHz). The only area consuming portion of the modulator is the cosine look up table. To save resources, we selected a look up table of size 65536 - the smallest look up table that produced offsets that were different enough to distinguish between the desired mark and space frequencies.

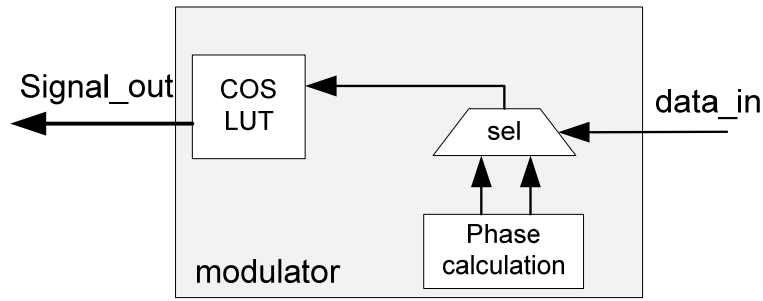


Figure 7.5: Block Diagram of FSK Modulator

7.3.2 Digital Down Converter

The digital down converter, DDC, (Figure 7.6) is responsible for converting high resolution signals to lower resolution signals to simplify subsequent processing. It takes the incoming signal from the ADC (*adc_in*) and multiplies it with a continuous 40kHz signal generated from a cosine look up table (*COSLUT*) using the same phase calculation (*Phasecalculation*) method described in the previous section. The mixed signal then passes through a 5kHz low pass filter (*LPF5K*) to filter out the high frequency components of the mixed signal leaving a 1k signal as the space frequency and a 2kHz as the mark frequency (*Signal_out*). The DDC then down samples the signal from 192kHz to 16kHz, the processing frequency. To reduce the resource usage of the down converter, the look up table from the

modulator is reused (as the modem cannot transmit and receive at the same time). The low-pass filter is a small 20-tap FIR filter designed using Spiral [144], a filter design program from Carnegie Mellon well known for creating compact filters.

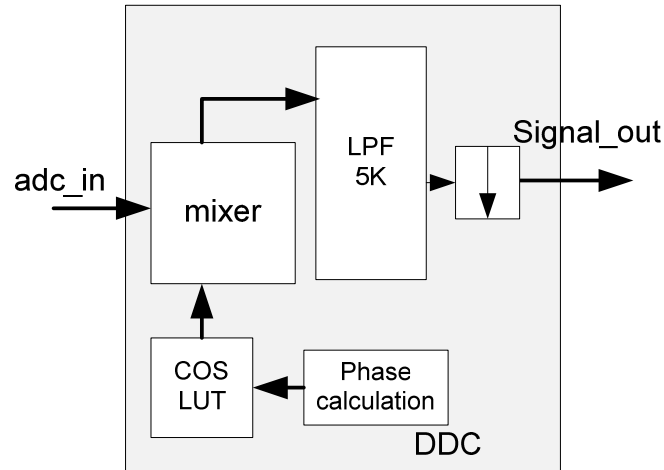


Figure 7.6: **Block Diagram of Digital Down Converter**

7.3.3 Symbol Synchronizer

Symbol synchronization, the ability of the receiver to synchronize to the first symbol of an incoming data stream [145], is a critical component in the design of an underwater acoustic modem. When the modem receiver obtains an input stream, it must be able to find the start of the data sequence to set accurate sampling and decision timing for subsequent demodulation. Symbol synchronization is particularly important in the underwater acoustic channel as the channel can be highly variable and plagued by multipath, variable noise levels, path-loss, Doppler shifts, and long propagation delays [146, 19]. Without accurate symbol synchronization, higher bit error rates incur thus reducing the reliability and quality of service of the wireless network. As the symbol synchronizer is the most complicated aspect of the digital transceiver design, many pages are devoted to its description. We describe the selection of symbol synchronization scheme and its hardware implementation.

Synchronization Scheme

The most common and simple symbol synchronization approach relies on the transmission of a predefined sequence of symbols, often referred to as a training, or reference sequence. The transmitter sends a packet that begins with the reference sequence and the receiver compares the received sequence with the known reference sequence in order to locate the start of the packet [145, 147]. The comparison is effectively performed by correlating the received sequence with the reference sequence when a new sample is received. When the reference and receiving sequence exactly align with each other, the correlation result reaches a maximum value and the synchronization point is located (Figure 7.7).

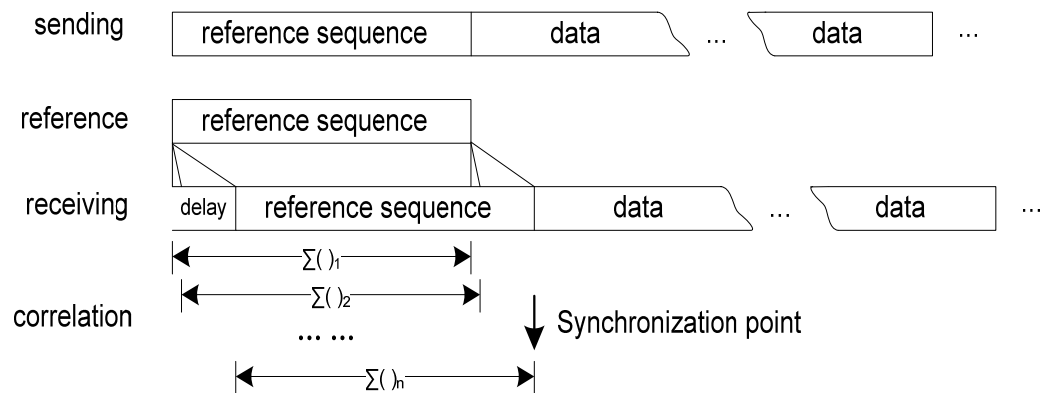


Figure 7.7: **Process of Symbol Synchronization**

Though this synchronization method is straight forward in theory, there are many design choices that must be considered before implementing the algorithm:

- How can the peak correlation result be detected effectively?
- What reference code is appropriate for the application?
- How will the reference code be represented?
- How long should the reference code be?

Typical methods to detect a correlation peak involve setting a correlation threshold where the correlation result only rises above the threshold when the

receiving sequence and reference sequence are perfectly aligned. The threshold must be large enough to minimize the number of false alarms (the system detects the reference code is present when it is not), but small enough to guarantee the peak will still be detected when the signal level is low.

The underwater acoustic channel is highly variable and plagued by variable noise levels, path-loss, and long propagation delays [146, 19]. Thus, selecting a static correlation threshold for the underwater receiver is impractical as the received signal strength and noise level are changing in real-time. We therefore need to set a dynamic correlation threshold based on a dynamic estimation of the noise level. As a data packet could be sent at any time, it is hard to find a suitable rate for the receiver to take ‘noise’ samples periodically to set the dynamic threshold. The receiver must be able to set an appropriate threshold whether data or noise are present. The goal can be achieved through the use of an orthogonal reference sequence. As shown in equations (7.2-7.5), the receive sequence, $R(t)$, contains both the delayed transmitted sequence (the reference sequence followed by data), $S(t-\tau)$, and noise $n(t)$ in (7.2). When we correlate the received sequence with the reference code, $r(t)$, and the orthogonal reference code $r_o(t)$ at the receiver separately, the correlation result of the reference branch $C(t)$ (7.3) contains both signal and noise portions, whereas the correlation result of the orthogonal branch $C_o(t)$ (7.4) contains solely the noise correlation result. We can therefore estimate the real-time noise level by calculating the standard deviation of the correlation result of the orthogonal branch $T(t)$ (7.5) and set the threshold according to this result. Though the threshold calculation is not a true estimate of the noise (as it includes the ‘noise’ from the imperfection of the orthogonal correlation), it serves as a reasonable threshold for peak detection.

$$R(t) = S(T - \tau) + n(t) \quad (7.2)$$

$$C(t) = R(t) * r(t) = \Sigma_j R(t)r(t + j) \quad (7.3)$$

$$\begin{aligned} C_o(t) &= R(t) * r_o(t) = \Sigma_j R(t)r_o(t + j) \\ &= \Sigma_j S(t - \tau)r_o(t + j) + \Sigma_j n(t)r_o(t + j) \\ &= \Sigma_j n(t)r_o(t + j) \end{aligned} \quad (7.4)$$

$$T(t) = \Sigma_j C_o(t)^2 = \Sigma_j n(t)^2 r_o(t + j)^2 \quad (7.5)$$

In order to make use of the scheme described above, we must select a reference code that has an excellent periodic and aperiodic autocorrelation function, and an excellent cross-correlation function (with values close to zero) with its orthogonal code. We considered using Gold codes, Walsh codes, and PN sequences. Figure 7.8 shows the autocorrelation (blue) and cross-correlation with an orthogonal code for the Gold, Walsh, and PN sequences respectively.

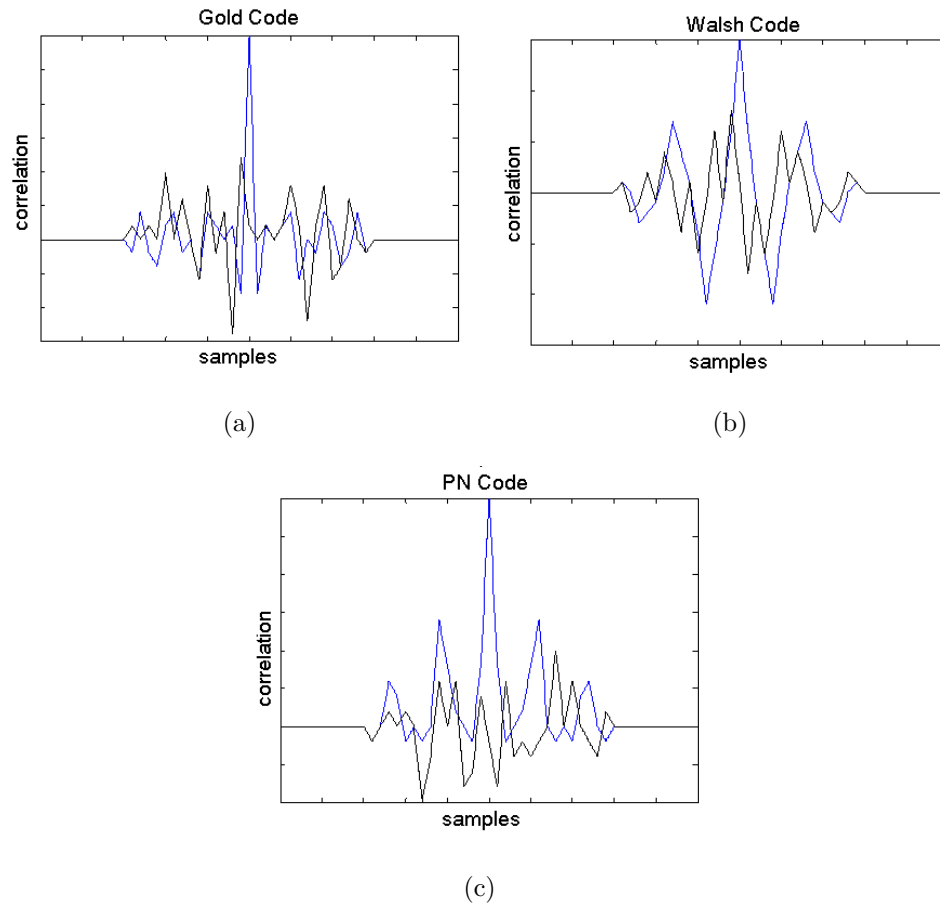


Figure 7.8: Auto Correlation (blue) and Cross Correlation (black) of Orthogonal Gold (a), Walsh (b) and PN (c) Reference Codes

Because of the Gold Code's superior autocorrelation and cross correlation properties, we selected to use two orthogonal Gold Codes for our reference and orthogonal reference sequence. Gold codes show reasonable cross-correlation and off-peak autocorrelation values while providing perfect orthogonality in the zero-offset case [147].

Gold codes are binary sequences of length 2^m-1 consisting of '1's and '-1's. As the underwater acoustic receiver uses FSK modulation, we can represent the Gold code by using the mark frequency to represent a '1' and a space frequency to represent a '-1.' However, representing the Gold code as a sequence of sinusoids eclipses its desired auto-correlation and cross-correlation properties. Thus we need to introduce a 'signal shaping' function before computing a correlation to make the receiving sequence look like a sequence of '1s' and '-1s' instead of a sequence of sinusoids.

We select an appropriate reference length for the Gold code by simulating the symbol synchronization method in MATLAB with a packet consisting of Gold code of lengths 3, 7, 15, and 31 followed by 80 symbols of data with a value of 15dB SNR. Ten thousand simulations produced correct results and a sharp and distinct peak for the synchronization point for packets with Gold codes of length 15 and 31, but failed to produce accurate results for packets with Gold codes of length 7 and 3. Thus, we select a reference code length of 15 as it is the minimum length that provides accuracy. Figure 7.9 shows the simulation result for a packet with a reference code of length 15. The dashed line shows the result of the orthogonal correlation, the thick line shows the resulting threshold and the solid line shows the reference correlation result. The result of the correlation and orthogonal correlation is virtually zero when only noise is present. The correlation result first rises above the threshold when the data packet is present and the synchronization point is accurately detected as the highest point above the threshold within the following two reference lengths. A two reference length period is selected as the peak searching interval because it takes two reference lengths for an incoming reference signal to enter and exit the interval of correlation.

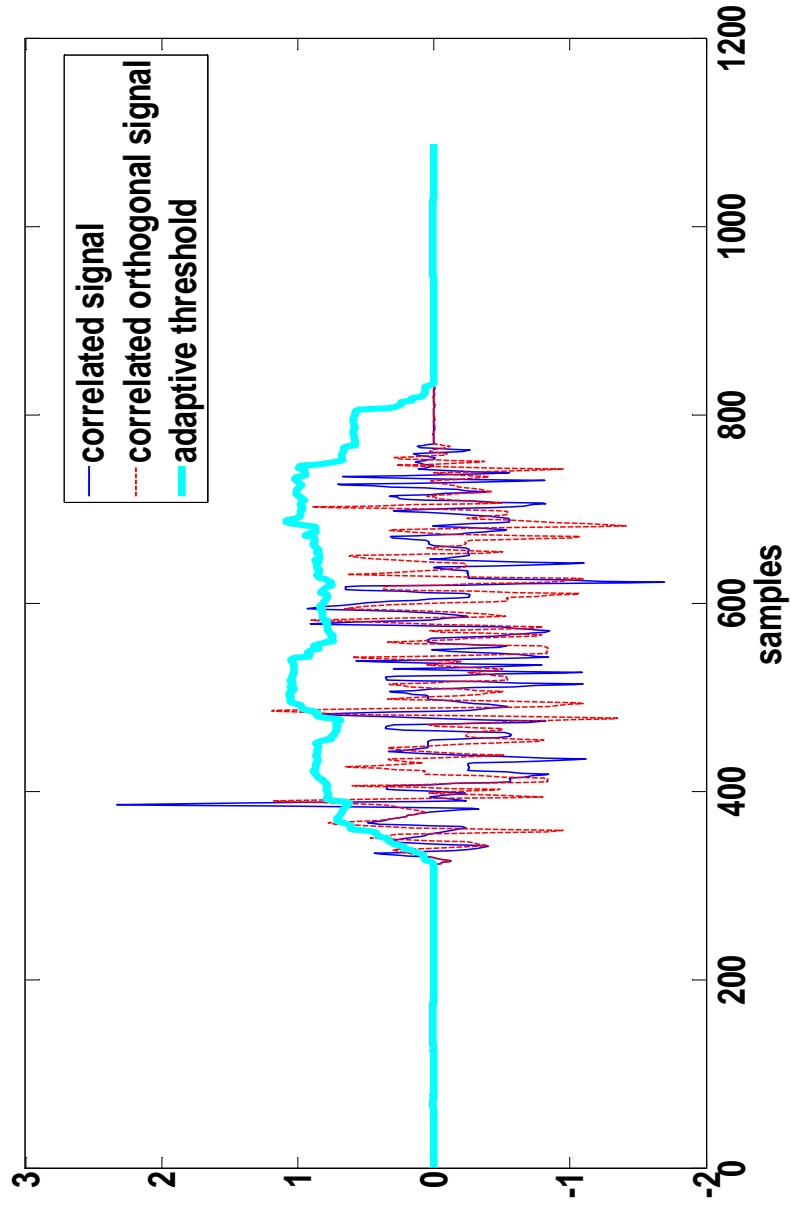


Figure 7.9: MATLAB simulation of symbol synchronization for underwater FSK

Our symbol synchronization scheme for underwater FSK is therefore given in Figure 7.10. The input signal, Sig_in , is the baseband signal coming from the DDC. The signal first passes through a signal shaping block which shapes the input signal from a sinusoid to a square-like wave. The signal shaping block consists of the same mark and space filters as those in the demodulator followed by a down sampler, absolute value operation, and subtraction. The effect of the filters is to remove out-of-band noise and begin to shape the signal as having regions of different amplitudes. The down sampler and absolute value operations further smooth the signal into an all positive square-like wave. The subtraction produces the desired square-like wave consisting of positive and negative numbers ready for correlation with the reference code consisting of ‘1s’ and ‘-1s.’

After the signal passes through the shaping block, it then performs a parallel correlation with the expected reference code and orthogonal reference code. The result of the correlation with the orthogonal branch is squared and summed to compute its standard deviation and serve as a threshold for the reference code correlation operation (as previously described). The ‘find max index’ logic compares the reference correlation result with the threshold. When the reference correlation result rises above the threshold, the logic looks for the highest peak above the threshold over two reference length periods to ensure it can find the highest peak that denotes the synchronization point. The index of peak position is recorded and sent to the demodulator for accurate symbol timing.

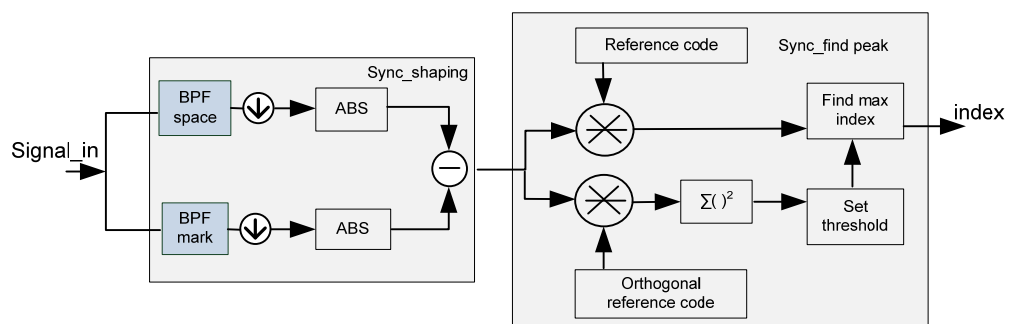


Figure 7.10: **Block Diagram of Symbol Synchronization for Underwater FSK**

Hardware Implementation

In order to implement our symbol synchronization design into hardware, we need to consider the design parameters of our acoustic receiver. Recall that the ADC sampling rate is 192KHz and the symbol period is 5ms. These parameters give a total of 960 samples per symbol. With a reference length of 15 symbols, the entire reference sequence is 14,400 samples. Multiply that by 2 to include the orthogonal reference sequence. Correlating 28,800 samples requires 28,800 multiplications and 28,798 additions. These operations are either too area-consuming or computationally infeasible to complete in one 192KHz sampling clock period (5.2 us). We thus focus our hardware design implementation on reducing the complexity of the correlation.

The signal shaping block down samples the incoming signal to shape the signal into a square-like wave. As a square wave only requires one bit to represent the sequence, we down sample the original signal by 240 to create a signal sequence consisting of 4 samples per symbol (4x oversampling), or 60 samples. We therefore require a correlator that can handle 120 multiplications (including the orthogonal branch) and 118 additions in one 800Hz (192kHz/240) clock period. Our correlation architecture (for one correlation branch) is given in Figure 7.11. In each 800Hz clock period, the shaped signal is shifted into a 60 element shift register that must be correlated with the reference signal. In order to reduce the path length, we applied a 4KHz local clock to pipeline the storing. As the reference signal is represented by '1's and '-1's, we can simplify the correlation operation by replacing the multiplications with a sign selection method (SS core): when the reference signal is a '1', add the relevant stored shaped signal, when the reference signal is a '-1' subtract the relevant stored shaped signal.

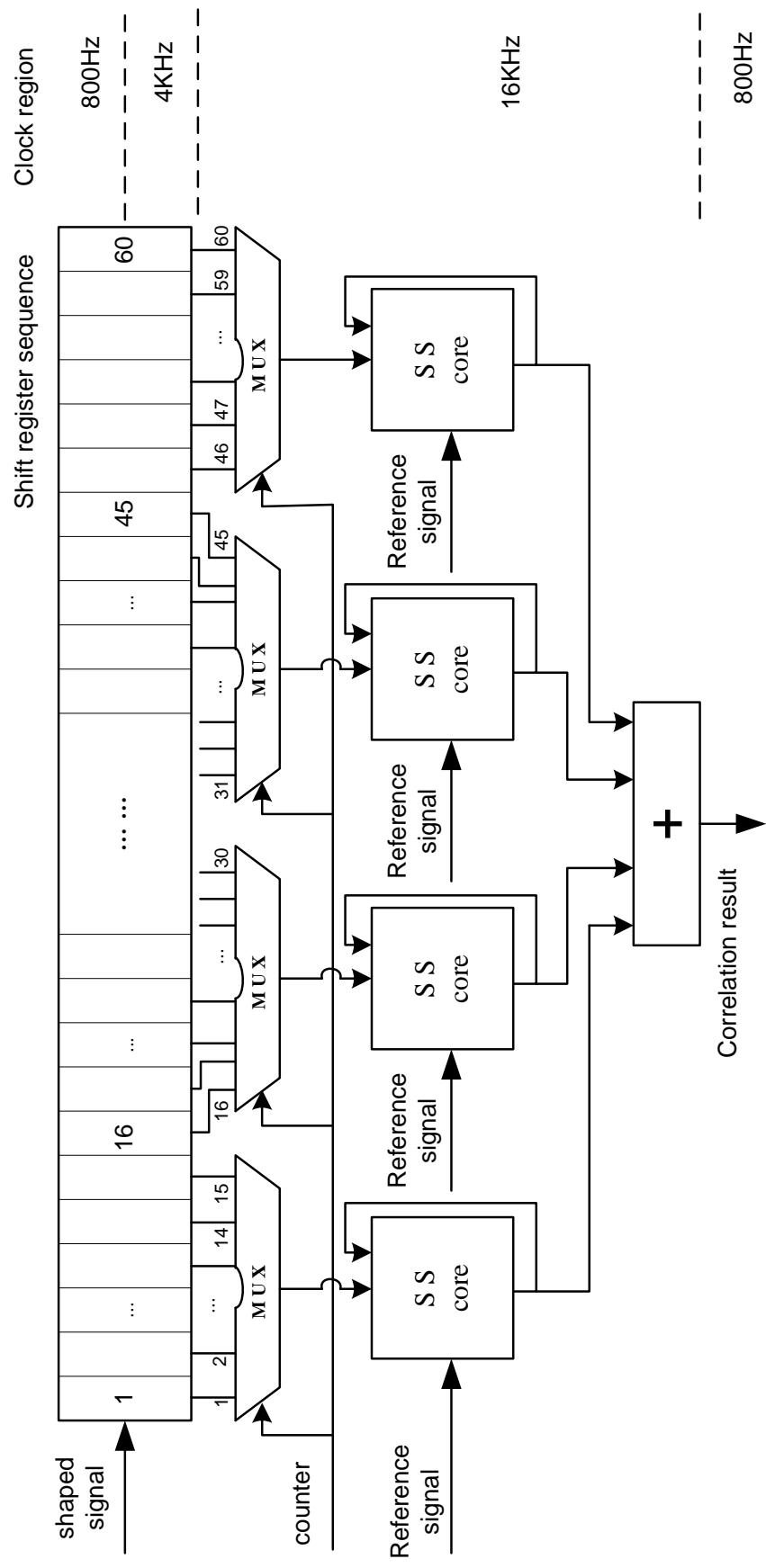


Figure 7.11: Hardware Units of Correlation Implementation for Underwater FSK

We implement the correlation in a 15-stage pipeline, as a fully parallel shift register implementation would require too many resources and a fully serial shift register implementation would require a significantly faster clock. The appropriate 15 elements of the shift register are serially selected into an SS core at a 16KHz clock rate to achieve a partial correlation result. The outputs of four SS cores are then summed in one 800Hz clock period to produce the complete correlation result. Thus we achieve a compact, timing accurate correlation implementation. The symbol synchronization has a delay of eighty 16KHz clock cycles, one for clocking data in, 60 for shifting the signal into the correlator, 15 for the pipelined additions and 4 for shifting the result to the output.

The rest of the symbol synchronization design is computationally inexpensive; the filters consist of two small 20-tap FIR filters designed using [144] and the threshold calculator only requires one multiplier and one adder. The 800Hz clock used for synchronization is source synchronous with the 192KHz sampling clock and 16KHz demodulator clock to avoid clock confliction.

Upon startup the modem must initialize the known reference code and orthogonal reference code to memory at the 192KHz clock rate and perform an initial correlation over one reference length (60, 800Hz clock cycles) to ensure a valid threshold value. The total initialization occupies 75ms.

After initialization, the synchronizer executes as previously described: shaping the incoming signal, correlating it with the reference code and orthogonal reference code and searching for a correlation result above the threshold. When the reference correlation result rises above the threshold, the block looks for the highest peak above the threshold over two reference length periods to ensure it can find the highest peak that denotes the synchronization point. The control structure is shown in Figure 7.12 and described in the following paragraphs.

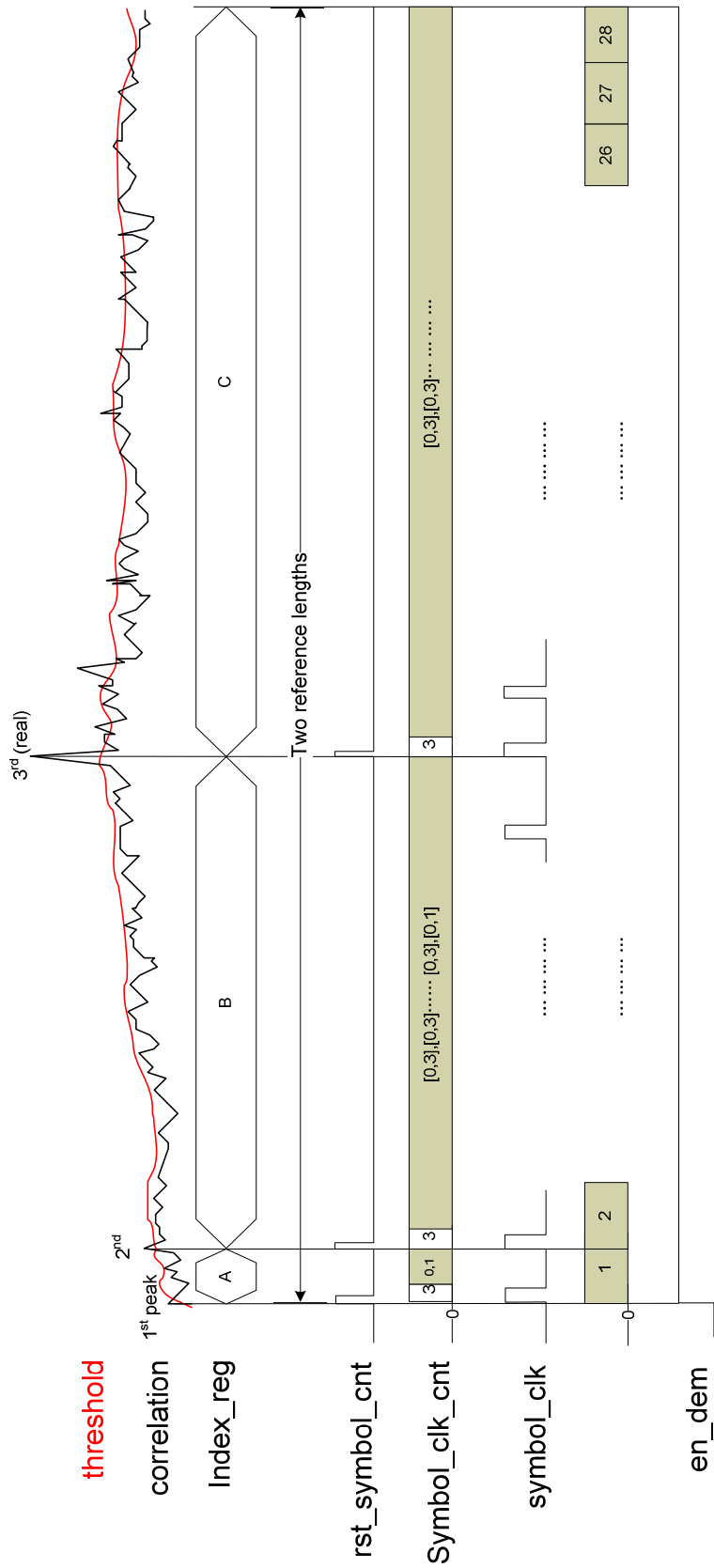


Figure 7.12: Control Structure of Symbol Synchronization for Underwater FSK

When the correlation result first rises above the threshold, we assume that this point is the synchronization point and thus need to start the symbol clock. Recall that the down-sampled clock used for synchronization is 800Hz and the symbol clock is 200Hz; therefore a symbol clock can be formed by 4 cycles of the down-sampled clock. Thus, at the time a peak occurs (1st peak), a reset signal is asserted (*Rst_symbol_cnt*) to reset a 2 bit counter (*Symbol_clk_cnt*) which is used to generate the symbol clock every four 800Hz cycles. In the meantime, the index of the peak location, A, is stored into a real-time index register (*index_reg*) and the demodulator is enabled (*en_dem*). The real-time demodulated values are then stored in a temporary buffer and the number of demodulated symbols is counted by another counter (*symbol_num_count*).

If another, larger peak, occurs within two reference lengths (2nd peak), *rst_symbol_cnt* is asserted to resynchronize the symbol clock at this higher peak point. The value of *index_reg* is also replaced to B (the number of samples offset from the initial peak A). The counter, *symbol_num_count*, continues to count the number of demodulated symbols and the demodulated results are stored in a temporary buffer. The values already demodulated between A and B will be ignored as the peak at A was not the maximum. When an even larger, real peak occurs (3rd), *rst_symbol_cnt* is again re-asserted to resynchronize the symbol clock at this higher peak. The value of *index_reg* is set to C (the number of samples offset from the initial peak A). Since B was not the maximum either, the values already demodulated between time A and C will have to be ignored.

At the end of two reference lengths, the location of the maximum peak, C, can be found in *index_reg* and the number of symbols demodulated since the first peak can be found in *symbol_num_count*. We can then calculate the address of the first valid piece of data in the temporary buffer with the following equation:

$$addr = symbol_num_cnt - round \left[\frac{NO_OF_SAMPLES - 1 - index_reg}{DS_FACTOR} \right] \quad (7.6)$$

where *NO_OF_SAMPLES* is the number of samples in two reference lengths (120), *DS_FACTOR* is the down sampling factor between the synchronization clock (800Hz) and the symbol clock (200Hz) and $round[(NO_OF_SAMPLES -$

$1 - \text{index_reg}] / \text{DS_FACTOR}]$ gives the number of symbols demodulated since the synchronization point (C) found in *index_reg*.

After the modem has demodulated the entire packet, it deserts the *en_dem* signal and the synchronizer returns to searching for a correlation result above the threshold to synchronize on the next incoming packet.

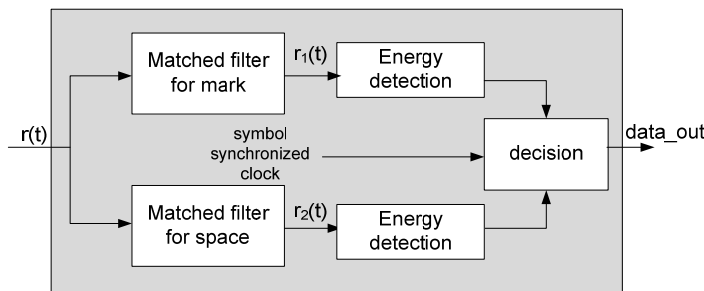


Figure 7.13: **Block Diagram of Matched Filter FSK Demodulator**

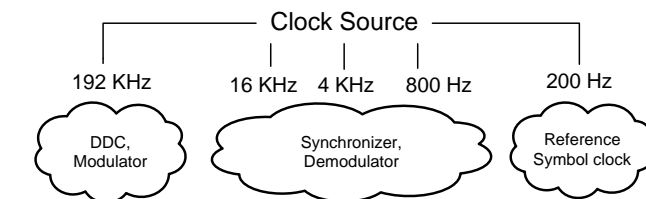
7.3.4 Demodulator

A demodulator converts the analog waveform it receives back into the digital signal that was transmitted. For FSK, this means it detects the mark and space frequencies in the received signal and converts them back to digital ‘1’s and ‘0’s respectively. The classic ‘matched’ filter demodulator is optimal for FSK detection with white Gaussian noise interference [148]. The demodulator (Figure 7.13) works by sending a symbol duration of the received signal (the output of the DDC) through two bandpass filters (one filter that is centered around the mark frequency (2kHz) and the other that is centered around the space frequency (1kHz)). The demodulator then integrates the output of each filter over one symbol period (energy detection) to determine the relative amount of energy in each frequency band. If the energy of the mark filter is greater than the energy of the space filter a ‘1’ was sent whereas if the energy of the space filter is greater than the energy of the mark filter a ‘0’ was sent. Our matched filter demodulator uses the same compact filters as the symbol synchronizer designed by [144]. To save design space, no embedded multiplier is used in our demodulator. The decision module includes two

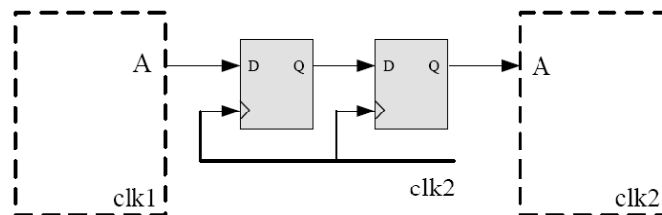
accumulators in order to add the output of low pass filters in a symbol period, and a comparator to select the greater one of the accumulators to make the decision.

7.3.5 Clock Generation

The digital transceiver makes use of multiple clocks: the sampling clock, the baseband clock, the symbol clock, and the clocks used for synchronization. All clocks are integer divided with logic from a single clock source as shown in Figure 7.14(a) to avoid clock confliction and ensure they are source synchronous. An extra flip flop was added between clock domains (as shown in figure 7.14(b)) to avoid random problems caused by metastability.



(a)



(b)

Figure 7.14: (a) Clock Division, (b) Added Flip Flop between clock domain to avoid metastability

7.3.6 HW/SW Co-Design Controller

We used Xilinx Platform Studio 10.1 to build a HW/SW co-design for accurate control and I/O of the digital transceiver. The co-design consists of the digital transceiver, a UART (Universal Asynchronous Receiver Transmitter) to connect to serial sensors or to a computer serial port for debugging, an interrupt controller to process interrupts received by the UART or the modem, logic to configure the on board ADC, DAC, and clock generator, and MicroBlaze, an embedded micro-processor to control the system (Figure 7.15).

The MicroBlaze processor is a 32-bit Harvard Reduced Instruction Set Computer (RISC) architecture optimized for implementation in Xilinx FPGAs. It interfaces to the digital modem through two fast simplex links (FSLs), point-to-point, uni-directional asynchronous FIFOs that can perform fast communication between any two design elements on the FPGA that implement the FSL interface. The MicroBlaze interfaces to the interrupt controller and UART core over a peripheral local bus (PLB), based on the IBM standard 64-bit PLB architecture specification.

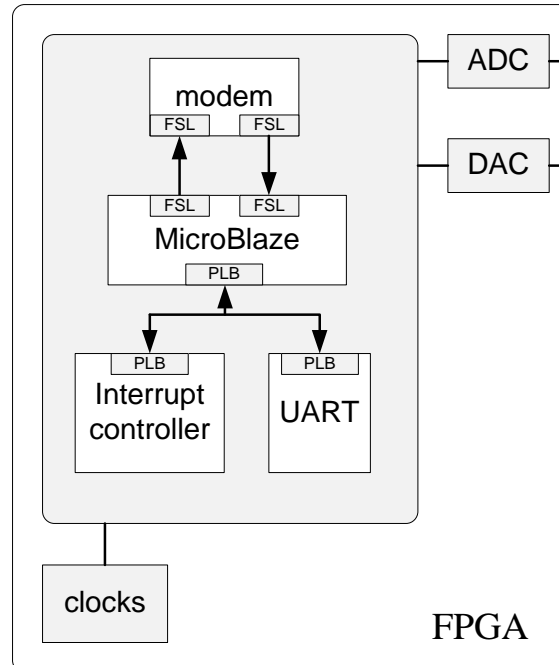


Figure 7.15: HW/SW Co-Design for the digital transceiver

Upon start-up, the MicroBlaze initializes communication with the digital transceiver through sending a command signal through the FSL bus signaling the digital transceiver to turn on. When the digital transceiver is ready to begin receiving signals, it sends an interrupt back to MicroBlaze to indicate initialization is complete. The digital transceiver then begins the down conversion and synchronization process, processing the signal received from the ADC and looking for a peak above the threshold to indicate a packet has been received. If the digital transceiver finds a peak above the threshold, it finds the synchronization point, and demodulates the packet. The demodulated bits are stored in the FSL FIFO.

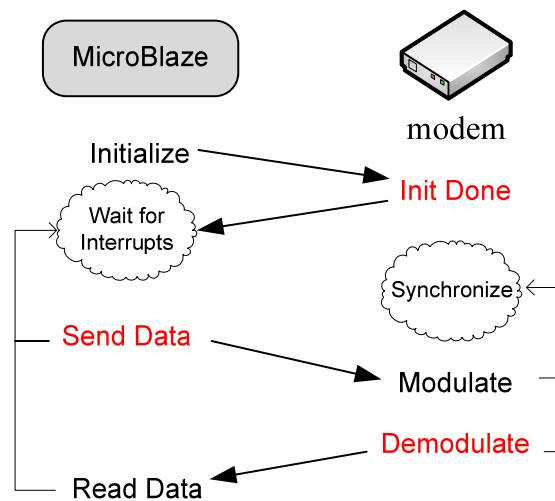


Figure 7.16: **Digital Transceiver Control Flow. Interrupts are shown in red**

When the full packet has been demodulated, the digital transceiver sends an interrupt indicating a packet has been received and the MicroBlaze may retrieve the packet from the FSL. The digital transceiver then returns to synchronization, searching for the next incoming packet. After initialization, the MicroBlaze remains idle, waiting for interrupts either from the digital transceiver or UART. If it receives an interrupt from the digital transceiver indicating that a packet has been demodulated, the MicroBlaze reads the bits from the FSL FIFO and sends the bits over the UART to be printed on a computer's Hyperterminal for verification. If the MicroBlaze receives an interrupt from the UART, indicating that the user

would like to send data, the MicroBlaze sends a command to the transceiver to send the bitstream the MicroBlaze places in the FSL. The digital transceiver then modulates the data from the FSL and sends the modulated waveform to the DAC for transmission. The MicroBlaze then returns to waiting for interrupts from the transceiver or the UART and the transceiver returns to synchronization, searching for the next incoming packet. This control flow is depicted in Figure 7.16.

7.4 Resource Requirements

Table 7.2 shows the FPGA hardware resources occupied for each component of the digital transceiver. The resources reported for ‘Total’ include the complete digital transceiver and HW/SW co-design controller. These resources were mapped for a Spartan 3 XC3S4000, the smallest device in the established Spartan 3 family that can fit the design.

Table 7.2: Digital Design Resource Usage

	Occupied Slices	LUTs	BRAMs
Modulator	95	184	9
DDC	284	541	9
Demodulator	1025	1980	1
Synchronizer	12000	22101	2
Total (% Spartan3)	16706 (60%)	29076 (51%)	55 (57%)

We obtained a power estimate of the complete FSK modem design on various FPGA devices by entering the resource values of the total modem into the Xilinx XPower Estimator 9.1.03 and the Altera Cyclone IV PowerPlay Early Power Estimator. We acknowledge that the resource values determined for one device are not an exact estimate of the resource values needed for another device, but they do provide us with a reasonable first order resource (and power) estimate. Also note that the estimates reported for the Xilinx devices are more accurate than those reported for the Altera device as the current design makes use of a Xilinx MicroBlaze core which would have to be replaced with the Altera NIOS processor should the design be implemented on an Altera chip. The devices reported are

in device families known for their low power consumption (the Xilinx Spartan 6 and the Altera Cyclone IV being some of the newest FPGA device families on the market). The particular devices reported are the smallest devices in their family that fit the total modem design. The letters ‘Q’, ‘D’, and ‘T’ in Table III stand for ‘quiescent,’ ‘dynamic’, and ‘total’ power respectively. The last column of Table 7.3 reports the size of device family’s CMOS technology.

Table 7.3: FPGA Power Consumption

Family	Device	Q Pwr (W)	D Pwr (W)	T Pwr (W)	Tech (nm)
Spartan 3	XC3S4000	0.274	0.105	0.379	90
Spartan 6	XC6SLX150T	0.212	0.021	0.255	45
Cyclone IV	EP4CE30	0.087	0.06	0.147	60

From Table 7.3 we observe that the quiescent power contributes significantly to the total power of the design. Thus, it is important to select a device that offers low quiescent power. Altera has invested considerable resources in reducing static power in their products as evidenced by our design’s low quiescent power on the Cyclone IV. Furthermore, the newer technologies (Spartan 6 and Cyclone IV) consume less power than the older technology, suggesting that with continued technological advancements, FPGA power consumption will continue to decrease.

Table 7.4 compares the total digital hardware platform processing power and cost of the UCSDModem design with existing research underwater modem digital designs that report their total processing power. As previously described, these research modem designs use various modulation schemes (FSK, PSK, or DSSS) and are implemented on various hardware platforms.

Table 7.4: Digital Transceiver Design Comparison

Modem	Mod	Category	Platform	Total Pwr (W)	Cost (\$)
[139]	FSK	FixedDSP	TMS320C5416	0.180	45
[139]	PSK	FP DSP	TMS320C6713	2.0	25
[140]	DSSS	FP DSP	TMS320C6713	1.6	25
[83]	FSK	MCU	Blackfin 533	0.280	25
UCSD Modem	FSK	FPGA	XC6SLX150T	0.233	14
			EP4CE30	0.147	40

From Table 7.4 we notice that the designs implemented on floating point DSPs consume considerably larger power than any of the other designs. However, these designs use more complex modulation schemes and thus require more resources. The FSK design in [139] on the fixed point DSP and the FSK design in [83] on a microcontroller provide comparable power consumption to our FSK design on an FPGA.

The cost reported for the DSP, Microcontroller, and FPGA devices were all found on electronic distributor websites. These estimates suggest that the FPGA design also provides a comparable cost to other digital hardware platforms.

7.5 Summary

This chapter described the design of the UCSDModem's FSK FPGA based digital transceiver including the modulator, digital down converter, symbol synchronizer, demodulator, clock generator, and HW/SW co-design. The design operates at 200 bps in a narrow band around a 40kHz carrier (to match the operating frequency of the transducer and the design of the analog transceiver) and provides comparable cost and power consumption to other frequency shift keying based modem designs. The next chapter describes the system tests used to evaluate the functionality and performance of the complete modem design.

The text of Chapter 7.3.3 is in part a reprint of the material as it appears in the proceedings of the IEEE International Conference on Sensor Networks, Ubiquitous, and Trustworthy Computing. The dissertation author was a co-primary researcher and author (with Ying Li). The other co-authors listed on this publication [3] directed and supervised the research which forms the basis for Chapter 7.3.3.

The text of Chapter 7.3.1, 7.3.2, 7.3.4, and 7.3.6 is currently being prepared for submission for publication of the material. The dissertation author is a co-primary researcher and author (with Ying Li). Ryan Kastner and Xing Zhang directed and supervised the research which forms the basis for Chapter 7.3.1, 7.3.2, 7.3.4, and 7.3.6.

Chapter 8

System Tests

In order to verify the operation of the UCSDModem, we first tested the analog components and digital components separately and then tested the full, integrated system in three different underwater environments at various ranges. This chapter describes the results of each test and summarizes the performance of our modem.

8.1 Analog Testing

To test the operation of our analog components (the transducer and analog transceiver), we took our analog hardware to Mission Bay, a salt water bay near San Diego, CA. One analog transceiver and transducer was placed on the dock to act as the transmitter (Figure 8.1 (a)) and another analog transceiver and transducer was placed on a boat to act as the receiver (Figure 8.1 (b)). The transmitter was powered by power supplies on the dock and the receiver was powered by a power supply connected to an inexpensive RadioShack AC/DC converter connected to the boat's power that unfortunately produced a substantial amount of noise (200mVpp).

We sent a 40kHz sinusoid from the transmitter to the receiver placed at three different locations as shown in Figure 8.2: 1. 75 meters, 2. 235 meters, and 3. 350 meters away. We were able to successfully detect the signal at 350m at the fourth output power level, however the receive signal was just above 200mVpp at



(a)



(b)

Figure 8.1:

Mission Bay Test Set Up. (a) Transmitter on dock, (b) Receiver on boat

this distance and hence could just be detected above the converter's noise. This test proved that our analog hardware could transmit a considerable distance and would likely be able to transmit a farther distance given a low-noise power supply at the receiver and further improvements to the analog transceiver.



Figure 8.2: Mission Bay Receive Distances 1. 75 m 2. 235 m 3. 350 m

8.2 Digital Testing

For digital testing, we purchased a prototype test platform, the DINI DMEG-AD/DA [151] that includes analog-to-digital and digital-to-analog converters, a Xilinx Virtex-4 FPGA, an onboard oscillator, and a serial port and downloaded the HW/SW co-design to the board (Figure 8.3). We also purchased two M-Audio ProFire 610 devices [152] to collect and store received waveforms for post-analysis. We conducted hard wired and bucket tests of the digital transceiver as described in the subsections below.

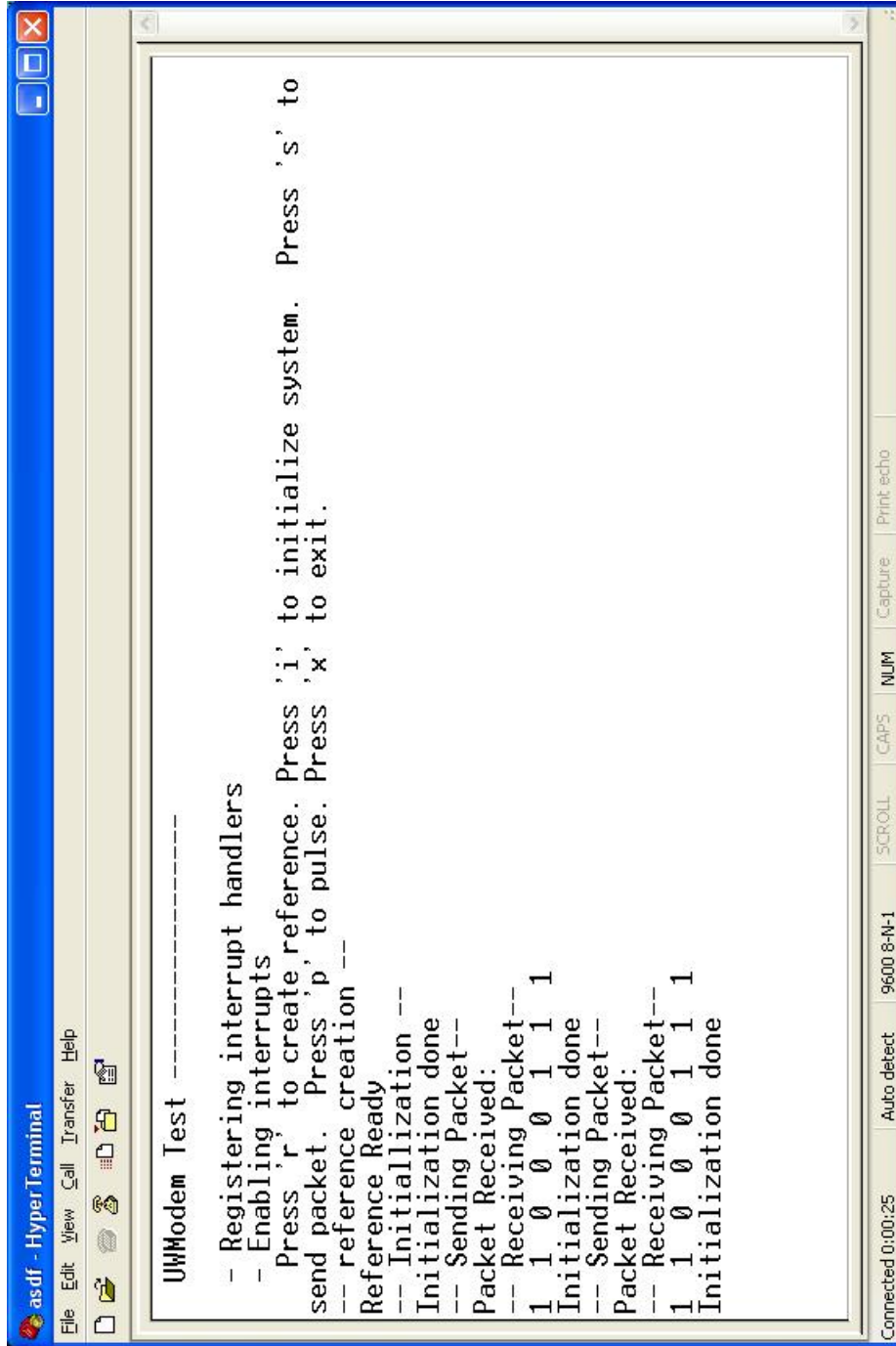


Figure 8.3: **DINI DMEG-AD/DA Test Platform**

8.2.1 Hard Wired Tests

To verify the functionality of our complete FPGA digital transceiver, we downloaded the HW/SW co-design to the DINI board, connected the output of the DAC directly to the input of the ADC, and sent packets consisting of the 15 bit Gold Code of ‘011001010111101’ followed by 8 bits (for easy visual verification of the data) or 100 bits (a data length comparable to that sent by sensors) of randomized ones and zeros. We used Hyperterminal to give the command to send a packet at random times and to display the decoded results of the modem. We used ChipScope Pro [153] to view the internal waveforms.

Figure 8.4 shows the HyperTerminal window of a test showing the correct transmission of two 8-bit data packets sent at different times according to the time the operator pressed the ‘s’ key. The modem continues to rest in a state waiting to receive the next packet.



The image shows a HyperTerminal window titled "asdf - HyperTerminal". The window contains a text-based output from a "UWModem Test". The output includes instructions for using 'i', 'p', and 's' characters, followed by a series of status messages and data packets. The status messages include "Reference Ready", "Initialization done", and "Packet Received". The data packets are binary strings: "1 1 0 0 0 1 1 1" and "1 1 0 0 0 1 1 1". The window also features a menu bar (File, Edit, View, Call, Transfer, Help), a toolbar, and a status bar at the bottom showing "Connected 0:00:25", "Auto detect", "9600 8-N-1", "SCROLL", "CAPS", "NUM", "Capture", and "Print echo".

```
UWModem Test -----
- Registering interrupt handlers
- Enabling interrupts
  Press 'r' to create reference. Press 'i' to initialize system. Press 's' to
  send packet. Press 'p' to pulse. Press 'x' to exit.
-- reference creation --
Reference Ready
-- Initialization --
Initialization done
-- Sending Packet--
Packet Received:
1 1 0 0 0 1 1 1
Initialization done
-- Sending Packet--
Packet Received:
1 1 0 0 0 1 1 1
Initialization done
```

Figure 8.4: HyperTerminal Output Window showing correct transmission of two hard wired packets

Figure 8.5 shows some of the internal waveforms and signals from a 100-bit data length test. The blue signal shows the output of the bandpass filter centered around the space frequency in the demodulator and the green signal shows the output of the bandpass filter centered around the mark frequency in the demodulator. Notice that the *data_in* signal exactly aligns with the waveforms. The decoded result (*decode_result*) is a delayed version of the input signal due to the 80, 16kHz clock cycles required for synchronization initialization.

Fifty 100-bit data length packets were sent, all achieving perfect synchronization and 0% bit error rate thus verifying the correct operation of the hardware.

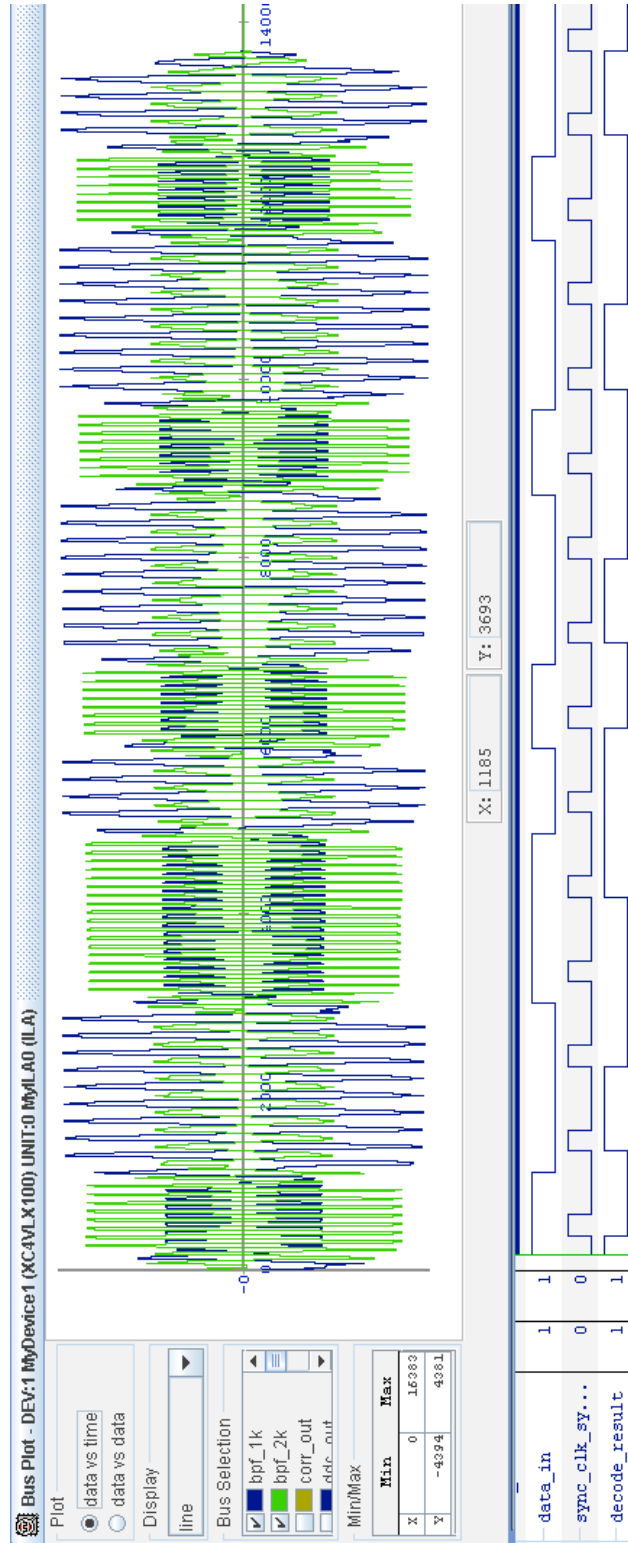


Figure 8.5: ChipScope Internal Waveforms and signals from a 100-bit data length test

8.2.2 Bucket Tests

For our initial in-water tests of the digital hardware, we sent a packet consisting of the 15 bit Gold Code of ‘011001010111101’ followed by a 100 bit packet of randomized ones and zeros with the M-Audio device through a 12 inch bucket of fresh tap water (Figure 8.6) and used the DINI board to synchronize and demodulate the data. Figure 8.7 shows a snapshot of the test result from post-analysis with ModelSim.



Figure 8.6: 12” Bucket Test

The four signals in the figure are: the output signal of the down converter (*DDCout*), the output of the reference cross correlation block (*correlation*) used for synchronization, and the output of the two bandpass filters in the demodulator. In the *DDCout* signal one can observe the FSK realization of the Gold Code followed by the first 8 bits of data (the digital ‘0’ being represented by the sparse waveform and the digital ‘1’ being represented by the dense waveform). The vertical arrow labeled ‘Index’ illustrates the synchronized peak found by the hardware which is a known clock delay from the start of the data (vertical arrow labeled ”Actual”). The bits written to the HyperTerminal revealed 0% error rate for the

100 bit packet from the 12 inch plastic bucket. Calculating the SNR as:

$$SNR = 10 * \log_{10} \left(\frac{\text{var}(\text{signal})}{\text{var}(\text{noise})} \right) \quad (8.1)$$

at the input to the digital down converter, the SNR in the bucket was 33 dB. The test was repeated with different data bits 10 times all producing 0% error.

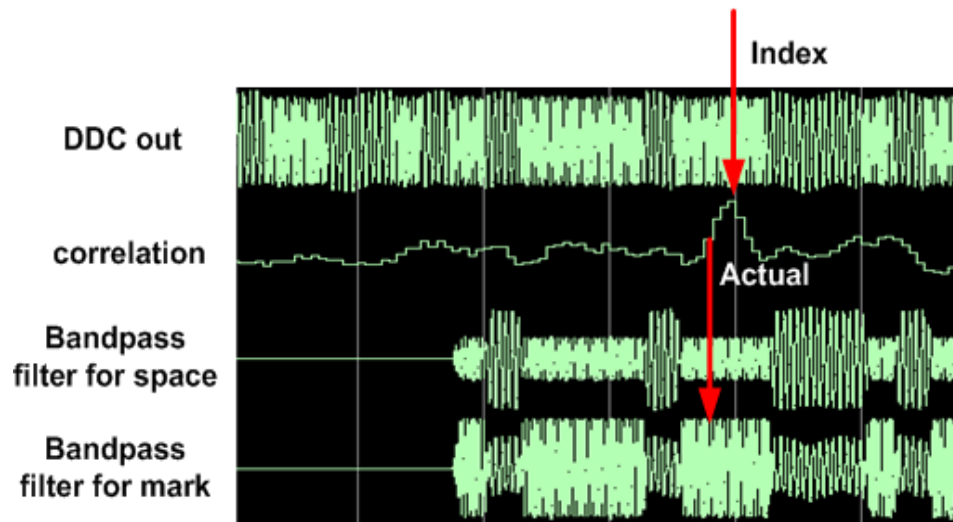


Figure 8.7: Snapshot of hardware simulation result for 12" bucket test

8.3 Integrated Tests

After verifying the correct operation of the analog and digital hardware separately, we conducted integrated system tests of the complete modem design in a tank, pool, and lake. To protect the digital electronics, we added a voltage limiter to the output of the pre-amplifier to clip all signals above 1.3Vpp. To characterize the multipath in the different environments, we sent a 200 ms 35k-45kHz chirp signal from the transmitter to receiver to measure the multipath delay spread. The multipath measurements and test results are described in the following subsections.

8.3.1 Multipath Measurements

As described in Chapter 3, underwater, there exist multiple paths from the transmitter to receiver, or multipath. Two fundamental mechanisms of multipath formation are reflection at the boundaries (bottom, surface, and any objects in the water), and ray bending (where rays of sound bend towards regions of lower propagation speed). The amount of multipath seen at the receiver depends on the locations of the transmitter and receiver and the geometric and physical properties of the environment.

The extent of the multipath at a receiver can be characterized by the multipath delay spread. Delay spread can be interpreted as the difference between the time of arrival of the first significant path (typically the line of site component) and the time of arrival of the last multipath component. Given the amplitude delay profile, $A_c(\tau)$, with effective signal length, M , the mean delay, $\bar{\tau}$, and the rms delay spread, τ_{rms} , are given as [154] :

$$\bar{\tau} = \frac{\sum_{n=1}^M \tau A_c(\tau)^2}{\sum_{n=1}^M A_c(\tau)^2} \quad (8.2)$$

$$\tau_{rms} = \sqrt{\frac{\sum_{n=1}^M (\tau - \bar{\tau})^2 A_c(\tau)^2}{\sum_{n=1}^M A_c(\tau)^2}} \quad (8.3)$$

For frequency shift keying, multipath will cause intersymbol interference when the multipath delay spread is larger than the symbol duration. Intersymbol

interference is a form of distortion of a signal in which one symbol interferes with subsequent symbols. This is an unwanted phenomenon as the previous symbols have similar effect as noise, thus making the communication less reliable [155]. Therefore, because the UCSDModem has a symbol duration of 5ms, the delay spread of the channel must be less than 5ms to ensure reliable communication.

To measure the multipath delay spread of the different test environments, we sent a 200 ms 35k-40kHz chirp signal from the transmitter to receiver and used the DAQ device to collect 5 seconds of the received signal containing the chirp. We then post-processed the received signal, correlating the transmitted waveform (the 2ms chirp) with the received waveform to form the amplitude delay profile. We then used equations 8.3 and 8.2 to compute the rms delay spread. The amplitude delay profiles and rms delay spread of each test environment are given in the following subsections along with performance results.

8.3.2 Tank Tests

We conducted an initial full integrated system test in a 0.5x1x0.5 meter tank filled with fresh water with the transducers spaced 50 cm apart. Five packets consisting of the reference code followed by 1000 randomized bits were sent from transmitter to receiver using all power levels. Calculating the SNR as:

$$SNR = 10 * \log_{10} \left(\frac{\text{var}(\text{signal})}{\text{var}(\text{noise})} \right) \quad (8.4)$$

at the input to the digital transceiver was 28dB for all power levels as the signal was clipped to 1.3Vpp at each level. All tests revealed 0% bit error rate. The rms delay spread in the tank was computed to be 1.86 ms from the amplitude delay profile given in Figure 8.8

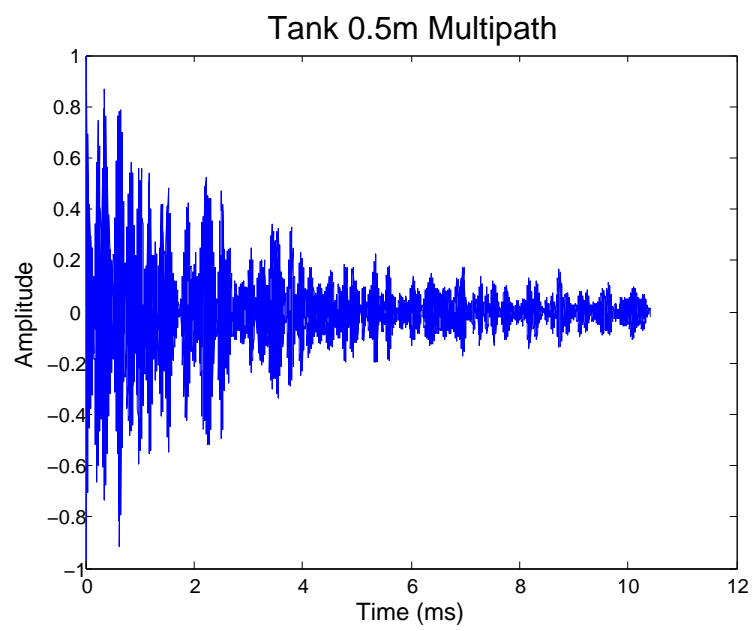


Figure 8.8: Multipath Amplitude Delay Profile at 0.5 m in the tank

8.3.3 Canyon View Pool Tests

We conducted another full integrated system test at the UCSD Canyon View Pool, a 50m x 25m concrete pool with 1m depth on the shallow end and 5m depth on the deep end filled with chlorinated fresh water. At 50 meters distance, we sent a packet of 400 symbols followed by a 400 symbol clearing period followed by another packet of 400 symbols using all power levels. The transducers were submerged to a depth of 10 cm and placed along the 50m side of the pool to avoid swimmers. The digital hardware was able to successfully detect the start of each packet, but failed to accurately demodulate the data, achieving only 25% bit error rate with an SNR of 14dB (for all power levels). The rms delay spread in the pool was computed to be 21.3 ms from the amplitude delay profile given in figure 8.9, thus causing severe intersymbol interference. Concrete pools are one of the most difficult underwater channels due to extremely strong multipath. As expected, a longer symbol duration or a channel equalizer would have to be added to the modem to improve the performance of the modem in high multipath environments.

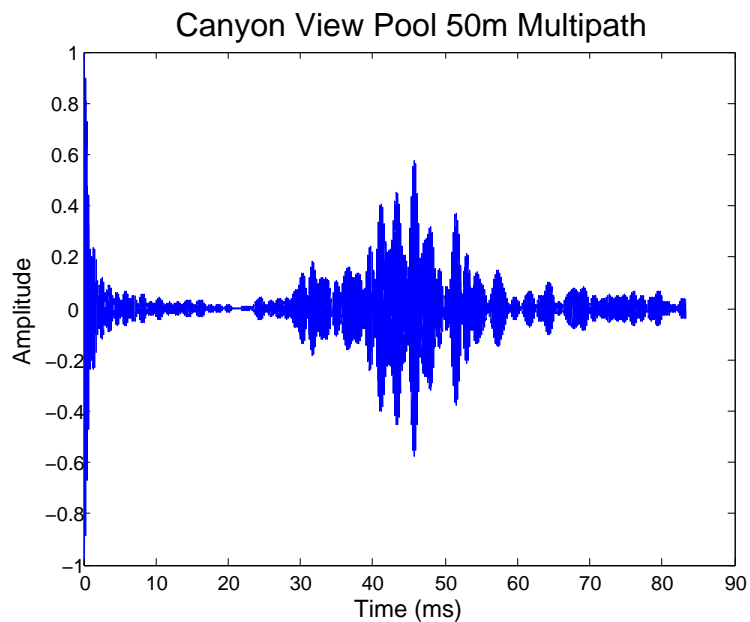


Figure 8.9: **Multipath Amplitude Delay Profile at 50m in the Canyon View Pool**

8.3.4 Westlake Tests

After completing tests in a tank and a pool, we conducted full integrated system tests in Westlake, a freshwater lake in Westlake Village, CA, at 5m, 50m, 95m, and 380m distances as shown in Figure 8.10. The transmitter was located on a dock, and the receiver was located on a boat. Five packets consisting of the reference code followed by 1000 randomized bits were sent from transmitter to receiver using all power levels. Tests at the 95 meter distance and 380 meter distance were incomplete due to the inability to remain near a private dock for a length of time.

The multipath amplitude delay profiles for the 5m, 50m, and 95m distances are given in Figures 8.11, 8.12, and 8.13 with calculated rms delay spreads of 2ms, 1.5 ms, and 2.66 ms respectively. Multipath at the 380 m distance was not measured.

The SNR at the input to the digital transceiver was 34dB for all power levels at the 5 meter distance, 21 dB for all power levels at the 50 meter distance, and 9 dB for power level 4 at the 380 meter distance (power levels 0-3 could not reach 380 meters). Bit error rates averaged 2.95%, 0.20%, and 4.13% at the 5 m, 50 m, and 380 m distances respectively. BER and SNR measurements were not measured at 95 meters.



Figure 8.10: Test Locations in Westlake

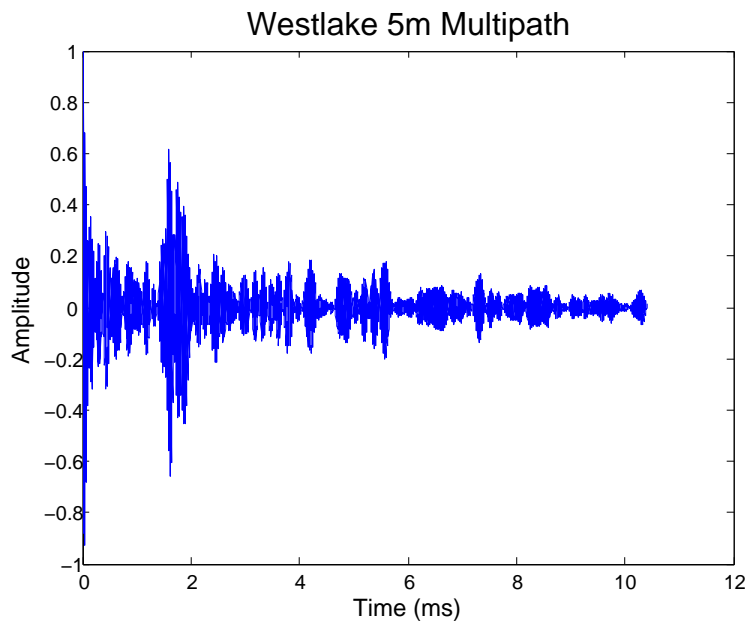


Figure 8.11: Multipath Amplitude Delay Profile at 5m in Westlake

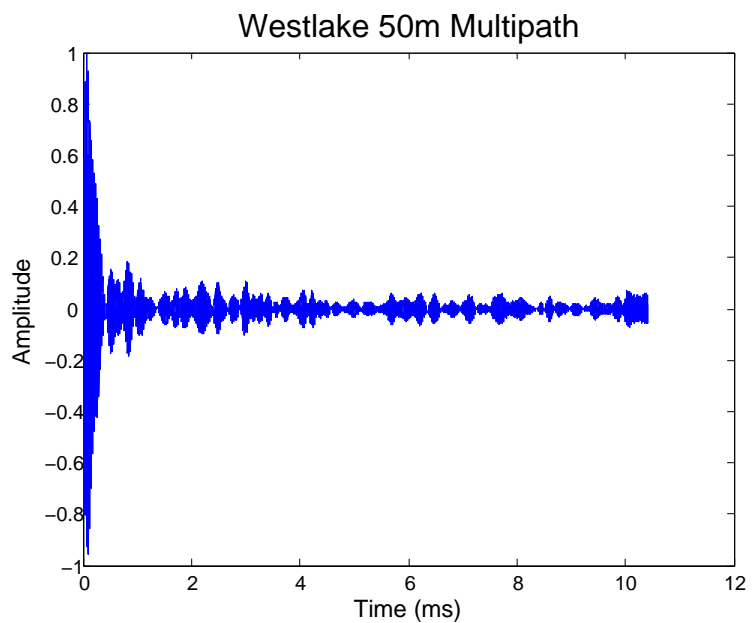


Figure 8.12: Multipath Amplitude Delay Profile at 50m in Westlake

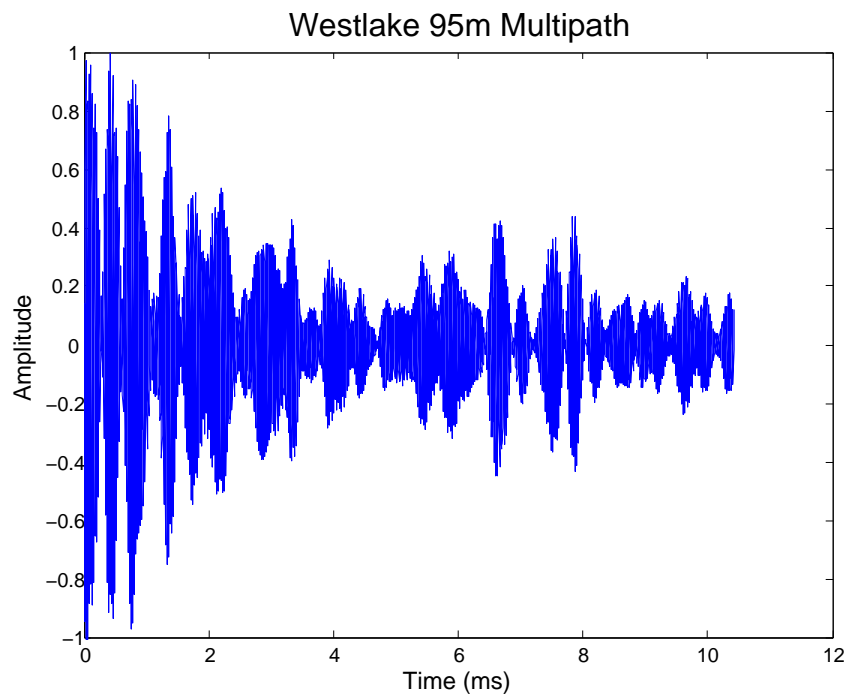


Figure 8.13: Multipath Amplitude Delay Profile at 95m in Westlake

8.3.5 Integrated System Test Summary

The integrated system test results in terms of distance, multipath delay spread, bit error rate, and SNR are summarized in Figure 8.14. As anticipated, the UCSDModem performed well (having a bit error rate of $<5\%$) in environments with a multipath spread less than 5 ms. The results also suggest that higher SNR will only improve performance for environments with low multipath.

8.4 Summary

This chapter described the analog, digital and integrated system tests used to evaluate the functionality and performance of the complete modem design. These tests prove that a short-range underwater acoustic modem can be designed from low-cost components. The tests indicate that the UCSDModem can support data rates of 200 bps for ranges up to ~ 400 meters with the power characteristics given in Table 9.2. Tables 4.1 and 4.2 show how the UCSDModem compares with existing commercial and research modems respectively.

The next chapter describes some deployment considerations one would have to realize to use the UCSDModem in a practical short-range, low data-rate underwater sensor network.

Selections of Chapter 8 are in part a reprint of the material as it appears in the proceedings of the IEEE Oceans Conference. The dissertation author was a co-primary researcher and author along with Ying Li, Brian Faunce, and Kenneth Domond. The other co-authors listed on this publication [1] directed and supervised the research which forms the basis for Chapter 8.

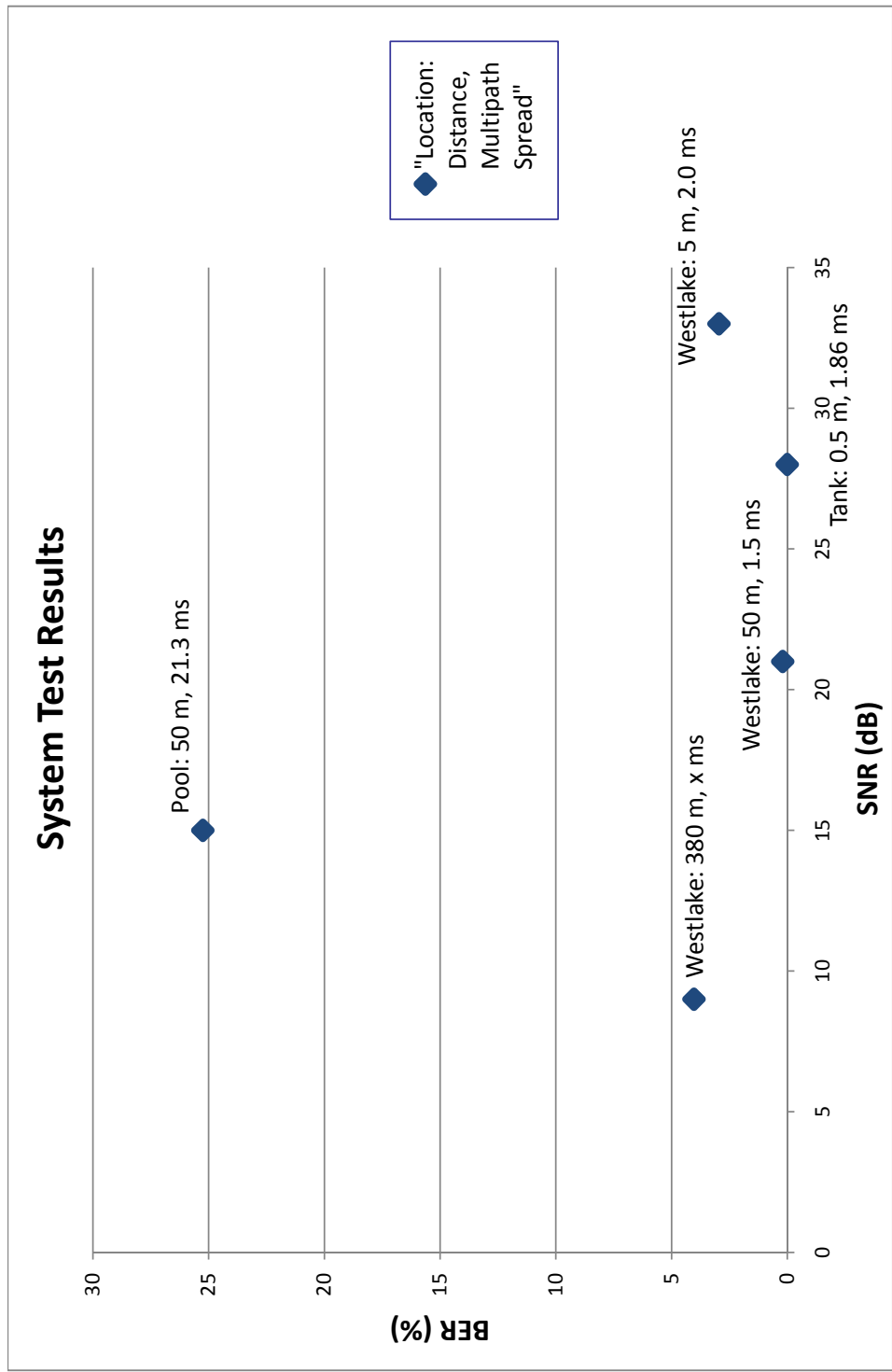


Figure 8.14: System Test Results

Chapter 9

Deployment Considerations

Now that we have described the full modem design and tested its performance, this chapter discusses some deployment considerations one would have to realize to use the modem in a practical underwater sensor network. We begin by describing a linear programming model that can be used to determine the required energy, cost, and lifetime of modems deployed on a given linear network. We then discuss battery, housing, and marine life considerations for underwater deployment.

9.1 Linear Programming Model

In order to determine the cost and energy requirements of modems on a given linear network, we use a linear programming model, modified from [156] with one of three objectives:

- Maximizing the lifetime of the network
- Minimizing the total energy consumption of the network
- Minimizing the total cost of the network

The model is given below:

$$\begin{aligned}
& \text{Maximize } t \text{ -or-} \\
& \text{Minimize } \sum_{j=2}^N e_j \text{ -or-} \\
& \text{Minimize } \sum_{j=2}^N c_j \\
& \text{Subject to:} \\
& f_{ij} \geq 0 \text{ for } i, j \in [1, N] \\
& f_{ij} = 0 \text{ for } i, j \notin E \\
& b_i \in [0, 1] \\
& b_i \geq \sum_j f_{ij} \\
& \sum_j f_{ij} - \sum_j f_{ji} = g_i t t \text{ for } i \in [2, N] \\
& t(\sum_j p_{tx,ij} f_{ij} + \sum_j p_{rx} f_{ji} + (b_i - \sum_j f_{ij} - \sum_j f_{ji}) p_{idle}) \leq e_i \text{ for } i \in [2, N] \\
& c_i = CMOD * b_i + CBAT(e_i/EBAT)
\end{aligned} \tag{9.1}$$

The network topology is represented by a graph $G = (V, E)$, where V is the set of nodes. An edge $(i, j) \in E \subset V \times V$ if node i can transmit to node j . The variables of the models are f_{ij} - the fraction packets transmitted from node i to node j , t - the network lifetime (expressed in seconds), e_i - the battery energy of node i (expressed in Joules), g_i - the packet generation rate for each node i (expressed in packets/second), tt - the packet transmission time (expressed in seconds), $p_{tx,ij}$ - the power consumed for transmission of a packet from node i to node j (expressed in Watts), p_{rx} - the power consumed for reception of a packet (expressed in Watts), p_{idle} - the power consumed while neither sending or receiving a packet, and c_i - the cost of the modem and its batteries at node i . b_i is a binary variable indicating the presence or absence of a modem at node i . $CMOD$, $CBAT$, and $EBAT$ are all constants indicating the cost of a modem, the cost of an individual battery, and the energy of an individual battery respectively chosen for deployment.

The first constraint necessitates that the fraction of time spent transmitting from node i to node j is not negative. The second constraint restricts the flow of

packets to only those nodes where transmission between node i and node j is possible. The third constraint defines the variables, b_i to be binary. The fourth constraint indicates a node is present if it sends data to any of the other nodes. The fifth constraint indicates the fraction of packets leaving node i must equal the fraction of packets received at node i plus the fraction of packets generated at node i . The sixth constraint indicates that the amount of power consumed receiving packets at node i plus the amount of power consumed transmitting packets at node i plus the amount of power consumed in an idle state over the network lifetime must be less than or equal to the amount of energy available at node i . The final constraint indicates that the cost of deploying a modem at node i is equal to the cost of the modem (if the modem is present) plus the total number of batteries required times the cost of a battery.

This model was written in Matlab using *lp_solve* [157], a linear and mixed integer/binary program solver based on the revised simplex method and the Branch-and-bound method for integers. *lp_solve* has no limit on model size and can be called as a library from different languages such as C, VB, .NET, Excel, Java, and Matlab.

In order to illustrate the use of the model, we apply it to a real application scenario of the Santa Barbara Channel Relocatable Mooring (CHARM). The CHARM is a shallow water mooring located in 24 m water depth off the town of La Conchita, CA (Figure 9.1). The CHARM has been retrieved and redeployed every 6 months since May 2003 with the purpose of: (1) developing and testing relatively small, lightweight optical and chemical sensors and real time data telemetry for autonomous deployment, (2) investigating particulate dynamics through optics, (3) optical and chemical detection and characterization of harmful algal blooms, and (4) determining effects of physical processes on chemical and bio-optical properties [158].

The CHARM supports RF telemetry from its location, 2 km from shore, to a shorebased data receiving station within line-of-sight and the 4 m instrument package is hard-wired to the surface buoy, but has been subject to failure. Ideally, all subsurface data would be transmitted to the surface buoy to be telemetered

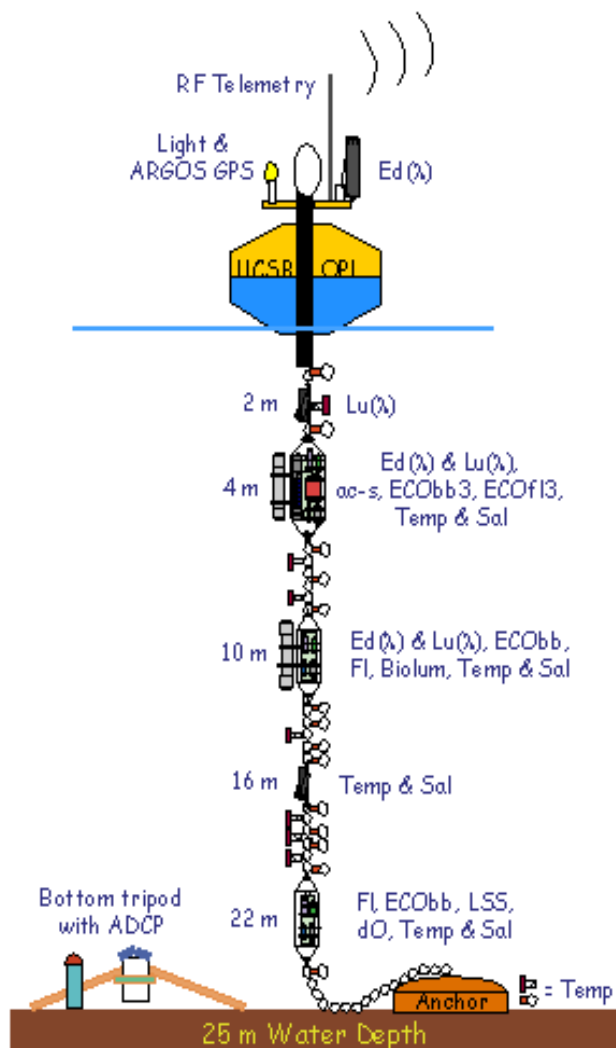


Figure 9.1: Santa Barbara Relocatable Mooring (CHARM)

to shore in near real-time. CHARM is equipped with physical, hydrographic, bio-optical, and chemical sensors as shown in Figure 2. The abbreviations in the Figure include: *GPS* = global positioning system, *RF* = radio frequency, *Ed(λ)* and *Lu(λ)* = downwelling irradiance and upwelling radiance, *ac-s* = absorption attenuation meter, *ECObb(3)* = backscattering sensor, *ECOf13* = spectral fluorometer; *Fl* = chlorophyll fluorometer; *Biolum* = bioluminescence sensor, *Temp* = temperature sensor, *Sal* = conductivity sensor, *dO* = dissolved oxygen sensor, *ADCP* = acoustic Doppler current profiler, *DH - 4* = data handler. The data

sampling rates for major sensors and sensor packages on CHARM are shown in Table 9.1.

Table 9.1: Data amounts for major sensors and sensor packages on the CHARM

Depth and Sensor or Sensor Package	Amount Data (per day)	Node Number
1 m SBE 39 Temperature Sensor	40 kB	2
2 m Hyperspectral Sensor	130 kB	3
4 m Sensor Package	450 kB	4
7 m SBE 39 Temperature Sensor	40 kB	5
10 m Sensor Package	325 kB	6
19 m SBE 39 Temperature Sensor	40 kB	7
22 m Sensor Package	65 kB	8

We use the data and distance parameters specified in Table 9.1 plus the power parameters specified in 9.2 (that combine the analog and digital hardware transmit, receive and idle power) as inputs to the linear programming model. We assume that the surface node (Node 1) can be solar powered and therefore do not report battery requirements for this node. The power to transmit from node i to node j is governed by the distance between the nodes, i.e. larger powers are required to transmit longer distances. In this particular application, all nodes could be reached with the lowest power level as the maximum distance between nodes is 22 meters. If distances were longer between nodes, additional nodes could be placed inbetween data nodes to act as repeaters and possibly reduce power consumption through multiple transmissions over shorter distances.

Table 9.2: UCSDModem Power Characteristics

Function	Power (W)
Tx	1.3-7.0
RX	0.42
Idle	0.33

Figure 9.2 and Table 9.3 show the routing, energy and cost results respectively of the linear programming model for minimizing battery energy and cost

for a deployment time of 6 months assuming a modem cost of \$500, an a cost per joule of \$10/70000 Joules. The modem cost was estimated using the parts cost of the modem given in the bill of materials and an estimated cost of a shallow water housing given in the following subsection. The battery cost and energy capacity was estimated from the cost and energy capacity of a standard C cell battery. Because the maximum transmit distance is 22 m, (a distance that can be handled by the lowest power of the modem) the routing scheme requires each node to send its data directly to the surface node.

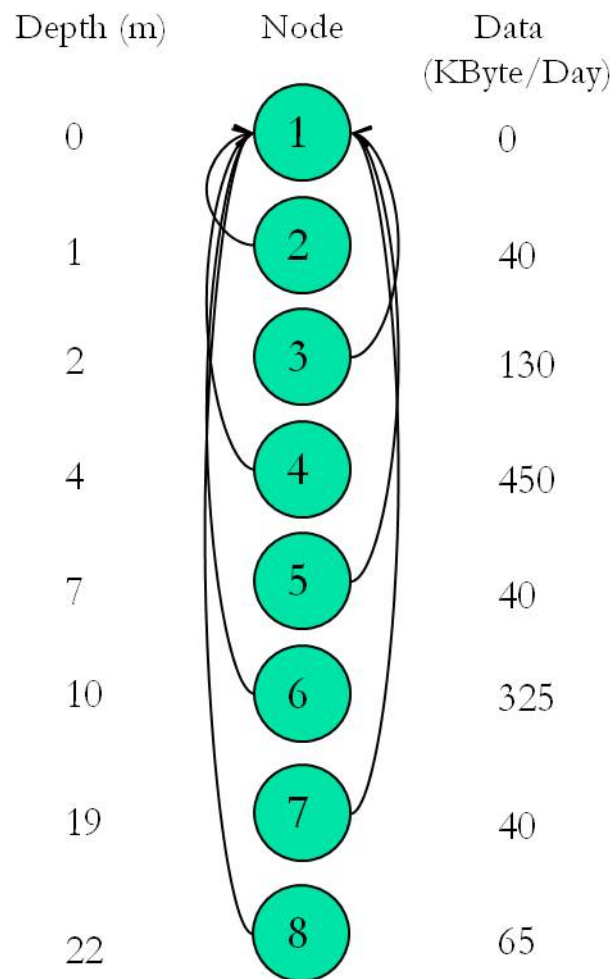


Figure 9.2: Routing schemes for optimal cost and energy (for 6 month deployment) or lifetime (for 140kJ of energy) on the CHARM

Table 9.3: Minimum Energy and Cost Requirements for a 6 month deployment of the CHARM mooring

Node	Energy (kJ)	Cost (\$)
1		500
2	5172	1238.8
3	5190	1241.5
4	5257	1251
5	5171	1238.8
6	5231	1247.3
7	5171	1238.8
8	5176	1239.5
Total	36370	8695.7

Figure 9.2 also shows the routing results of the linear programming model for maximizing the network lifetime, giving each node only 140kJ of energy. The maximum network lifetime for the SB CHARM deployed with the UCSDModem is 4.7 days. Reducing the idle power to 500uW (as per [77]) would increase the network lifetime to 6 months.

With these results, we see that the model is useful for giving a cost and energy requirement estimate for outfitting a given linear underwater network with a given acoustic modem. Note that the cost and energy estimates do not include costs associated with deploying the network, costs or energy associated with the network sensors themselves, nor cost and energy required for any possible packet loss. The model is also useful for determining the amount of energy savings a given reduction in transmit, receive, or idle power may provide in a practical application scenario.

9.2 Battery Considerations

Any practical underwater modem deployment requires a battery pack to provide power to the modem. Commercial modem companies sell battery packs separately so users can select the type, size, form factor, and energy capacity of the batteries for a given deployment. Users often select to purchase rechargeable batteries so they can reuse the batteries for more than one deployment. Popular

rechargeable batteries include rechargeable alkaline batteries, lithium ion (Li-ion) batteries, and nickel metal hydride (NiMH) batteries.

Rechargeable alkaline batteries cannot be recharged nearly as many times as NiMH or Li-ion batteries, and lose charge capacity after just a few charges, but are typically the least expensive of the rechargeable batteries. Li-ion batteries have a higher energy density, have a lower self discharge rate (they will retain their charge for a longer time), and can be smaller and lighter than most other types of rechargeables. However, because Li-ion batteries require special circuitry to protect the battery from damage due to undercharging or overcharging, they are typically more expensive than other rechargeables and require custom (and thus more expensive) chargers. Li-ion batteries are not available in standard cell sizes (like AA, C, and D) to ensure they are not placed in chargers that could damage the battery. NiMH batteries come in standard sizes, are less expensive than Li-ion batteries, can be rapidly recharged over 500 times, and have higher energy density than alkaline batteries (although less energy density than Li-ion batteries). Li-ion are usually preferred if the budget allows, but NiMH are suitable if a standard cell size is desired and cost is of importance. Standard C cell NiMH batteries cost \sim \$10 and provide 70000 J of energy.

9.3 Housing Considerations

Any practical underwater modem deployment also requires a water-proof housing rated to the depth of the deployment. The housing serves as both a mounting platform and a watertight casing for all the modem components. Commercial modem companies often sell housing separately so users can select the type, size, form factor, and depth rating needed for a given deployment. Housings that can withstand pressures at deeper depths are much more expensive than housings designed for shallow water deployments.

Typical underwater modem housings are made out of plastics rated to withstand pressures at a given depth. Pressures increase by 1 bar for every 10 meters below sea level, or 1 atmosphere for every 33 feet of sea water, so pressure at 100

meters reaches about 150 psi. These plastics also have high UV resistance as UV radiation causes plastics to become brittle and fail overtime. Some housings are made of UV resistant plastics such as Delrin (acetyl copolymer), or PEEK and for a 1" diameter rod stock cost \$4.50 and \$60.00 per foot respectively. Non UV resistant plastics such as PVC or ABS can be used as a low-cost alternative for short deployments. Schedule 80 3" PVC pipe is rated to a maximum operating pressure of 158 psi and costs roughly \$3 per foot. The size of the housing must be large enough to contain the modem hardware, batteries, and heat sink to reduce thermal dissipation.

All that being said, the hard part (and most expensive) is not the plastic tube used for the housing, but the required end caps and sealing hardware. Deflections in end caps become larger by r^4 , so keeping a relatively small tube diameter is desirable to avoid increased trouble with sealing. An estimate for an end cap designed for a 3" PVC pipe is \$100. O-rings and stainless steel nuts and bolts are used for sealing which cost on the order of \$20-\$50 depending on the design. Given these cost estimates, a 3" PVC housing for the UCSDModem would cost ~\$150.

9.4 Marine Life Considerations

Any practical underwater modem deployment also requires attention to its effect on marine life and the marine life's effect on the modem. Care must be paid to minimize the physical and acoustic interference between the modem and its surrounding environment.

9.4.1 Physical Effects

A modem deployed in marine environment will be subjected to biofouling - the undesirable accumulation of microorganisms, plants, algae, and/or animals on wetted structures. Barnacles or algae could build up on a transducer potentially blocking the modems signal and corrupting data. Anti-fouling techniques such as applying an anti-fouling coating, should be considered especially for long deployments.

Underwater instrumentation has also been known to suffer from shark bites and other physical damage from curious marine animals, thus protective cages should be considered depending on the deployment location and its inhabitants.

9.4.2 Acoustic Effects

Many marine animals use sound underwater including whales, dolphins, certain species of fish (such as the toadfish), and certain species of marine invertebrates (such as snapping shrimp). Marine organisms use sound to communicate, navigate and feed, using frequencies as low as 10Hz and as high as a few hundred kilohertz. Marine organisms communicating in the operating frequency band of an acoustic modem add to the ambient noise level in that band thus possibly corrupting signal transmission. Marine mammal calls have been known to increase ambient noise levels by 20-25 dB in the frequency band below 500 Hz and snapping shrimp have been known to corrupt signal transmission in the 2-15KHz band having individual source levels of 189 dB re 1 uPa at 1 meter (almost 50dB higher than the source level of our modem) [159]. Researchers can devise higher level networking protocols to counter the effects of marine life noise (i.e. retransmit when the noise source is absent) should the signal be corrupted by an organism producing sound in the modem's operating frequency band.

Acoustic modems on the other hand, must be designed not to cause physiological damage to marine organisms. Richardson et. al have shown that sound levels of 195-210 dB re 1 uPa may cause immediate damage to the auditory organs of baleen whales [162]. Simmonds and Hutchinson stated that intense underwater sound sources caused hemorrhage in the lungs and ulceration of the gastrointestinal tract for animals with air filled lungs or swim bladders [160]. In 1998, the Seattle Times reported hundreds of dead fish appeared in Lake Washington after 240 dB re 1 uPa airgun blasts were used to test for earthquake faults [161]. The UCSDModem operates at source levels well under those that have been shown to cause damage to marine life.

9.5 Summary

This chapter described a linear programming model that optimizes for cost, energy consumption or deployment time for a given linear underwater network equipped with acoustic modems, and described battery, housing, and marine life considerations. The linear programming model was used to equip an existing underwater network, the CHARM, with the UCSDModem to illustrate the modem's potential use, energy, cost and lifetime requirements in a practical real-life scenario. The next chapter describes some future improvements that could be made to the modem to make it more versatile for a wider variety of sensor network applications and underwater environments.

Chapter 10

Future Improvements

This thesis described the design and initial testing of a functional low-cost underwater acoustic modem prototype for short-range underwater sensor networks. The UCSDModem can support data rates of 200 bps for ranges up to ~ 400 meters in environments with less than 5 ms multipath delay spread. This chapter discusses possible future improvements to the modem to make it more versatile for a wider variety of sensor network applications and underwater environments.

Power Reduction: The linear programming model described in Chapter 9 showed the necessity of reducing power consumption (particularly idle power consumption) to ensure a longer deployment lifetime on a limited battery supply. Further improvements could be made to the analog and digital transceivers to make them more power efficient and a low power wake up circuit could be added to greatly reduce listening/idle power.

Wider Bandwidth, Higher Bit Rate: The existing FSK modulation scheme uses only a 1 kHz bandwidth which achieves a theoretical maximum bit rate of 500 bps and a practical bit rate of 200 bps. As the transducer is power efficient over a 5 kHz band (see Figure 6.9), the bandwidth of the receiver could be widened to amplify signals over the 5 kHz range allowing for a modulation scheme that uses more bandwidth allowing higher data rates. However, the widening of the receiver bandwidth comes at a cost of reducing gain, thus reducing transmis-

sion range.

Low-Power DSP: The existing digital transceiver design was implemented on a FPGA that provides comparable power consumption to other low power research modem designs. Because the FPGA does not offer considerable power savings over the other designs (see Table 7.4) and because FPGA design time is so high, it may make sense to move the design to a low-power DSP. DSPs can be much more easily configured and reprogrammed allowing the user to easily modify the modulation scheme and its parameters.

Channel Adaptive Modem: As shown in the system test results, the current modem design can only perform well in environments with a low multipath delay spread. An adaptive algorithm could be programmed into the modem to measure the channel characteristics and apply channel equalization and/or lengthen the symbol period for channels with high multipath.

The ideas conveyed in the thesis are shared with the material in the proceedings of the IEEE Oceans Conference and the Embedded Systems Letters. The dissertation author was a co-primary researcher and author along with Ying Li, Brian Faunce, and Kenneth Domond. The other co-authors listed on these publications [1, 2] directed and supervised the research which forms the basis for the dissertation.

Appendix A

Bill Of Materials

Table A.1 shows the bill of materials for the UCSDModem providing parts costs for the transducer, analog transceiver, and digital transceiver. Low volume costs are estimated for purchasing quantities of components for fewer than 50 modems. High volume costs are estimated for purchasing components in bulk (for some components such as resistors and capacitors that means quantities greater than 1000). Digital costs are estimated for a custom digital board that use the EP4CE30 FPGA and required peripherals.

Table A.1: Underwater Modem Bill of Materials

Transducer Components			
Part	Quantity	High Volume (\$)	Low Volume (\$)
Ceramic	1	10	10
Potting Compound	3 oz	10	10
Shielded cable	2"	1	1
1/4" cork sheet	1	6	6
1/8" cork sheet	1	13	13
Mold	1	2	2
Total	6	42	42
Analog Components			
Part	Quantity	High Volume (\$)	Low Volume (\$)
Resistors	92	16	17
Capacitors	76	32	54
Diodes	7	42	5
Mosfets	4	3	4
Comparator	1	1	2
Op Amps	12	36	53
Relays	6	28	40
Connectors	28	13	20
Ferrite Cores	3	5	7
Wires	4	4	4
Board	1	50	20
Total	234	162	248
Digital Components			
Part	Quantity	High Volume (\$)	Low Volume (\$)
FPGA	1	40	60
UART	1	2	5
ADC	1	2	4
DAC	1	5	7
Connectors	various	10	20
Digital Board	1	5	15
Total	6	148	195
Grand Total	246	~350	<500

Bibliography

- [1] B. Benson, Y. Li, B. Faunce, K. Domond, D. Kimball, C. Schurgers, and R. Kastner, Design of a Low-Cost, Underwater Acoustic Modem for Short-Range Sensor Networks, IEEE Oceans Conference, 2010.
- [2] B. Benson, Y. Li, B. Faunce, K. Domond, D. Kimball, C. Schurgers, and R. Kastner, Design of a Low-Cost Underwater Acoustic Modem, Embedded Systems Letters, accepted.
- [3] Y. Li, B. Benson, X. Zhang, and R. Kastner, Hardware Implementation of Symbol Synchronization for Underwater FSK, IEEE International Conference on Sensor Networks, Ubiquitous, and Trustworthy Computing, 2010.
- [4] R. Beckwith, D. Teibel, and P. Bowen, Unwired wine: Sensor networks in vineyards, In Proceedings of IEEE Sensors, 2004.
- [5] A. Mainwaring, J. Polastre, R. Szewczyk, and D. Culler, Wireless sensor networks for habitat monitoring, In Proceedings of the ACM Workshop on Sensor Networks and Applications, September 2002.
- [6] J. Lynch, K. Law, E. Straser, A. Kiremidjian, and T. Kenny, The Development of a Wireless Modular Health Monitoring System for Civil Structures, Proceedings of the MCEER Mitigation of Earthquake Disaster by Advanced Technologies Workshop, November 2000.
- [7] N. Ramanathan, M. Yarvis, J. Chhabra, N. Kushalnagar, L. Krishnamurthy, and D. Estrin, A stream-oriented power management protocol for low duty cycle sensor network applications, In Proceedings of the IEEE Workshop on Embedded Networked Sensors, May 2005.
- [8] J. Heidemann, W. Ye, J. Wills, A. Syed, and Y. Li, Research challenges and applications for underwater sensor networking, Proceedings of IEEE Wireless Communications and Networking Conference (WCNC), pp. 263-70, 2006

- [9] D. Codiga, J. A. Rice, and P. S. Bogden, Real-time wireless delivery of sub-surface coastal circulation measurements from distributed instruments using networked acoustic modems, Proceedings of MTS/IEEE Oceans 2000, 2000.
- [10] J. G. Proakis, E. M. Sozer, J. A. Rice, and M. Stojanovic, Shallow water acoustic networks, IEEE Communications Magazine, pp. 114-119, 2001.
- [11] E. M. Sozer, M. Stojanovic, and J. G. Proakis, Underwater acoustic networks, IEEE Journal of Oceanic Engineering, vol. 25, pp. 72-83, 2000.
- [12] H. Milburn, A. Nakamura, and F.I. Gonzalez, Deepocean Assessment and Reporting of Tsunamis (DART): Real-Time Tsunami Reporting from the Deep Ocean, NOAA Online Report, http://www.ndbc.noaa.gov/Dart/milburn_1996.shtml, 1996.
- [13] Ocean Research Interactive Observatory networks Website (ORION), <http://www.orionprogram.org>.
- [14] Laboratory for the Ocean Observatory Knowledge Integration Grid (LOOKING) Website, <http://lookingtosea.ucsd.edu>.
- [15] Monterey Accelerated Research System (MARS) Website, <http://www.mbari.org/mars/>.
- [16] NEPTURE Website, <http://www.neptune.washington.edu>.
- [17] D. Estrin, L. Girod, G. Pottie, and M. Srivastava, Instrumenting the world with wireless sensor networks, IEEE International Conference on Acoustics, Speech, and Signal Processing, 2001.
- [18] J. M. Rabaey, M. J. Ammer, J. L. da Silva, D. Patel, and S. Roundy, Pico-Radio supports ad-hoc ultra-low power wireless networking, IEEE Computer, pp. 42-48, 2000.
- [19] I. F. Akyildiz, D. Pompili and T. Melodia, Challenges for Efficient Communication in Underwater Acoustic Sensor Networks, ACM Sigbed Review, Vol. 1, No. 2, July 2004.
- [20] R. Jurdak, C. V. Lopes, and P. Baldi, Battery lifetime estimation and optimization for underwater sensor networks, in Sensor Network Operations, S. Phoha, T. F. LaPorta, and C. Griffin, Eds.: IEEE Press, 2004.
- [21] R. Galzin and J. P. Pointier, Moorea island, Societyarchipelago, Proceedings

of the 5th International Coral Reef Congress, vol. 1, pp. 73-102., 1985.

- [22] J. Jaffe and C. Schurgers, Sensor networks of freely drifting autonomous underwater explorers, Proceedings of ACM International Workshop on Underwater Networks, 2006.
- [23] J. Jaffe, R. Glatts, C. Schurgers, D. Mirza, P. Franks, P. Roberts, and F. Simonet, AUE: An Autonomous Float for Monitoring the Upper Water Column, in Proceedings of MTS/IEEE Oceans 2007, Aberdeen, Scotland, 2007.
- [24] D. Mirza and C. Schurgers, Collaborative localization for fleets of underwater drifters, in MTS/IEEE Oceans, October 2007.
- [25] G. Chang, T. Dickey, and M. Lewis, Toward a global ocean system for measurements of optical properties using remote sensing and in situ observations, Remote Sensing of the Marine Environment, vol. 6, pp. 285-326, 2006.
- [26] D. Frye, L. Freitag, R. Detrick, J. Collins, J. Delaney, D. Kelley, A. LaBonte, and K. Brown, An acoustically linked moored-buoy ocean observatory, EOS, 87(22), 2006.
- [27] A., Hamilton, M. Chaffey, E. Mellinger, J. Erickson, and L. McBride, Dynamic modeling and actual performance of the MOOS test mooring, Proceedings of MTS/IEEE Oceans, 2006.
- [28] Real-Time Oceanography with Inductive Moorings, Sea-Bird Electronics, Inc., http://www.seabird.com/technical_references/IMtutorialR2.htm.
- [29] B. Benson, F. Spada, D. Manov, G. Chang and R. Kastner, Real Time Telemetry Options for Ocean Observing Systems, European Telemetry Conference, April 2008.
- [30] Electromagnetic Wave, Def, American Heritage Dictionary of the English Language, 4th ed.
- [31] J.B. Lindsay, Mr. Lindsay's marine telegraph, Dundee Advertiser, 12th April 1853.
- [32] M. Siegel and R. W. P. King, Electromagnetic propagation between antennas submerged in the ocean, IEEE Trans. Antennas Propagation, vol. 4, pp. 507-513, 1973.
- [33] M. Rhodes, Electromagnetic Propagation in Sea Water and its value in Mil-

- itary Systems, Second Annual Conference of Systems Engineering for Autonomous Systems, July 2007.
- [34] L. Butler, Underwater Radio Communication, Amateur Radio, April 1987.
- [35] R. Moore, Radio Communications in the Sea, IEEE Spectrum, Vol 4, pp 42-51, Nov 1967.
- [36] T. Shelley, Radio waves transmit information underwater, An article in Eureka Magazine, Nov. 14, 2005.
- [37] Extremely Low Frequency Transmitter Site Clam Lake, Wisconsin, United States Navy Fact File, http://enterprise.spawar.navy.mil/UploadedFiles/fs_clam_lake_elf2003.pdf
- [38] A. I. Al-Shamma'a, A. Shaw, and S. Saman, Propagation of electromagnetic waves at MHz frequencies through seawater, IEEE Transactions on Antennas and Propagation, vol. 52, no. 11, pp. 2843-2849, Nov. 2004.
- [39] J. Lucas, A. Al-Shamma'a, J. Seim, W. Loehr, G. Puchbauer, and D. McGregor, Underwater communications using electromagnetic waves (EMCOMMS), in Proceedings of European Conference on Marine Science and Ocean Technology, 2004.
- [40] Wireless Fibre Systems, <http://www.wirelessfibre.co.uk/>.
- [41] R. Stewart, Introduction to Physical Oceanography, Texas A & M University, September 6, 2005.
- [42] L. Liu, S. Zhou and J.-H. Cui, Prospects and problems of wireless communication for underwater sensor networks, Wireless Communications and Mobile Computing, pp. 977-994, 2008.
- [43] Y. Ito, S. Haruyama, and M. Nakagawa, Short-Range Underwater Wireless Communication Using Visible Light LEDs, IEICE, 2006.
- [44] J. R. Apel, Principles of Ocean Physics, International Geophysics Series, Academic Press, Vol. 38, pp509-584, 1987.
- [45] H. Arst, Optical Properties and Remote Sensing of Multicomponential Water Bodies, Praxis Publishing, Chichester, UK, pg 8-28, 2003.
- [46] M. Chancey, Short Range Underwater Optical Communication Links, North

Carolina State University, Masters Thesis, 2005.

- [47] M. Kerker, *The Scattering of Light and other Electromagnetic Radiation*, 3rd Ed. Academic Press, New York, NY, 1973.
- [48] N.G. Jerlov, *Optical Oceanography*, Elsevier Publishing Company, New York, Vol. 5, pg 50-62, 118-126, 1968.
- [49] Underwater Laser Pops in Navy Ops. BBC News. 8 September 2009.
- [50] I. Vasilescu, K. Kotay, D. Rus, M. Dunbabin, and P. Corke, Data collection, storage, and retrieval with an underwater sensor network, *Proceedings of ACM Sensys*, 2005.
- [51] F. Schill, U.R. Zimmer, J. Trumpf, Visible spectrum optical communication and distance sensing for underwater applications, *The Australasian Conference Robotics and Automation ACRA*, 2004.
- [52] N. Farr, A. Chave, L. Freitag, J. Preisig, S. White, and D. Yoerger, Optical modem technology for seafloor observatories, *Oceans*, 2005.
- [53] J. Simpson, *A 1 Mbps Underwater Communication System using LEDs and Photodiodes with Signal Processing Capability*, North Carolina State University, Masters Thesis, 2007.
- [54] F. Hanson and S. Radic, High bandwidth underwater optical communication, *Applied Optics*, vol. 47, pp. 277283, Jan. 2008.
- [55] P. J. Westervelt and R. S. Larson, Laser-excited broadside array, *Journal of the Acoustic Society of America*, vol. 54, pp. 121122, 1973.
- [56] Y. H. Berthelot, Thermoacoustic generation of narrow-band signals with high repetition rate pulsed lasers, *Journal of the Acoustic Society of America*, vol. 85, pp. 11731181, 1989.
- [57] F. Blackmon, L. Estes, and G. Fain, Linear opto-acoustic underwater communication, *Applied Optics*, vol. 44, no. 18, pp. 38333845, Jun. 2005.
- [58] M. A. Ainslie and J. G. McColm, A simplified formula for viscous and chemical absorption in sea water, *Journal of the Acoustical Society of America*, vol. 103, no. 3, pp. 16711672, 1998.
- [59] F. Fisher and V. Simmons, Sound Absorption in Sea Water, *Journal of the*

- Acoustical Society of America, vol. 62, no. 3, pp. 558-564, 1977.
- [60] R. Urick, Principles of Underwater Sound. 3rd ed. New York: McGraw-Hill, 1983.
- [61] National Research Council (NRC), Ocean Noise and Marine Mammals. National Academies Press, 2003.
- [62] G.M. Wenz, Acoustic ambient noise in the ocean: Spectra and sources, Journal of the Acoustical Society of America, 34, 19361956, 1962.
- [63] J. Preisig, Acoustic propagation considerations for underwater acoustic communications network development, Proceedings of First ACM International Workshop on Underwater Networks, Sep. 2006.
- [64] M. Stojanovic, On the relationship between capacity and distance in an underwater acoustic communication channel, Proceedings of First ACM International Workshop on Underwater Networks, Sep. 2006.
- [65] M. Stojanovic, Underwater Acoustic Communications, Encyclopedia of Electrical and Electronics Engineering, John G. Webster, Ed., John Wiley & Sons, vol.22, pp.688-698. 1999.
- [66] Underwater Acoustic Propagation Modelling Software - AcTUP V 2.2L, <http://cmst.curtin.edu.au/products/actoolbox.cfm>.
- [67] D. B. Kilfoyle and A. B. Baggeroer, The state of the art in underwater acoustic telemetry, IEEE Journal of Oceanic Engineering, vol. 25, no. 1, pp. 427, Jan. 2000.
- [68] F. Tong, B. Benson, Y. Li, and . Kastner, Channel Equalization Based on Data Reuse LMS Algorithm for Shallow Water Acoustic Communication, IEEE International Conference on Sensor Networks, Ubiquitous, and Trustworthy Computing, June 2010.
- [69] LinkQuest, Inc., Underwater acoustic modems, <http://www.linkquest.com/html/models1.htm>.
- [70] Benthos, Inc., Acoustic Modems, <http://www.benthos.com/acoustic-tesonar-modem-product-comparison.asp>.
- [71] Trittech International, Trittech Micron Data Modem - Small ROV Communications, http://www.tritech.co.uk/products/products-micron_modem.htm.

- [72] Aquatec Group, AQUAmodem 500 Overview, <http://www.aquatecgroup.com/aquamodem.html>.
- [73] EvoLogics, Underwater Acoustic Modem <http://www.evologics.de/en/products/acoustics/index.html>.
- [74] DSPComm, AquaComm: Underwater wireless modem, http://www.dspcomm.com/products_aquacomm.html.
- [75] L. Freitag, M. Grund, S. Singh, J. Partan, P. Koski, and K. Ball, The WHOI micro-modem: an acoustic communications and navigation system for multiple platforms, MTS/IEEE OCEANS, pp. 1086-92 Vol, 2005.
- [76] Hydro International, Product Survey: Acoustic Modems, http://www.hydro-international.com/files/productsurvey_v-pdfdocument_15.pdf, June 2007.
- [77] J. Wills, W. Ye, and J. Heidemann, Low-power acoustic modem for dense underwater sensor networks, Proceedings of ACM International Workshop on Underwater Networks, 2006.
- [78] R. Jurdak, C.V. Lopes, and P. Baldi. Software Acoustic Modems for Short Range Mote-based Underwater Sensor Networks, Proceedings of IEEE Oceans Asia Pacific, May 2006.
- [79] MoteIV Corporation, www.moteiv.com.
- [80] R. A. Iltis, H. Lee, R. Kastner, D. Doonan, T. Fu, R. Moore and M. Chin. An Underwater Acoustic Telemetry Modem for Eco-Sensing, Proceedings of MTS/IEEE Oceans, September 2005.
- [81] T. Fu, D. Doonan, C. Utley, B. Benson, R. Kastner, R. A. Iltis, and H. Lee, AquaModem Field Tests in Moorea, Poster Presentation, Proceedings of ACM International Workshop on Underwater Networks, September 2007.
- [82] J. Namgung, N. Yun, S. Park, C. Kim, J. Jeon, and S. Park, Adaptive MAC Protocol and Acoustic Modem for Underwater Sensor Networks, Demo Presentation, Proceedings of ACM International Workshop on Underwater Networks, November 2009.
- [83] I. Vasilescu, C. Detweiler, and D. Rus, AquaNodes: An Underwater Sensor Network, Proceedings of ACM International Workshop on Underwater Networks, September 2007.

- [84] H. Yan, S. Zhou, Z. Shi, and B. Li, A DSP Implementation of OFDM Acoustic Modem, Proceedings of ACM International Workshop on Underwater Networks, September 2007.
- [85] S. Zhou, Z. Shi, J. Cui, H. Zhou, J. Liu, and P. Carroll, Aqua-fModem: A Stand-alone Underwater Acoustic Modem Based on OFDM Technology, Demo Presentation, November, 2009.
- [86] Z. Yan, J. Huang, C. He, Implementation of an OFDM underwater acoustic communication system on an underwater vehicle multiprocessor structure, Frontiers of Electrical and Electronic Engineering in China, vol. 2, no. 2, pp. 151-155, April 2007.
- [87] E. M. Sozer and M. Stojanovic, Reconfigurable Acoustic Modem for Underwater Sensor Networks, Proceedings of ACM International Workshop on Underwater Networks, 2006.
- [88] M. Vajapeyam, U. Mitra, J. Preisig, and M. Stojanovic, Distributed TR-STBC schemes for cooperative underwater acoustic communications, Proceedings of Oceans06 Asia Pacific, May 2006.
- [89] P. Ozog, M. Lesser, M. Stojanovic, Adapting the USRP as an Underwater Acoustic Modem, Poster Presentation, High Performance Embedded Computing, September 2009.
- [90] P. J. Gendron, Orthogonal frequency division multiplexing with on-off-keying: Noncoherent performance bounds, receiver design and experimental results, U.S. Navy Journal of Underwater Acoustics, vol. 56, no. 2, pp. 267300, Apr. 2006.
- [91] M. Stojanovic, Low complexity OFDM detector for underwater channels, Proceedings of MTS/IEEE OCEANS, September 2006.
- [92] Cadence PSpice A/D and Advanced Analysis
http://www.cadence.com/products/orcad/pspice_simulation/Pages/default.aspx
- [93] B. Li, S. Zhou, M. Stojanovic, L. Freitag, and P. Willett, Multicarrier communication over underwater acoustic channels with nonuniform Doppler shifts, IEEE Journal of Oceanic Engineering, vol. 33, no. 2, Apr. 2008.
- [94] B. Li, S. Zhou, M. Stojanovic, L. Freitag, and P. Willett, Non-uniform Doppler compensation for zero-padded OFDM over fast-varying underwater acoustic channels, in Proceedings of MTS/IEEE OCEANS conference, Aberdeen, Scot-

land, Jun. 18-21, 2007.

- [95] B. Li, S. Zhou, J. Huang, and P. Willett, Scalable OFDM design for underwater acoustic communications, in Proceedings of Intl. Conf. on ASSP, Las Vegas, NV, Mar. 3 Apr. 4, 2008.
- [96] T. Kang and R. A. Iltis, Matching Pursuits Channel Estimation for an Underwater Acoustic OFDM Modem, Proceedings of the 2008 IEEE International Conference on Acoustics, Speech, and Signal Processing Special Session on Physical Layer Challenges in Underwater Acoustic Communications, April 2008.
- [97] D. B. Kilfoyle, J. C. Preisig, and A. B. Baggeroer, Spatial modulation experiments in the underwater acoustic channel, IEEE Journal of Oceanic Engineering, vol. 30, no. 2, pp. 406415, Apr. 2005.
- [98] S. Roy, T. M. Duman, V. McDonald, and J. G. Proakis, High rate communication for underwater acoustic channels using multiple transmitters and space-time coding: Receiver structures and experimental results, IEEE Journal of Oceanic Engineering, vol. 32, no. 3, pp. 663688, July 2007.
- [99] B. Li, S. Zhou, M. Stojanovic, L. Freitag, J. Huang, and P. Willett, MIMO-OFDM over an underwater acoustic channel, Proceedings of MTS/IEEE OCEANS, September 2007.
- [100] Sensor Design Fundamentals: Piezoelectric Transducer Design for Marine Use, Airmar Technology Corporation, 2000.
- [101] Channel Industries Inc. Piezoelectric Ceramics Catalog, online document, www.channelindustries.com, Jun 2009.
- [102] Piezo Theory, APC International Ltd., http://www.americanpiezo.com/piezo_theory/index.html.
- [103] C.H. Sherman and J.L. Butler, Transducers and Arrays for Underwater Sound, New York: Springer, 2007.
- [104] Revision of DOD-STD-1376A, Ad Hoc Subcommittee Report on Piezoceramics, April 1986.
- [105] MIL-STD-1376B (Notice 1), Military Standard Piezoelectric ceramic material and measurements guidelines for sonar transducers, July 1999.

- [106] Morgan ElectroCeramics, <http://www.morganelectroceramics.com>.
- [107] O.B. Wilson, An Introduction to Theory and design of Sonar Transducers, Peninsula Pub, 1985.
- [108] Steminc, Steiner & Martins, Inc., <http://www.steminc.com/>.
- [109] Cytec Industries, <http://www.cytec.com/>.
- [110] Urethanes, Silicones, and Epoxies Seminar, Deep Sea Power and Light facilities, 4033 Ruffin Road, San Diego, CA 92123-1817, May 2009.
- [111] How-To Guide for Mold Making and Casting, Smooth-On, www.smooth-on.com.
- [112] R. Urick, Principles of Underwater Sound for Engineers, McGraw Hill Book Company, 1967.
- [113] W. MacLean, Absolute Measurement of Sound without a Primary Standard, Journal of the Acoustical Society of America, volume 12, pp 140-146, 1940.
- [114] P. Ebaugh, and R. Meuser, Practical Application of the Reciprocity Theorem in the Calibration of Underwater Sound Transducers, Journal of the Acoustical Society of America, volume 19, pp 695-700, 1947.
- [115] B. Simmons and R. Urick, The Plane Wave Reciprocity Parameter and Its Application to the Calibration of Electroacoustic Transducers at Close Distances, Journal of the Acoustical Society of America, volume 21, pp 633, 1949.
- [116] R. Bobber and G.A. Sabin, Cylindrical Wave Reciprocity Parameter, Journal of the Acoustical Society of America, volume 33, pp 446, 1961.
- [117] Marport Deep Sea Technology, <http://www.marport.com/>.
- [118] ITC-1042, Deep Water Omnidirectional Transducer, <http://www.itc-transducers.com>.
- [119] H. Krauss, C. Bostian, and F. Raab, Solid State Radio Engineering, John Wiley & Sons, 1980.
- [120] J. Honda and J. Adams, Application Note AN-1071, International Rectifier, Class D Audio Amplifier Basics, www.irf.com/technical-info/appnotes/an-1071.pdf

- [121] Electronics Tutorial about Amplifiers, Electronics-Tutorials, http://www.electronics-tutorials.ws/amplifier/amp_1.html.
- [122] C. Verhoeven, A. van Staveren, G. Monna, M. Kouwenhoven and E. Yildiz, Structured electronic design: negative feedback amplifiers, Boston/Dordrecht: Kluwer Academic, 2003.
- [123] I. F. Akyildiz, D. Pompili, and T. Melodia, Underwater acoustic sensor networks: research challenges, *Ad Hoc Networks* (Elsevier), 3(3):257–279, May 2005.
- [124] A. Phadke, Handbook of Electrical Engineering Calculations, Technology and Engineering, 1999.
- [125] M. Stojanovic, J. Catipovic, J.G. Proakis, Phase coherent digital communications for underwater acoustic channels, *IEEE Journal of Oceanic Engineering* 19 (1) (1994) 100111.
- [126] L. Freitag, M. Stojanovic, S. Singh, and M. Johnson, Analysis of channel effects on direct-sequence and frequency-hopped spread spectrum acoustic communications, *IEEE Journal of Oceanic Engineering*, vol. 26, no. 4, pp. 586593, Oct. 2001.
- [127] J. A. C. Bingham, Multicarrier modulation for data transmission: An idea whose time has come, *IEEE Communications Magazine*, pp. 514, May 1990.
- [128] Z. Wang and G. B. Giannakis, Wireless multicarrier communications: Where Fourier meets Shannon, *IEEE Signal Processing Magazine*, vol. 17, no. 3, pp. 2948, May 2000.
- [129] Analog Devices' New Blackfin Family Offers the Fastest and Most Power-Efficient Processors for Their Class, *Radio Locman*, 2003. <http://www.radiolocman.com/news/new.html?di=475>.
- [130] M. Yovits, *Advances in computers*, Academic Press, pp. 105-107, 1993.
- [131] A. Amara, F. Amiel, and T. Ea, FPGA vs. ASIC for low power applications, *Microelectronics Journal*, v. 37, pp. 669-677, 2006.
- [132] E. Rocha, Implementation Tradeoffs of Digital FIR filters, *Military Embedded Systems*, OpenSystems Publishing, 2007.
- [133] R. Kastner, A. Kaplan, and M. Sarrafzadeh, *Synthesis Techniques and Op-*

timizations for Reconfigurable Systems. Boston: Kluwer Academic, 2004.

- [134] W. Mangione-Smith , B. Hutchings , D. Andrews, A. DeHon , C. Ebeling , R. Hartenstein , O. Mencer , J. Morris, K. Palem , V. Prasanna , and H. Spaanenburg, Seeking Solutions in Configurable Computing, *Computer*, v.30 n.12, pp. 38-43, December 1997.
- [135] A. DeHon and J. Wawrzynek, Reconfigurable computing: what, why, and implications for design automation, *Proceedings 1999 Design Automation Conference*, IEEE, pp. 610-15, 1999.
- [136] K. Bondalapati and V. K. Prasanna, Reconfigurable computing systems, *Proceedings of the IEEE*, vol. 90, pp. 1201-17, 2002.
- [137] K. Compton and S. Hauck, Reconfigurable computing: a survey of systems and software, *ACM Computing Surveys*, vol. 34, pp. 171-210, 2002.
- [138] P. Schaumont, I. Verbauwhede, K. Keutzer, and M. Sarrafzadeh, A quick safari through the reconfiguration jungle, *Proceedings of the 38th Design Automation Conference (IEEE Cat. No.01CH37232)*. ACM. 2001, pp. 172-7.
- [139] Micro-Modem Overview, Woods Hole Oceanographic Institution, <http://acomms.whoi.edu/umodem/>.
- [140] D. Doonan, AquaModem Electronics Engineer, Personal Communication, May 2006.
- [141] M. LaPedus. FPGAs can outperform DSPs, study says, *DSP DesignLine*, 11/13/2006.
- [142] BDTI, FPGAs vs. DSPs: A look at the unanswered questions, *DSP Design Line* 1/11/2007.
- [143] ModelSim SE 6.4a. <http://model.com/content/modelsim-downloads>.
- [144] Spiral. <http://spiral.net/hardware/filter.html>.
- [145] S. Bregni, *Synchronization of Digital Telecommunications Networks*, WILEY, 2002.
- [146] E. M. Sozer and M. Stojanovic, Underwater Acoustic Networks, *IEEE Journal of Oceanic engineering*, Vol. 25, No. 1, January 2000.

- [147] C. Chien, Digital radio system on a chip: a system approach, Springer, 2001.
- [148] B. Watson, FSK: Signals and Demodulation, W. J. Communications, July 2004 [http://www.wj.com/pdf/technotes/FSK_signals_demod.pdf].
- [149] FPGA and Programmable Logic Journal, http://www.fpgajournal.com/fpgajournal/feature_articles/20090203_grand/.
- [150] Altera's New Cyclone IV, http://www.altera.com/corporate/news_room/releases/2009/products/nr-cyclone-iv.html.
- [151] DINI Group, DNMEG_ADDA, http://www.dinigroup.com/index.php?product=DNMEG_ADDA.
- [152] M-Audio Ltd, <http://www.m-audio.com>.
- [153] Xilinx Chipscope Pro, <http://www.xilinx.com/tools/cspro.htm>.
- [154] H. Li, D. Liu, J. Li, and P. Stoica, Channel order and RMS delay spread estimation with application to AC power line communications, Digital Signal Processing, Vol. 13, pp 284-300, 2003.
- [155] W. Dally and J. Poulton, Digital Systems Engineering, Cambridge University Press, pp. 280285, 1998.
- [156] S. Ergen and P. Varaiya, On multi-hop Routing for Energy Efficiency. Communications Letters, IEEE, Vol.9, Iss.10, Oct.2005, Pages: 880- 881.
- [157] Using lpsolve from Matlab, <http://lpsolve.sourceforge.net/5.5/MATLAB.htm>.
- [158] University of California Santa Barbara Ocean Physics Laboratory, CHAnnel Relocatable Mooring, (CHARM);<http://www.opl.ucsb.edu/mosean/datasb.html>.
- [159] Sounds in the Sea: What are common underwater sounds?, Discovery of Sound in the Sea Website, <http://www.dosits.org/science/soundsinthesea/commonsounds/>.
- [160] M.P. Simmonds and J.D. Hutchinson, The Conservation of Whales and Dolphins, John Wiley & Sons. 1996.
- [161] USGS Fish Kill Investigation, USGS, <http://walrus.wr.usgs.gov/earthquakes/ships/deadfish.html>.

- [162] W.J. Richardson, C.R. Green, C.I. Malme, D.H. Thompson, S.E. Moore, B. Wurwig, Effects of noise on marine mammals, Report prepared by LGL Ecological Research Associates Inc., TX, for US Minerals Management Service, Study 90-0093, NTIS PB 91-168914, pp 462.